

**LIGHT-LOAD BURN RATE ANALYSIS IN AN AIR-COOLED
UTILITY ENGINE**

by

John Richard Brossman

A thesis submitted in partial fulfillment of the requirements for the degree

of

Master of Science

(Mechanical Engineering)

at the

UNIVERSITY OF WISCONSIN – MADISON

2008

Approved: _____ **Date:** _____

Professor Jaal B. Gandhi
Department of Mechanical Engineering
University of Wisconsin - Madison

Abstract

In order to maximize the power-to-weight ratio, small, air-cooled utility engines are designed for WOT performance. Low-speed, light-load conditions suffer due to high residual gas retention, poor volumetric efficiency and an unfavorable in-cylinder flow field that can lead to heat release past EVO. Conditions with significant heat release past EVO have been found to contribute as a dominant HC emissions source at low-speed and light-load.

The effects of a dual spark configuration, an alternate spark location, and bulk flow improvement through swirl enhancement were investigated on a single-cylinder, air-cooled utility engine. A steady flow analysis of various swirl enhancement techniques was conducted on a steady flow bench with a swirl adaptor to obtain a global view of the intake flow angular momentum. Through in-cylinder pressure recording and exhaust gas sampling, a single-zone heat release and ring-pack model were utilized to analyze combustion and emissions performance. A similar operating condition was defined and explored to determine the light-load performance of various engine designs to isolate characteristics leading to improved performance.

It was found that a dual spark configuration advances combustion leading to a reduction in burn duration, but increased burning rate only occurs when the flame fronts are held independent. With a retarded combustion phasing strategy, HC and NO_x emissions were reduced independent of speed and load due to lower ring pack loading and a favorable post-oxidation environment. Conditions with significant heat release past EVO through

retarded combustion phasing were found to not increase HC emissions; an oxidation reaction was still in effect.

A port blockage that induced a tangential flow was found to significantly improve the part-throttle steady flow swirl coefficient leading to a greater global swirl ratio. Engine combustion tests using this blockage indicated a significant advance of combustion leading to decreased burn duration and reduced COV independent of speed and load. Due to the improved burn rate, lean operating conditions were explored and resulted in a significant reduction in HC emissions, but increased NO_x leading to a negligible change in the $\text{HC}+\text{NO}_x$ parameter from the rich condition.

A similarity condition was defined based on mean piston speed, IMEP and combustion phasing with engines of various size and geometry. This first order assessment provided similar thermodynamic conditions at CA50, with the intake and combustion chamber geometry produced in-cylinder flow field variations impacting combustion duration. Engines with centralized spark positions and pent-roof combustion chambers were found to improve the CAIgn-10 and CA10-50 duration over the side spark, bathtub configurations. Significant differences of the flame termination period, CA50-90, indicate favorable flow fields late in the cycle and may indicate a dependence on the cooling package associated with the engine.

Acknowledgements

There are many people that I need to thank for their help with this project. First and foremost, I can't thank Prof. Jaal Ghandhi enough for his patience and extensive help along the way. His guidance has allowed me to grow as an experimentalist and engineer.

Thanks to all the member companies of the Wisconsin Small Engine Consortium for their sponsorship, specifically Mike Pitcel from Briggs and Stratton for technical help and parts for the engine and Ken Derra for allowing us to use the Briggs flowbench. Thanks to Jeff Borman at Mercury and Phil Pierce at Harley for collecting data for the similarity study.

At the ERC, I have to thank Ralph Braun for his help machining and indispensable knowledge of all lab equipment. Thanks to Renato Yapaulo, James Krasselt and Kash Puntambekar who's help got me through fluids and combustion classes. Thanks to my office mates Victor Salazar, Ben Petersen, Doug Heim and Javier Vera for putting up with my ranting about EES and supporting my coffee addiction.

Finally, I would like to thank my friends and family for their love and support. Thanks to all of the guys from 639B for pushing me through undergrad. Thanks to Rachel at home, for her supportive conversations at any time of the day and to Becky for allowing me to experience life outside of the lab. To my parents, John and Theresa, and my sister Kelly, thank you for their love and support through all of this and you are the reason I have been able to succeed.

Table of Contents

| | |
|--|------|
| Abstract | i |
| Acknowledgements | ii |
| List of Figures | ix |
| List of Tables | xvi |
| Nomenclature | xvii |
| 1.0 Introduction | 1 |
| 1.1 Motivation..... | 1 |
| 1.1.1 Small Engines | 1 |
| 1.1.2 Burning Rate and Emissions..... | 2 |
| 1.1.3 Similarity Analysis..... | 3 |
| 1.2 Objectives | 4 |
| 2.0 Background and Literature Review | 6 |
| 2.1 Introduction..... | 6 |
| 2.2 Heat Release Rate Analysis | 7 |
| 2.2.1 Multiple-Zone Heat Release Analysis | 9 |
| 2.2.2 Heat Release Analysis Errors..... | 10 |
| 2.3 Engine Operating Condition Effects on Heat Release Rate..... | 11 |
| 2.3.1 Engine Speed | 11 |
| 2.3.2 Engine Load..... | 11 |
| 2.3.3 Air-Fuel Ratio | 11 |
| 2.3.4 Spark Timing | 12 |
| 2.4 Small Engine Emissions Testing | 12 |
| 2.5 Dual Spark Combustion..... | 13 |
| 2.5.1 Spark Location Effects on Heat Release Rate | 13 |
| 2.5.2 Dual Spark Configurations | 14 |
| 2.6 Retarded Spark Timing – Cold Start Conditions | 16 |
| 2.7 Bulk Flow and Turbulence in Engines..... | 19 |
| 2.7.1 Bulk Motion Measurement Techniques..... | 19 |

| | |
|---|-----------|
| 2.7.2 Non-Dimensional Flow Parameters | 20 |
| 2.7.2.1 Volumetric Efficiency | 20 |
| 2.7.2.2 Discharge Coefficient | 21 |
| 2.7.2.3 Flow Coefficient | 22 |
| 2.7.2.4 Swirl Coefficient and Swirl Ratio | 23 |
| 2.7.3 Bulk Motion and Turbulent Flow in Engines | 24 |
| 2.7.4 Bulk Flow and Turbulence Effects on Heat Release Rate | 26 |
| 2.8 Combustion Similarity | 27 |
| 2.8.1 Similarity Studies in Engines | 28 |
| 2.8.2 Combustion Chamber Geometry Effects on Combustion | 33 |
| 2.8.3 Valve Lift and Port Geometry Effects on Combustion | 36 |
| 2.9 Residual Gas Effects | 38 |
| 2.9.1 Residual Gas Effects on Heat Release Rate | 39 |
| 2.9.2 Residual Gas Effects on Emissions | 40 |
| 3.0 Experimental Setup | 41 |
| 3.1 Engine Description | 41 |
| 3.2 Engine Control System | 42 |
| 3.3 Ignition System | 43 |
| 3.4 Engine Dynamometer, Torque Sensor, and Shaft Encoder | 44 |
| 3.5 Fuel System | 45 |
| 3.5.1 Homogeneous Mixture System | 46 |
| 3.6 Air Delivery System | 47 |
| 3.7 Exhaust System | 48 |
| 3.8 Pressure Transducers | 49 |
| 3.9 Air-Fuel Ratio Analyzer | 49 |
| 3.10 Horiba Emissions Bench | 50 |
| 3.11 Engine Data Acquisition and Processing | 51 |
| 3.12 Steady Flowbench | 53 |
| 3.13 Swirl Adapter | 55 |
| 3.14 Flowbench Data Acquisition | 57 |

| | |
|---|-----|
| 4.0 Steady Flow Characterization | 58 |
| 4.1 Introduction..... | 58 |
| 4.2 Basic Flow Measurement..... | 58 |
| 4.3 ΔP Selection..... | 59 |
| 4.4 Data Acquisition | 61 |
| 4.5 Statistical Analysis of Uncertainty and Repeatability | 65 |
| 4.5.1 Volumetric Flow Rate..... | 65 |
| 4.5.2 Flow Coefficient | 67 |
| 4.5.3 Swirl Coefficient..... | 68 |
| 4.6 Throttle Effects on Steady Flow Tests..... | 71 |
| 4.7 Modified Combustion Chamber Steady Flow Tests..... | 73 |
| 4.8 Flow Modification | 77 |
| 4.8.1 Port Modifications | 77 |
| 4.8.1.1 Port Plates | 78 |
| 4.8.1.2 Charge Motion Control Valve | 79 |
| 4.8.2 Valve Modifications..... | 81 |
| 4.8.2.1 Shrouded Valves | 81 |
| 4.8.2.2 “Pin-Wheel” Blockage Valves..... | 83 |
| 4.8.2.3 “Pin-Wheel” Blockage on the Valve Stem | 85 |
| 4.8.2.4 Port Blockages | 87 |
| 4.9 Steady Flow Conclusions..... | 89 |
| 5.0 Engine Performance Characterization | 91 |
| 5.1 Introduction..... | 91 |
| 5.2 Operating Condition Effects on Heat Release Rate..... | 92 |
| 5.2.1 Engine Speed Effects on Combustion Performance | 92 |
| 5.2.2 Load Effects on Combustion Performance | 94 |
| 5.2.3 Ignition Timing Effects on Combustion Performance..... | 96 |
| 5.2.4 Spark Location Effects on Combustion Performance..... | 97 |
| 5.3 Dual Spark Sweep Effects on Heat Release Rate | 100 |
| 5.3.1 Combustion Phasing: CA50..... | 100 |

| | |
|---|-----|
| 5.3.2 Spark Timing Sweeps | 102 |
| 5.3.2.1 Mean Best Torque Spark Timing..... | 102 |
| 5.3.3 Burn Duration | 104 |
| 5.3.4 Flame Propagation | 105 |
| 5.3.5 Flame Termination..... | 108 |
| 5.3.6 Heat Transfer Effects on Heat Release | 109 |
| 5.3.7 Dual Spark Combustion Conclusions..... | 111 |
| 5.4 Combustion Phasing Effects on Emissions..... | 112 |
| 5.4.1 Retarded Spark Timing Effects on Burn Rate | 113 |
| 5.4.2 Retarded Spark Timing Effects on HC | 113 |
| 5.4.2.1 EIHC Emissions Response | 114 |
| 5.4.2.2 Mass-Based HC Emissions Response..... | 117 |
| 5.4.2.3 Oxygen Concentration Response..... | 118 |
| 5.4.3 Retarded Spark Timing Effects on NO _x Emissions | 120 |
| 5.4.4 COV Effects on Heat Release..... | 122 |
| 5.4.5 COV Effects on Emissions | 123 |
| 5.4.6 Combustion Phasing Emissions Conclusions | 125 |
| 5.5 Engine Replacement | 125 |
| 5.6 Swirl Enhanced Flow Field Effects on Heat Release | 128 |
| 5.6.1 Swirl Condition Comparison | 128 |
| 5.6.2 Emissions Response from Swirl Enhanced Conditions..... | 131 |
| 5.6.2.1 HC Emissions Response with Swirl Enhancement..... | 132 |
| 5.6.2.2 NO _x Emissions Response with Swirl Enhancement | 133 |
| 5.6.2.3 O ₂ Emissions Response with Swirl Enhancement..... | 134 |
| 5.6.3 COV with Swirl Enhancement..... | 135 |
| 5.6.4 Combustion Duration with Swirl Enhancement | 136 |
| 5.6.5 AF Ratio Exploration with Swirl Enhancement | 136 |
| 5.6.6 Lean, Retarded Combustion Phasing with Swirl Enhancement | 138 |
| 5.6.6.1 HC Response with Lean, Retarded Combustion Phasing and Swirl Enhancement | 139 |

| | |
|--|------------|
| 5.6.6.2 NO _x Response with Lean, Retarded Combustion Phasing and Swirl Enhancement | 141 |
| 5.6.6.3 O ₂ Response with Lean, Retarded Combustion Phasing and Swirl Enhancement | 143 |
| 5.7 Combustion Stability | 143 |
| 5.7.1 Condition Definition | 144 |
| 5.7.2 Engine Description..... | 144 |
| 5.7.3 Similar Condition Heat Release Results..... | 145 |
| 5.7.4 Similar Condition Conclusions..... | 148 |
| 6.0 Discussion..... | 150 |
| 6.1 Heat Release Rate Improvement..... | 150 |
| 6.1.1 Burn Duration Comparison..... | 151 |
| 6.1.2 Combustion Phasing Comparison..... | 151 |
| 6.1.3 COV Comparison..... | 152 |
| 6.1.4 Relative Heat Release Improvement Conclusions..... | 153 |
| 6.2 Bulk Flow Description..... | 153 |
| 7.0 Conclusions and Recommendations..... | 156 |
| 7.1 Overview..... | 156 |
| 7.2 Summary of Results..... | 156 |
| 7.3 Recommendations..... | 159 |
| References..... | 162 |
| Appendix A.1: Pressure Transducer Calibration..... | 166 |
| Appendix A.2: WOT Flowbench Data..... | 167 |

List of Figures

| | |
|--|----|
| Figure 1.1.1: Common Combustion Chamber Designs..... | 2 |
| Figure 2.2.1: Single-Zone Heat Release Analysis Control Volume (taken from [3]) | 8 |
| Figure 2.2.2: Two-Zone Heat Release Rate Analysis Control Volume (taken from [10])..... | 10 |
| Figure 2.5.1: Early Flame Interaction with Dual Spark Combustion of Flame Surface Density Plots (taken from [26])..... | 15 |
| Figure 2.6.1: HC Oxidation Plateau with Retarded Spark Timing Conditions (taken from [29]) | 18 |
| Figure 2.7.1: Common Steady Flow Configuration for Momentum Measurement (taken from [33]) | 19 |
| Figure 2.7.2: Response of C_D and C_F with Non-dimensional Valve Lift | 23 |
| Figure 2.7.3: Turbulence Intensity Scaling with Mean Piston Speed with Various Intake Geometries (taken from [34])..... | 25 |
| Figure 2.7.4: Turbulent Model Spectrum (taken from [39])..... | 26 |
| Figure 2.8.1: Log-P, Log-V Plot of an Engine Cycle | 29 |
| Figure 2.8.2: Technical Diagram of Scaled MIT Engines (taken from [35]) | 30 |
| Figure 2.8.3: Pent-roof and Bathtub Combustion Chamber and Valve Arrangement (taken from [55]) | 34 |
| Figure 2.8.4: Variation of In-Cylinder Flow from a CFD Analysis (taken from [55])..... | 35 |
| Figure 2.8.5: Port Positioning for Increased Swirl and Similar Geometry (taken from [42]) | 37 |
| Figure 2.8.6: Similar Engines of Varying Bore-to-Stroke Ratio Combustion Rates (taken from [59]) | 38 |
| Figure 2.9.1: Increasing Combustion Duration with Increasing Residual Gas (taken from [62]) | 39 |
| Figure 3.1.1: Modified Intek Head | 42 |
| Figure 3.5.1: Test Cell Fuel and Air Layout..... | 45 |
| Figure 3.12.1: Engine Head and Swirl Adaptor Arrangement..... | 53 |
| Figure 3.12.2: SuperFlow 600 Flowbench Setup (taken from [64])..... | 54 |

| | |
|--|----|
| Figure 3.13.1: Negligible Flow Modification Due to Swirl Adaptor | 55 |
| Figure 3.13.2: Strain Gage Pattern..... | 56 |
| Figure 4.3.1: Flow Coefficient Response with Varying Pressure..... | 60 |
| Figure 4.3.2: Swirl Coefficient Convergence with Increasing Pressure Drop..... | 60 |
| Figure 4.4.1: Orifice Plate and Swirl Adaptor Attachment | 61 |
| Figure 4.4.2: Orifice Plate Swirl Coefficient Response over Varying ΔP | 62 |
| Figure 4.4.3: Orifice Plate Torque Response with Varying ΔP | 63 |
| Figure 4.4.4: Output Voltage Time Varying Response with ΔP | 63 |
| Figure 4.4.5: Orifice Plate Torque Response with Varying ΔP | 64 |
| Figure 4.5.1: Repeatability from 15 Randomized Tests of the Volumetric Flow Rate | 65 |
| Figure 4.5.2: Mean Values of Volumetric Flow Rate with Uncertainty Error Bars | 66 |
| Figure 4.5.3: Repeatability from 15 Randomized Tests of the Flow Coefficient..... | 67 |
| Figure 4.5.4: Mean Values of Flow Coefficient with Uncertainty Error Bars | 68 |
| Figure 4.5.5: Repeatability from 15 Randomized Tests of the Swirl Coefficient | 69 |
| Figure 4.5.6: Swirl Coefficient and Torque Data Indicating Noise at Low Valve Lifts..... | 69 |
| Figure 4.5.7: Mean Values of Swirl Coefficient with Uncertainty Error Bars | 70 |
| Figure 4.6.1: Effect of the Throttle Setting on the Flow Coefficient..... | 71 |
| Figure 4.6.2: Swirl Coefficient Response with Partial Throttle Conditions | 72 |
| Figure 4.6.3: Diagram of the Throttle Plate Relative to the Combustion Chamber | 73 |
| Figure 4.7.1: Modified Combustion Chamber; ‘Decked’ Geometry..... | 73 |
| Figure 4.7.2: Port Configuration for “Natural” CCW Flow Momentum..... | 74 |
| Figure 4.7.3: Swirl Coefficient Response to WOT “Decked” Combustion Chamber..... | 75 |
| Figure 4.7.4: Swirl Coefficient Response to Partial Throttle “Decked” Combustion Chamber | 75 |
| Figure 4.7.5: Flow Coefficient Response for the Decked Chamber Geometry | 77 |
| Figure 4.8.1: CCW Port Plate Design and Position in the Head..... | 78 |
| Figure 4.8.2: Partial Throttle Flow Coefficient Response Due to Port Plates Favoring CCW and CW Flow Direction | 78 |
| Figure 4.8.3: Partial Throttle Swirl Response Due to Port Plates Favoring CCW and CW Flow Direction..... | 79 |

| | |
|---|----|
| Figure 4.8.4: CMCV Design and Position in the Head..... | 79 |
| Figure 4.8.5: CMCV Plate Designs for 50% and 75% Port Area Blockage..... | 80 |
| Figure 4.8.6: Partial Throttle Flow Coefficient Response Due to Various CMCV Plate Blockage..... | 80 |
| Figure 4.8.7: Partial Throttle Swirl Response Due to Various CMCV Plate Blockages..... | 81 |
| Figure 4.8.8: Shrouded Valve Design and Position in the Head | 82 |
| Figure 4.8.9: Partial Throttle Flow Coefficient Response Due to the Shrouded Valve..... | 82 |
| Figure 4.8.10: Partial Throttle Swirl Response Due to the Shrouded Valve | 83 |
| Figure 4.8.11: Pin-Wheel Blockage Design and Position on the Valve | 83 |
| Figure 4.8.12: Partial Throttle Flow Coefficient Response Due to the Pin-Wheel Blockages at the Valve Face..... | 84 |
| Figure 4.8.13: Partial Throttle Swirl Response Due to the Pin-Wheel Blockage at the Valve Face | 84 |
| Figure 4.8.14: Pin-Wheel Blockage Position in the Head Attached to the Stem..... | 85 |
| Figure 4.8.15: Partial Throttle Flow Coefficient Response Due to the Pin-Wheel Blockages Attached to the Valve Stem | 86 |
| Figure 4.8.16: Partial Throttle Swirl Response Due to the Pin-Wheel Blockages Attached to the Valve Stem..... | 86 |
| Figure 4.8.17: Tangential Blockage Position in the Head Attached to the Stem..... | 87 |
| Figure 4.8.18: Partial Throttle Flow Coefficient Response Due to the Port Blockages | 88 |
| Figure 4.8.19: Partial Throttle Swirl Response Due to the Port Blockages..... | 88 |
| Figure 4.8.20: WOT and Partial Throttle Flow Coefficient Response Due to the Tangential Blockage Attached to the Head for Combustion Tests..... | 90 |
| Figure 4.8.21: WOT and Partial Throttle Swirl Coefficient Response Due to the Tangential Blockage Attached to the Head for Combustion Tests..... | 90 |
| Figure 5.2.1: Variance of Heat Release at 10% Load..... | 92 |
| Figure 5.2.2: Variance of Heat Release at 25% Load..... | 93 |
| Figure 5.2.3: Variation of Heat Release at 1750 RPM | 94 |
| Figure 5.2.4: Variation of Heat Release at 3060 RPM | 95 |
| Figure 5.2.5: Variation of Heat Release with Spark Timing | 96 |

| | |
|---|-----|
| Figure 5.2.6: Variation of Heat Release Rate with Spark Position at 10% Load | 98 |
| Figure 5.2.7: Variation of Heat Release Rate with Spark Position at 25% Load | 98 |
| Figure 5.3.1: Direct Relationship between Ignition Timing and CA50 Phasing | 101 |
| Figure 5.3.2: Matched Combustion Phasing Heat Release Rate Response | 101 |
| Figure 5.3.3: BSFC to indicate MBT for the Spark Sweep Tests | 103 |
| Figure 5.3.4: Burn Duration Response to Varying Spark Positions | 104 |
| Figure 5.3.5: Flame Propagation Response to Varying Spark Positions | 106 |
| Figure 5.3.6: Flame Termination Period for Varying Spark Positions | 108 |
| Figure 5.3.7: Heat Transfer Rate for Dual Spark and Single Spark Combustion | 110 |
| Figure 5.4.1: Peak Pressure Response with Retarded Combustion | 112 |
| Figure 5.4.2: Exhaust Gas Temperature Response with Combustion Phasing | 113 |
| Figure 5.4.3: EIHC Emissions Response Due to Combustion Phasing | 114 |
| Figure 5.4.4: EIHC _{CA90-EVO} Emissions Response Due to Combustion Phasing | 116 |
| Figure 5.4.5: Exhaust HC Emissions Response Due to Combustion Phasing | 118 |
| Figure 5.4.6: Exhaust O ₂ Emissions Response Due to Combustion Phasing | 119 |
| Figure 5.4.7: Exhaust HC Response to Reduced O ₂ Levels | 120 |
| Figure 5.4.8: NO _x Emissions Response Due to Combustion Phasing | 121 |
| Figure 5.4.9: COV Effects from Dual Spark Combustion | 122 |
| Figure 5.4.10: EIHC Emissions Response from COV Effects | 123 |
| Figure 5.4.11: EI NO _x Emissions Response from COV Effects | 124 |
| Figure 5.5.1: HRR from the Old and New Engine | 126 |
| Figure 5.5.2: EIHC Response with Retarded Spark Timing Sweep from the Old and New Engine | 127 |
| Figure 5.5.3: EINO _x Response with Retarded Spark Timing Sweep from the Old and New Engine | 127 |
| Figure 5.5.4: Exhaust O ₂ Response with Retarded Spark Timing Sweep from the Old and New Engine | 128 |
| Figure 5.6.1: Variation of Heat Release with Spark Position and Swirl for 1750 RPM 10% Load | 129 |

| | |
|--|-----|
| Figure 5.6.2: Variation of Heat Release with Spark Position and Swirl for 1750 RPM 25% Load | 130 |
| Figure 5.6.3: Variation of Heat Release with Spark Position and Swirl for 3060 RPM 10% Load | 130 |
| Figure 5.6.4: Variation of Heat Release with Spark Position and Swirl for 3060 RPM 25% Load | 131 |
| Figure 5.6.5: EIHC Response with Swirl Enhancement..... | 132 |
| Figure 5.6.6: Mass-based HC Response with Swirl Enhancement..... | 133 |
| Figure 5.6.7: EINO _x Response with Swirl Enhancement..... | 134 |
| Figure 5.6.8: O ₂ Response with Swirl Enhancement..... | 135 |
| Figure 5.6.9: COV Response with Swirl Enhancement..... | 135 |
| Figure 5.6.10: Combustion Duration Response with Swirl Enhancement | 136 |
| Figure 5.6.11: Combustion Duration Response with Varying AF Ratio..... | 137 |
| Figure 5.6.12: EIHC, EINO _x , EIHC+NO _x Response with Varying AF Ratio..... | 138 |
| Figure 5.6.13: Combustion of Stock and Swirl Enhanced Conditions of Varying Combustion Phasing and AF Ratio..... | 139 |
| Figure 5.6.14: EIHC Response with Lean, Retarded Combustion Phasing and Swirl Enhancement..... | 140 |
| Figure 5.6.15: Mass-Based HC Response due to Lean, Retarded Combustion Phasing and Swirl Enhancement | 140 |
| Figure 5.6.16: EIHC _{CA90-EVO} Emissions Response Due to Lean Combustion Phasing and Swirl Enhancement | 141 |
| Figure 5.6.17: EINO _x Response with Lean, Retarded Combustion Phasing with Swirl Enhancement..... | 142 |
| Figure 5.6.18: EIHC+NO _x Response with Lean, Retarded Combustion Phasing and Swirl Enhancement | 142 |
| Figure 5.6.19: O ₂ Response Due to Lean, Retarded Combustion Phasing and Swirl Enhancement | 143 |
| Figure 5.7.1: In-Cylinder Pressure Response of the Engines at the Similarity Condition..... | 145 |

| | |
|---|-----|
| Figure 5.7.2: Heat Release Rate of the Engines at the Similarity Condition..... | 146 |
| Figure 5.7.3: Mass Fraction Burned Curve of the Engines at the Similarity Condition | 146 |
| Figure 5.7.4: Differentiated Mass Fraction Burned Curve of the Engines at the Similarity Condition | 147 |
| Figure 6.1.1: Burn Duration Comparison of Various Techniques to Modify Light-Load Heat Release Rate | 151 |
| Figure 6.1.2: Combustion Phasing Comparison of Various Techniques to Modify Light-Load Heat Release Rate | 152 |
| Figure 6.13: COV Comparison of Various Techniques to Modify Light-Load Heat Release Rate | 152 |
| Figure 6.2.1: Flow Coefficient Response to Various References Areas from Table 5.6.1 | 155 |
| Figure A.1.1: Kistler In-cylinder Pressure Transducer Calibration..... | 166 |
| Figure A.1.2: MotoTron MAP Sensor Calibration | 166 |
| Figure A.2.1: WOT Flow Coefficient Response due to the Port Plates Favoring CCW and CW Flow Direction..... | 167 |
| Figure A.2.2: WOT Swirl Coefficient Response Due to Port Plates Favoring CCW and CW Flow Direction | 167 |
| Figure A.2.3: WOT Flow Coefficient Response Due to Various CMCV Plate Blockages.. | 168 |
| Figure A.2.4: WOT Swirl Coefficient Response Due to Various CMCV Plate Blockages . | 168 |
| Figure A.2.5: WOT Flow Coefficient Response Due to the Shrouded Valve..... | 169 |
| Figure A.2.6: WOT Swirl Coefficient Response Due to the Shrouded Valve | 169 |
| Figure A.2.7: WOT Flow Coefficient Response Due to the Pin-Wheel Blockages at the Valve Face | 170 |
| Figure A.2.8: WOT Swirl Coefficient Response Due to the Pin-Wheel Blockages at the Valve Face | 170 |
| Figure A.2.9: WOT Flow Coefficient Response Due to the Pin-Wheel Blockages Attached to the Valve Stem..... | 171 |

Figure A.2.10: WOT Swirl Coefficient Response Due to the Pin-Wheel Blockages Attached to the Valve Stem.....171

Figure A.2.11: WOT Flow Coefficient Response Due to the Port Blockages172

Figure A.2.12: WOT Swirl Coefficient Response Due to the Port Blockages172

Figure A.2.13: WOT Flow Coefficient Response Due to the Port Blockage on the Modified Heat Used for Combustion Tests.....173

Figure A.2.14: WOT Swirl Coefficient Response Due to the Port Blockage on the Modified Head Used for Combustion Tests173

List of Tables

| | |
|---|-----|
| Table 3.1.1: Briggs and Stratton Intek™ Model 128603 Specifications..... | 41 |
| Table 3.5.1: EPA Tier II EEE Fuel Specifications | 46 |
| Table 4.5.1: Uncertainty of Volumetric Flow Rate for WOT and Partial Throttle Tests | 66 |
| Table 4.5.2: Uncertainty of the Flow Coefficient for WOT and Partial Throttle Tests.... | 67 |
| Table 4.5.3: Uncertainty of the Flow Coefficient for WOT and Partial Throttle Tests.... | 70 |
| Table 5.1.1: Engine Test Matrix | 91 |
| Table 5.2.1: Combustion Performance Data for 10% Load Conditions | 93 |
| Table 5.2.2: Combustion Performance Data for 25% Load Conditions | 93 |
| Table 5.2.3: Combustion Performance Data for 1750 RPM Conditions | 95 |
| Table 5.2.4: Combustion Performance Data for 3060 RPM Conditions | 95 |
| Table 5.2.5: Combustion Performance Data for Ignition Timing Sweep | 96 |
| Table 5.2.6: Combustion Performance Data for 10% Load Spark Position Sweep | 99 |
| Table 5.2.7: Combustion Performance Data for 25% Load Spark Position Sweep | 99 |
| Table 5.5.1: Engine Comparison of HRR and Emissions..... | 126 |
| Table 5.6.1: Variation of Heat Release Parameters with Spark Position and Swirl for 129 RPM and 10% Load..... | 129 |
| Table 5.6.2: Variation of Heat Release Parameters with Spark Position and Swirl for 1750 RPM 25% Load..... | 129 |
| Table 5.6.3: Variation of Heat Release Parameters with Spark Position and Swirl for 3060 RPM, 10% Load..... | 130 |
| Table 5.6.4: Variation of Heat Release Parameters with Spark Position and Swirl for 3060 RPM, 25% Load..... | 131 |
| Table 5.7.1: Similar Operation Condition Definitions..... | 144 |
| Table 5.7.2: Engine Geometry and Speed | 145 |
| Table 5.7.3: MFB Parameter Comparison of Various Engines at the Similarity Condition..... | 147 |
| Table 6.2.1: Various Reference Areas for Flow Coefficient Calculation..... | 154 |
| Table 6.2.2: Various Area Values and Corresponding Global Swirl Ratio Values..... | 155 |

Nomenclature

| | |
|--|---|
| AF | Air-Fuel Ratio |
| AOA | Angle of Attack |
| $^{\circ}\text{aTDC}$ | After Top Dead Center |
| $^{\circ}\text{bTDC}$, $^{\circ}\text{b}$ | Before Top Dead Center |
| B/S | Bore-to-stroke |
| CA | Crank Angle |
| CA10 | 10% of the Mass Fraction Burned |
| CA50 | 50% of the Mass Fraction Burned |
| CA90 | 90% of the Mass Fraction Burned |
| CAIgn-10 | Duration between Ignition and CA10, Early Flame Propagation |
| CA10-50 | Duration between CA10 to CA50, Flame Propagation |
| CA50-90 | Duration between CA50 to CA90, Flame Termination |
| CA10-90 | Duration between CA10 to CA90, Burn Duration |
| CCW | Counter-clockwise |
| C_D | Discharge Coefficient |
| C_F | Flow Coefficient |
| CFO | Choked Flow Orifice |
| CMCV | Charge motion control device |
| CO | Carbon Monoxide |
| CO ₂ | Carbon Dioxide |
| COV | Coefficient of Variance |
| C_s | Swirl Coefficient |
| CW | Clockwise |
| ECU | Engine Control Unit |
| EI | Emissions Index |
| EGR | Exhaust Gas Recirculation |
| EVC | Exhaust Valve Close |
| EVO | Exhaust Valve Open |
| HC | Hydrocarbons |
| HMS | Homogeneous Mixture System |
| HRR | Heat Release Rate |
| IVC | Intake Valve Close |
| IVO | Intake Valve Open |
| IMEP | Indicated Mean Effective Pressure |
| LHV | Lower Heating Value |
| MFB | Mass Fraction Burned |
| \dot{m} | Mass flow rate |
| N | Engine Speed |
| n | Polytropic Exponent |
| NO _x | Oxides of Nitrogen |
| O ₂ | Oxygen |

| | |
|------------|--|
| OH | Hydroxyl |
| ppm | Parts per million |
| Q_{CH} | Chemical Energy |
| Q_{HR} | Heat Release Energy |
| Q_{HT} | Heat Transfer Energy |
| r_c | Compression Ratio |
| RPM | Revolutions Per Minute |
| S_L, S_T | Laminar flame speed, Turbulent flame speed |
| T | Temperature |
| TQ | Torque |
| t_v | t-estimator |
| TDC | Top Dead Center |
| UEGO | Universal Exhaust Gas Oxygen Sensor |
| V | Volume |
| WOT | Wide Open Throttle |
| η_v | Volumetric Efficiency |
| γ | Ratio of Specific Heats |
| θ | CA |

1.0 Introduction

1.1 Motivation

Engine development is driven by the desire to improve performance and meet emissions regulations; small engines are no exception. The small engine market has met emissions requirements without exhaust after-treatment and advanced combustion strategies, but more stringent regulations may require a change. After-treatment, such as a three-way catalyst commonly found on automotive engines, provides an expensive solution for the small engine emissions problem. To avoid this expense, strategies to increase the burn rate through turbulence enhancement and dual spark combustion have been investigated.

1.1.1 Small Engines

The high power-to-weight ratio common for small engines has led to design optimization at wide open throttle (WOT) conditions. A cam design and valve timing that provides high breathing capacity under these conditions, typically lacks in light-load, low-speed performance due to increased trapped residual gases and poor bulk charge motion. Prior studies by Haugle and Albert investigated the influence of trapped residual by way of external exhaust gas recirculation and internal residual retention and found the residual could be “tuned” to provide decreased emissions, but at the loss of burning rate [1,2].

Intake port geometry in small engines is simplistic to keep costs at a minimum; charge motion in the cylinder is dominated by combustion chamber design. To maintain a small package, an overhead valve design is common, with a simple “bathtub” chamber design (see Fig. 1.1.1).

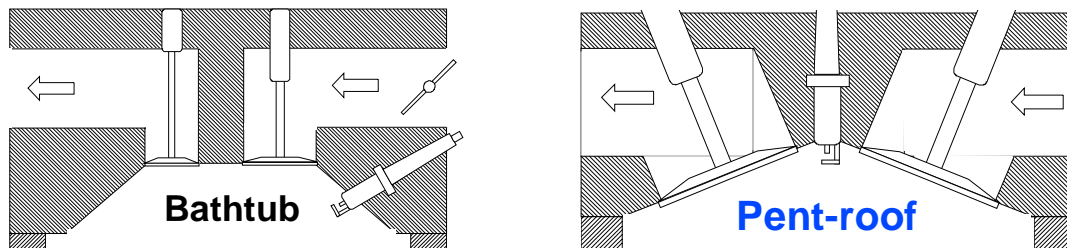


Figure 1.1.1: Common Combustion Chamber Designs

This geometry allows for easy maintenance, sufficient high-load performance, and low cost for the consumer, but the resulting burn rate at light-load, low-speed conditions is extremely slow.

1.1.2 Burning Rate and Emissions

The poor performance at light-load, low-speed conditions is reflected in the speed at which the fuel-air mixture (charge) can burn within the combustion chamber. In order to obtain the highest work from the reaction, combustion should take place as fast as possible to allow for complete expansion of the hot gases, yielding the highest work transfer to the piston. It is not uncommon to have combustion taking place after the exhaust valve has opened under these conditions. Previous studies have shown, long combustion duration and combustion occurring during the exhaust period is a possible source of emissions [1, 3].

Small engine emissions are regulated on an HC+NO_x basis. Prior investigations by Salazar and Haugle indicated HC emissions dominate the value during light-load, load-speed operation due to ring-pack effects, combustion past the exhaust valve open period (EVO) and high levels of trapped residual [1, 3]. Emissions were found to be weakly dependent on misfires and poor combustion quality, but could be improved with increased residual at an increase in combustion duration. Improved mixing through increased charge motion by simple geometry modification of the intake port was found to significantly increase the

burning rate with minimal loss to high-load, high-speed performance [4]. Through improved charge motion and spark timing strategies, the combustion duration can be decreased resulting in no heat release past EVO and a favorable HC oxidation environment created by increased exhaust gas temperatures. Lessons learned from the automotive industry can be applied to these small engines with minimal research and development reducing the adoption cost retaining the high value to the consumer.

1.1.3 Similarity Analysis

Due to the simplistic design of small engines, strikingly similar geometry can be found across a wide range of applications. Minor differences between engines can yield significant benefits in light-load burning rate therefore a comparison at the same operating condition can highlight those with under-performing designs. To this end, a similarity study comparing combustion conditions between geometrically similar engines was conducted.

To ensure similar in-cylinder conditions between varying engines, mean piston speed, load, and combustion phasing were held constant. Since all of the tested engines have varying levels of combustion chamber and intake port design complexity, variations due to improved charge motion will appear in the heat release rate and burning rate analysis. This “similarity condition” will present the varying designs with comparable levels of peak pressure, and location of peak pressure which can also lead to a comparison of the influence of the piston ring-pack on emissions. By creating a proper testing methodology, member companies will be able to compare engines of varying geometry without sacrificing the time and money necessary to map different operating conditions.

1.2 Objectives

The influence of bulk charge motion on heat release rate and burning rate has been well documented in automotive engines, but due to the unique operating conditions and low consumer cost, the investigations are more scant in utility engines. Measures to increase the bulk motion can yield a significant improvement in burning rate and emissions over the current designs.

The main objective of this project was to investigate simple methods to increase the bulk swirling charge motion to improve the burning rate and reduce the emission formation in a small air-cooled utility engine.

This study will investigate light-load, low-speed burning rate improvement strategies with simple features such as a dual spark combustion chamber and intake charge motion control devices.

For the dual spark combustion configurations, the engine head has been modified with provisions for two spark plugs, which fire simultaneously. Conditions will be compared to the stock spark location at the stock timing. A general conclusion will be made about spark location and number of ignition locations concerning heat release rate and emissions formation.

Investigations into simple bulk motion control devices were conducted on a steady flow bench. Modifications were primarily conducted to change the port geometry through easily implementable techniques applicable to a wide range of designs. Valve modifications to block or direct portions of the flow have also been conducted. Non-dimensional flow parameters are utilized to allow a comparison between different designs, with particular interest to flow and swirl coefficients. The highest swirl configuration was selected, and

implemented on the engine for combustion tests and heat release analysis. A general conclusion will be made about swirl enhancement through simple bulk flow modification through heat release rate analysis and emissions formation.

Finally, a combustion similarity methodology was developed to compare engines at a similar operating condition in the light-load, low-speed regime. An engine from each of the Wisconsin Small Engine Consortium member companies, along with geometrically similar engines located at the ERC, were compared at the similarity test condition for comparison of burning rate. A general conclusion will be made about combustion similarity testing methodology and a first-order comparison in burning rate with geometrically similar engines.

2.0 Background and Literature Review

2.1 Introduction

In-cylinder fluid motion has been investigated since the beginning of engine development. In the hundred years of development, the automotive industry has made significant advancement in burn rate enhancement through head and port optimization, spark location and valve timing. Before the advent of complex computational simulation, engineers created methods to speed up the development of new, advanced engine designs from those of high-performance designs through similarity and parametric studies. This method, most commonly used by the diesel industry, provided a first-order assessment of a new design. The small engine community, due to other constraints, has not kept pace with the developments of the automotive industry, but certain techniques can be adapted to small engine development. Through a greater understanding of in-cylinder fluid flow and techniques developed in the automotive industry, the small engine community can by-pass ineffective technology to meet the burn rate and emissions requirements of tomorrow.

Previously documented research associated with in-cylinder flow enhancement, burn rate enhancement as well as engine similarity studies will be discussed in this chapter. An introduction to small engine testing, steady flow measurement and heat release rate will be provided. These topics will provide the background, experimental methodology and purpose of this research.

2.2 Heat Release Rate Analysis

Internal combustion (IC) engines convert chemical work into power by way of exothermic reactions increasing the in-cylinder pressure. During the development of the IC engine, experimenters have found ways of relating the release of the chemical energy to the work output. In the 1930's, Rassweiler and Withrow compared flame propagation images recorded simultaneously with in-cylinder pressure data to determine the volume and mass fraction burned (MFB). Their analysis of the MFB for a given condition required prior knowledge of the ignition state (subscript o), the end of combustion state (subscript f) and the assumption of a constant polytropic exponent (n) through equation 2.2.1:

$$x_b = \frac{P_i^{1/n} V_i - P_o^{1/n} V_o}{P_f^{1/n} V_f - P_o^{1/n} V_o} \quad \text{Eqn. 2.2.1}$$

Subsequent methods have proven to be more accurate, but this method continues to be used today to provide a fast estimation of MFB [5]. This method represents a comparison of the pressure data from a motoring condition and that of a combusting condition to determine the effect of pressure on the system.

Krieger and Borman [6], and later Gatowski *et al.* [7] improved on this primitive estimation of heat release through a First Law balance of a single-zone, closed system (see Fig. 2.2.1).

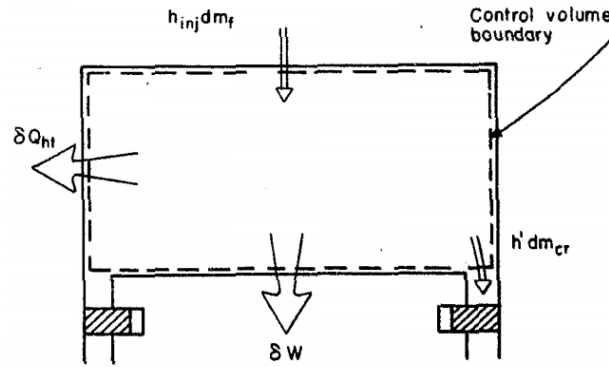


Figure 2.2.1: Single-Zone Heat Release Analysis Control Volume (taken from [3])

Through some thermodynamic manipulation and using the sign convention indicated above, the heat release of the system can be determined by:

$$\frac{dQ_{HR}}{d\theta} = \frac{\gamma}{\gamma-1} P \frac{dV}{d\theta} + \frac{1}{\gamma-1} V \frac{dP}{d\theta} + \frac{dQ_{HT}}{d\theta} \quad \text{Eqn. 2.2.2}$$

The first and second term represent the change in sensible energy from the chemical conversion during combustion and associated work imparted on the piston due to the change in pressure. The third term relates the energy loss due to heat transfer effects to the cylinder wall; commonly modeled as a convection term. Integrating Eqn. 2.2.2 between the ignition crank angle and exhaust valve open time (EVO) provides the heat release rate (HRR) for the entire combustion period [6,7,8].

The determination of the ratio of specific heats, γ , is of significant importance for an accurate heat release rate. The parameter's strong dependency on temperature can be modeled, with considerable accuracy, as a linear relationship [9]:

$$\gamma(T) = a + b * T \quad \text{Eqn. 2.2.3}$$

Where a and b are chosen to be 1.392 and -8.14×10^{-5} with T in Kelvin [8].

The MFB relation comes from a determination of the total possible energy released from the fuel as indicated by:

$$Q_{CH} = \dot{m}_{fuel,cycle} LHV \eta_C \quad \text{Eqn. 2.2.4}$$

Where LHV is the lower heating value of the fuel and η_C represents the combustion efficiency. Normalizing the heat release rate $\left(\frac{dQ_{HR}}{d\theta}\right)$ by Q_{CH} results in the mass fraction burned curve:

$$MFB = \frac{\int_{IGN}^{EVO} dQ_{HR}}{Q_{CH}} \quad \text{Eqn. 2.2.5}$$

Combustion phasing parameters are commonly associated with the MFB curve to describe when in-cylinder events occur. The positions in CA of 10%, 50% and 90% of the MFB curve are usually referred to CA10, CA50 and CA90. Burn duration, which describes the lifespan of the flame in the chamber, is defined to be the number of crank angles between CA10 and CA90 (CA10-90).

2.2.1 Multiple-Zone Heat Release Analysis

Further evolution of the single-zone heat release analysis has resulted in multi-zone analysis, dividing the burned and unburned regions of the combustion chamber into individual regions (an unburned region listed as U and an adiabatic, burned core region listed as A, see Fig. 2.2.2)

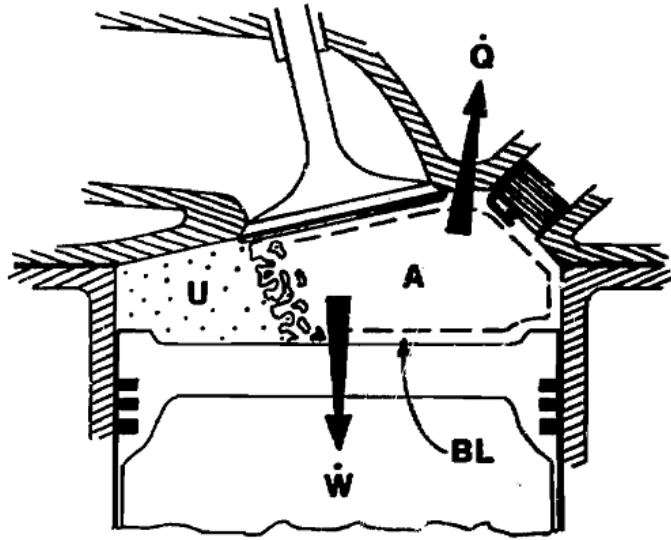


Figure 2.2.2: Two-zone Heat Release Rate Analysis Control Volume (taken from [10])

Other zones can be added for further resolution of the unburned zone (such as the low-temperature regions in the crevice volume near the wall), but the complexity compounds. Multiple zones allow for prediction of emissions (specifically NO_x), but have not been found to provide significantly different combustion phasing parameters. Up to 3° difference in MFB parameters (CA10, CA50 and CA90) has been indicated between a two-zone and single-zone model [11]. Previously

2.2.2 Heat Release Analysis Errors

All heat release calculations rely on accurate in-cylinder pressure data. Minor errors in measurement techniques can lead to erroneous heat release information. Proper calibration of pressure transducers and careful pressure-volume phasing greatly increase the overall accuracy of the data. The greatest source of error has been shown to be in absolute pressure referencing leading up to a 5% error in combustion phasing parameters [12]. Low-speed, light-load operating conditions present the highest error due to the small magnitude

changes in pressure. Literature suggests a minimum of 200 cycles of consecutive data is necessary for proper statistical estimation of pressure data for heat release analysis [12].

2.3 Engine Operating Condition Effects on Heat Release Rate

An engine can run over a wide range of operating conditions with varying speed, load, spark timing and air-fuel ratio. The heat release rate at different engine conditions will vary due to differences in turbulence, combustion phasing or mixture properties. In order to understand the effect of a modified flow field or multiple spark configurations, heat release rate variation due to engine conditions must be quantified.

2.3.1 Engine Speed

Turbulence intensity has been found to scale with engine speed [13], but little improvement is indicated in the HRR, MFB or burn duration on a crank angle basis [14]. Comparing the burn duration on a time basis, increasing engine speed results in a decrease in burn duration as expected [14].

2.3.2 Engine Load

Increasing the load of a throttled engine allows a greater flow of intake charge into the cylinder. A significant advance in combustion phasing can be realized by increasing engine load due to the increased breathing capability of the head and improved charge motion [14].

2.3.3 Air-Fuel Ratio

Flame speed is very sensitive to mixture properties. Lean conditions result in slightly increased burn durations whereas fuel-rich conditions yield slightly decreased burn durations. The fastest combustion occurs around a stoichiometric mixture, but overall the effects of

minor variation in air-fuel ratio have been found to be minor in comparison to other parameters [14].

2.3.4 Spark Timing

Spark timing affects HRR by phasing the combustion event at different points in the cycle. Spark advance for mean best torque (MBT) results in the best performance for a given speed condition due to the optimal pressure phasing of combustion resulting in the highest torque at the lowest fuel consumption. “Advancing” and “retarding” describes the spark relative to MBT timing. Retarding combustion phasing places a significant portion of the combustion in a quickly expanding volume and decreasing turbulence field, resulting in a decreasing burning rate. Further explanation of the effect of retarded spark timing is developed in later discussions (section 2.6) [14]. The spark energy has been found to be an influencing parameter in the early flame propagation in lean-combustion conditions [14].

2.4 Small Engine Emissions Testing

Small engine emission testing is governed by an SAE standard, first established 1974 [15]. The J1088 standard provides a uniform emissions and performance testing methodology for small engines. Measurements are dictated to be conducted at rated engine speed, 85% rated speed and idle conditions with engine loads varying from idle conditions to 100% load. The emissions requirements are divided into various engine classes by displacement and handheld versus non-handheld engines. All emissions measurements are required to be recorded on a mass emissions rate (gram/hour) for CO, CO₂, HC, O₂, and NO_x along with engine speed, brake torque and fuel and air mass flow rates. Currently, small engines are regulated on HC+NO_x and CO emissions [16].

2.5 Dual Spark Combustion

The heat release rate is related to the flame propagation through the combustion chamber. A simple burning rate relation indicates it is a function of the density of the charge (ρ_U), laminar flame speed (S_L) and flame area ($A_{flamelet}$) given the mass burning rates as:

$$\dot{m}_{fuel} = \rho_U A_{flamelet} S_L \quad Eqn. 2.5.1$$

By changing spark location and number of ignition locations in the chamber, the flame area term can be adjusted [17].

2.5.1 Spark Location Effects on Heat Release Rate

The location of initial flame creation influences the life of the flame. Numerous studies have shown central spark plugs provide the highest heat release rates due to the reduced flame travel distance and unrestricted, spherical flame growth with minimal influence of the chamber and heat transfer losses to the wall [18,19]. Side mounted spark plug burn duration was found to increase by 25% with minimal bulk motion conditions in comparison to central locations [18]. With limited bulk motion available to convect the flame, the propagation process has been determined to be a diffusion limited process and therefore dictated by the distance for the flame to travel [19].

Hydrocarbon and NO_x emissions have been found to be related to spark location due to the stark differences in engine operating conditions presented with differing location. The spark plug, a local region of hot temperatures, presents a prime location for NO_x formation and should be placed far from the exhaust valve [20]. Other studies have suggested placement of the spark plug close to the intake valve to allow for the convective cooling effects during intake while retaining favorable spark positions [21].

Hydrocarbon emissions have similar trends of increasing emissions with spark locations placed further from a central location. The unburned mixture stored in the ring-pack has been found to be a significant contributor to small engine HC emission, especially at high-load conditions [22]. Centralized spark locations provide the highest burning rates and relatively higher peak pressures which can result in increased HC emissions due to increased ring-pack loading, but provide higher burn rates. Moving the plug towards the chamber walls presents a cooler ignition region, increasing the quench layer and unburned HC emissions.

2.5.2 Dual Spark Configurations

Dual spark configurations have been investigated by automotive manufactures in order to improve the combustion quality (reduce COV), and to extend the lean limit of a given condition [23]. By increasing the number of spark locations, the probability of an ignitable mixture in the vicinity of the plug increases, reducing the chance for misfire. Low-speed, light-load engine conditions are especially attractive for dual spark plugs due to the reduced charge motion and larger residual providing an unfavorable ignition condition for establishing a stable propagating flame front [23,24].

As shown by Witze, the burn duration increases with spark positions further from the center of the cylinder with minimal bulk motion [18]. Compact, dual spark chambers significantly reduce the flame travel distance and present rapid combustion during the early flame propagation phase (CA10-50). Single spark conditions have similar late flame propagation durations, but overall burn durations (CA10-90) are consistently lower for dual spark configurations [25]. An investigation into this early flame relation through modeling,

revealed early flame interaction of two independent flame fronts significantly reducing any burning rate advantage over a single spark condition (see Fig. 2.5.1) [26].

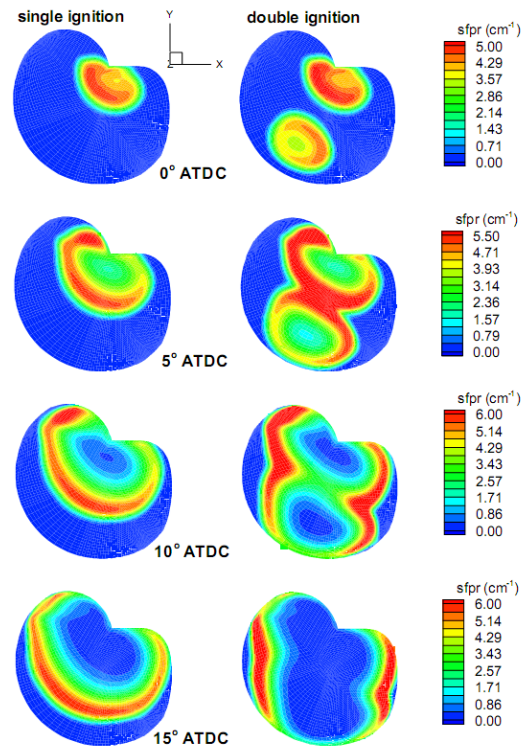


Figure 2.5.1: Early Flame Interaction with Dual Spark Combustion of Flame Surface Density Plots (taken from [26])

The longer the independent flame fronts can exist, the greater the burn duration reduction [26]. The introduction of bulk motion further reduces any burning rate advantage as the flame fronts coalesce earlier in the cycle [24,25].

Heat transfer effects from dual ignition conditions are increased as a greater volume of the combustion chamber interacts with the flame earlier in the cycle. By matching combustion phasing, heat transfer effects are reduced, but advantageous early flame propagation still provides increased heat losses to the walls [26].

Nitric oxide emissions were found to increase with multiple spark conditions. This can be attributed to an increase in local hot regions (spark plug electrodes) and increased initial combustion temperatures (through advanced combustion phasing due to rapid early flame propagation) favorable to NO_x formation [24]. HC was shown to decrease, but extension of lean operating conditions reduces the fuel in-cylinder leading to reduced HC emissions [24,25,26]. The combustion advance presented by dual spark combustion conditions increased in-cylinder peak pressure. As the ring-pack loading is directly related to the peak pressure, an increase in HC is expected for conditions away from the lean limit [22].

2.6 Retarded Spark Timing – Cold Start Conditions

Modern automotive engines are equipped with three way catalysts that significantly reduce engine-out emissions. To properly catalyze the exhaust gas, the catalyst material must be raised to an operating temperature around 300°C . The first 15-20 seconds of exhaust gases can escape the system without reacting due to the “cold” system, and this results in a significant fraction of the allowable emissions [27]. To combat this transient “cold start” behavior, automotive systems employ retarded spark timing strategies placing combustion later in the cycle, where less work can be extracted from the gas, raising the exhaust gas temperature, which quickly raises the catalyst to the operating temperature.

By phasing combustion late in the cycle, the increased exhaust gas temperature and lower peak pressures offer improved HC oxidation and reduced ring-pack effects. Many studies have concluded a minimum temperature of 1500 K is required for HC oxidation with a sufficient OH radical pool [28, 29]. Below this temperature, the chemical kinetics allow

the NO_x formation reactions to compete for OH radicals reducing the effectiveness of the HC oxidation [28].

Since OH is not easily measured, exhaust O₂ concentration is commonly used as a surrogate for determining the radical pool size [28, 29]. The oxidation of hydrocarbons is chemically linked to the amount of CO produced. In HC oxidation, the fuel must breakdown to form CO, which in turn oxidizes to form CO₂, releasing energy in the process. The CO oxidation process is rate limiting, but with the introduction of the OH radical, the process significantly speeds up. In order to form a sufficient OH pool, CO must react with O₂ to begin the reaction steps [30]. Therefore, the greater exhaust O₂ concentration, the lower the amount of CO oxidized and the smaller the OH radical pool.

As spark timing is retarded, load decreases as combustion occurs in a rapidly increasing volume. In order to hold a constant engine torque, air and fuel rates must be increased. Characteristics unique to the retarded spark timing combustion emissions can easily be masked by the mass flow rate increase [29]. When reporting emissions on an emissions index basis (EI), the pollutant is normalized by the amount of the fuel burned [30]:

$$EI = \frac{\text{mass species}}{\text{mass fuel burned}} = \left[\frac{\text{g}}{\text{kg}} \right] \quad \text{Eqn. 2.6.1}$$

Since the fueling rate is increased in retarded spark timing conditions, EIHC will be linearly decreasing with late combustion phasing. Eng suggested these conditions should be reported on a mass per cycle basis in order to include the effects of the increased fueling rates [30].

During slightly rich combustion conditions with retarded spark timing, a plateau develops in engine-out HC mass basis emissions representing a maximum in in-cylinder oxidation possibility (see Fig. 2.6.1).

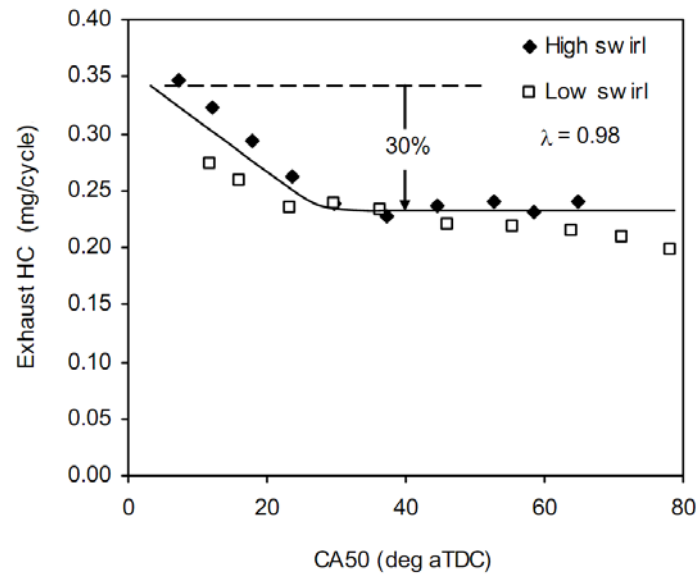


Figure 2.6.1: HC Oxidation Plateau with Retarded Spark Timing Conditions (taken from [29])

The main parameters controlling HC oxidation were found to be CA90 phasing and O_2 concentration. The CA90 phasing is indicative of the out-gassing period for any trapped mass in the ring-pack as the in-cylinder pressure and first ring volume pressure levels equalize. Early out-gassing allows any trapped mass to be fed into hotter exhaust gases increasing the probability of reaction and oxidation.

A critical concentration around 2000 ppm of oxygen represented the minimum concentration required for post-flame HC oxidation [29].

To keep heat release occurring before EVO, charge motion control valves (CMCV) are commonly employed to improve in-cylinder bulk motion in this unfavorable flow condition [31]. Further explanation of these devices and turbulence effects on combustion will follow in subsequent sections.

2.7 Bulk Flow and Turbulence in Engines

Early in the stages of engine evolution, it was quickly determined that intake the motion significantly impacts combustion. Early investigations in the 1930's by Lee at NACA using a high speed camera and goose feathers, discovered that large bulk motion, specifically a swirling rotation about the cylinder axis persisted through compression and is directly related to intake geometry [32]. From this early study, engine design has strived to obtain proper air motion near TDC to aid the combustion process.

2.7.1 Bulk Motion Measurement Techniques

Flow benches and laser-based techniques, such as particle image velocimetry (PIV), are commonly utilized to measure the momentum and flow structure of an in-cylinder flow field. Steady flow setups (see Fig. 2.7.1) are simple, inexpensive and provide a general value of the flow field angular momentum.

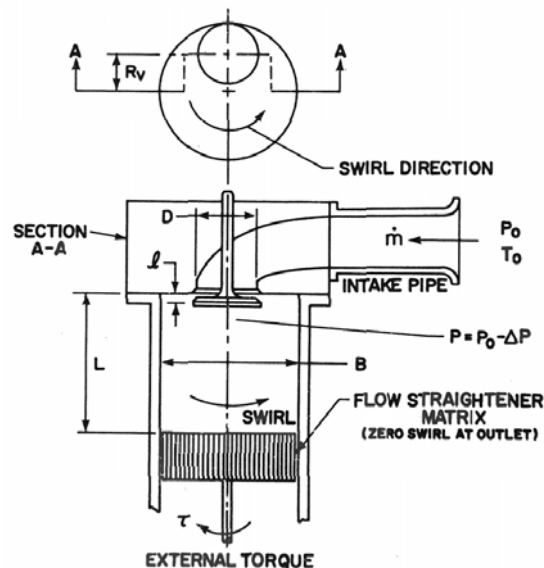


Figure 2.7.1: Common Steady Flow Configuration for Momentum Measurement (taken from [33])

A flow straightener with a strain-gauged torsional shaft in an open ended cylinder is commonly used in the measurement of the angular momentum [33, 34, 37]. Assuming solid body rotation, the torque imparted on the flow straightener is directly related to the angular momentum flux created by the intake geometry [33].

In order to obtain a more detailed view of the flow structures present, a laser-based method must be used. PIV and steady flow experiments conducted on the same engine geometry by Bottom showed the measurement techniques correlated well, especially at high valve lifts [4].

2.7.2 Non-Dimensional Flow Parameters

When characterizing the flow through an engine, non-dimensional parameters such as volumetric efficiency, discharge coefficient, flow coefficient, swirl coefficient and global swirl ratio provide a description of the breathing performance. The use of non-dimensional parameters allows experimenters to remove size effects from the data and compare various designs based on geometry.

2.7.2.1 Volumetric Efficiency

Volumetric efficiency, η_v , is defined to be the measured mass of air ingested during intake over the total mass possible [34]:

$$\eta_v = \frac{m_{Air/cycle}}{\rho_{Air,inlet} V_D} \quad Eqn. 2.7.1$$

Where $m_{air/cycle}$ is the mass of air per cycle, $\rho_{air,inlet}$ is the density of the intake air and V_D is the displacement volume. This parameter describes the breathing effectiveness of the engine. This value is affected by engine geometry (intake port geometry, size, intake valve lift) as well as operating condition (throttle setting, pressure differential across manifold and engine

speed) with high-speed, high-load conditions providing most favorable breathing effectiveness [34]. In order to compare various engines the mean piston speed should be held constant [35]. To improve low-speed, light-load volumetric efficiency, variable valve timing and lifts along with tuned intake manifold strategies have been pursued by automotive companies [34]. Improving the breathing capacity provides a higher intake density therefore influencing the mass burning rate by increasing the density parameter in Eqn. 2.5.1. To further focus on specific performance of the intake port geometry, the discharge and flow coefficient must be calculated.

2.7.2.2 Discharge Coefficient

The discharge coefficient, C_D , is defined to be the measured mass flow rate over the ideal mass flow rate as defined by an isentropic nozzle:

$$C_D = \frac{\dot{m}}{\rho_{mixture} A_{C,i} v_C} \quad \text{Eqn. 2.7.2}$$

Where the characteristic area, $A_{C,i}$ is equation 2.7.3:

$$A_{C,i} = \pi D_{valve} L_i \quad \text{Eqn. 2.7.3}$$

D_{valve} is the inner seat diameter of the valve and L_i is the valve lift. The characteristic velocity, v_C , is defined by a compressible flow velocity equation (equation 2.7.4).

$$v_C = \sqrt{\left(\frac{2\gamma}{\gamma-1} \right) \left(\frac{P_{ambient}}{\rho_{mixture}} \right) \left(1 - \left[\frac{P_{ambient} - \Delta P_{head}}{P_{ambient}} \right]^{\frac{\gamma-1}{\gamma}} \right)} \quad \text{Eqn. 2.7.4}$$

Note that the density of the mixture ($\rho_{mixture}$) must be used to account for the moisture in the intake air. The discharge coefficient is used to highlight low valve lift performance due to

the selection of the characteristic area to reflect the minimum area between the valve and seat lips [37].

2.7.2.3 Flow Coefficient

The flow coefficient, C_F , has a similar definition to C_D , but highlights higher valve lift performance:

$$C_F = \frac{\dot{m}}{\rho_{mixture} A_C v_C} \quad Eqn. 2.7.5$$

The characteristic velocity follows equation 2.7.4 outlined before, but the area defined differently:

$$A_C = \frac{\pi}{4} D_{valve}^2 \quad Eqn. 2.7.5$$

This area is constant across all valve lifts and is based off of the inner seat diameter of the valve (D_{valve}) [37].

When used in conjunction with C_D , the “static flow parameters” allow for a description of the flow restrictions in the system. These parameters are commonly plotted in conjunction with non-dimensional valve lift based off of the inner seat diameter [37].

$$\frac{L}{D} = \frac{Lift}{D_{valve}} \quad Eqn. 2.7.6$$

A common profile of C_D and C_F across the non-dimensional valve lifts are shown in Fig. 2.7.2.

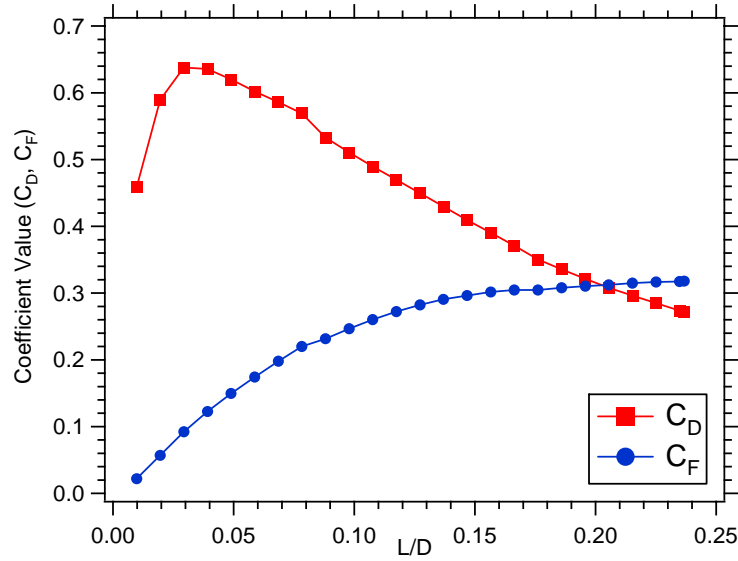


Figure 2.7.2: Response of C_D and C_F with Non-dimensional Valve Lift

2.7.2.4 Swirl Coefficient and Swirl Ratio

The swirl coefficient, C_S , is defined to be the ratio of the angular momentum of the flow over the axial momentum with a length scale:

$$C_S = \frac{8T}{\dot{m} v_C B} \quad \text{Eqn. 2.7.7}$$

Where T is the torque as measured by a steady flow momentum measurement device (see Fig. 2.7.1) and B is the engine bore. This parameter varies with valve lift and can be positive or negative depending on rotation direction.

The global swirl ratio, R_S , is an integrated value and an estimate of the angular momentum of the total flow field during the intake period [38]:

$$R_S = \frac{BS}{n_{valves} D_{valves}^2} \frac{\int_{IVO}^{IVC} C_F C_S d\theta}{\left[\int_{IVO}^{IVC} C_F d\theta \right]^2} \quad \text{Eqn. 2.7.8}$$

Where n_{valves} is the number of intake valves and S is the stroke. This parameter provides one value for the entire valve lift and describes a global angular momentum for the induction process [38].

2.7.3 Bulk Motion and Turbulent Flow in Engines

Large-scale bulk motion with rotation about the central axis is commonly referred to as swirl (see Fig. 2.7.1). A swirling velocity field has been found to survive to TDC better than other intake motion, independent of port geometry [36]. While bulk motion describes flow structures on the order of the engine bore, turbulence describes the smaller, energy-containing vortices that interact with the flame front leading to increased burning rates.

The turbulent flow field is characterized by the turbulent intensity and a length scale. Turbulent intensity, u' , is the root-mean-squared value of the velocity [39].

$$u' \equiv \sqrt{\overline{u^2}} \quad \text{Eqn. 2.7.9}$$

Numerous studies have shown turbulence intensity significantly affects the burn rate in an engine [13, 17, 36]. Turbulent intensity has also be found to scale with mean piston speed (see Fig. 2.7.3) [13, 34].

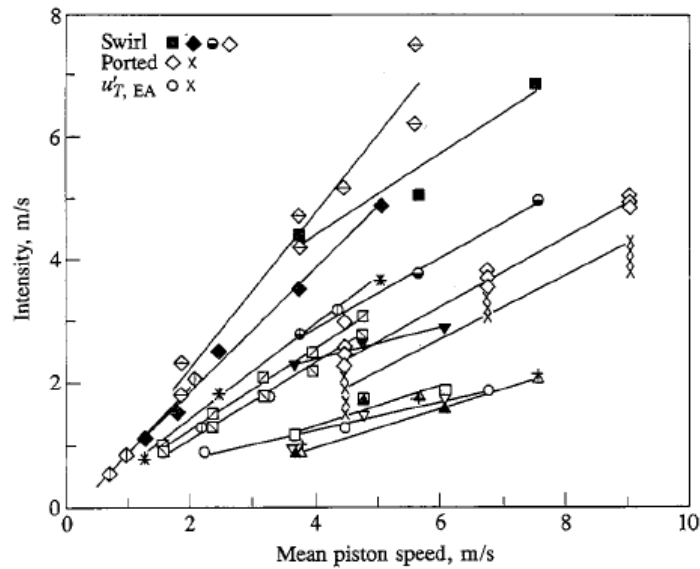


Figure 2.7.3: Turbulence Intensity Scaling with Mean Piston Speed with Various Intake Geometries (data from [13], taken from [34])

The turbulent length scale is the representative size of the turbulent eddies and is

commonly provided as a wave number ($\kappa = \frac{1}{length}$). The greatest length scales are defined

by system boundaries (commonly valve lift) and smallest defined by the lowest kinetic energy before dissipating to heat energy. To quantify the spectra of the turbulent length scales and kinetic energy present, a 1-D spectra model is commonly introduced (see Fig. 2.7.4).

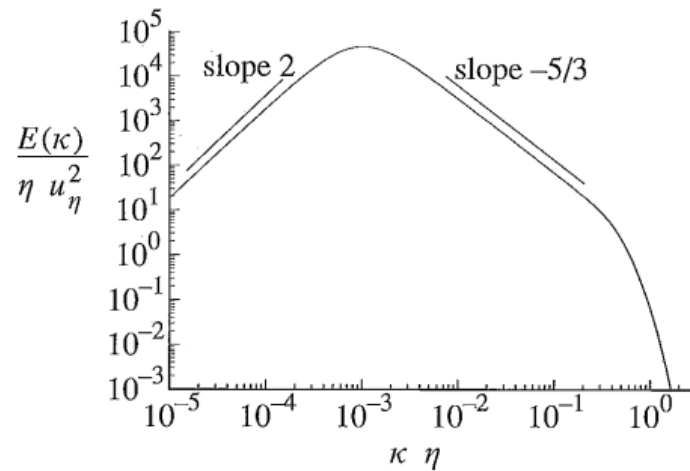


Figure 2.7.4: Turbulent Model Spectrum (taken from [39])

It was found early in turbulent measurement in engines by Semenov that the jet emanating from the intake valve produces a significant amount of turbulence along with creating a bulk motion disturbance [40]. After IVC, degradation of the bulk motion, via compression and viscous dissipation, creates a nearly isotropic, homogeneous turbulent state at TDC [36, 40].

2.7.4 Bulk Flow and Turbulence Effects on Heat Release Rate

In 1940, Damkohler set up a simple experiment using a Bunsen burner to investigate the influence of turbulence on premixed combustion resulting in two major conclusions with bulk flow and turbulence. First, small vortices on the order of the laminar flame thickness ($\sim 1\text{mm}$) increases the flame speed by improving the turbulent mixing process of burned charge and fresh mixture [30, 41]. With flow motion length scales greater than the flame thickness, the flame surface is “stretched” and enlarged increasing the burning rate by increasing the flame surface area (see Eqn. 2.5.1) [41]. From this initial study, many investigators have studied the effect of bulk motion and turbulence on the heat release rate and burn duration.

Increasing swirl has been found to reduce ignition delay (CAIgn-10) and combustion duration (CA10-90) by several investigators [18, 42, 43, 44]. To isolate the influence of swirling bulk motion and changes in kinetic energy of the flow, Mikulec *et al.*, created a variable swirl engine with constant geometry [43]. By modifying the angle of the intake port, the swirl ratio increased without modification to the port geometry. Turbulence intensity was found to increase by 10% and a reduction in CA10-90 by 25%. The reduction in burn duration was attributed to the increase of turbulence intensity [43], which was a similar conclusion to all other studies [18, 42, 44].

Lancaster *et al.* investigated the influence of turbulence on combustion through flame speed ratio calculations. The flame speed ratio (*FSR*) of turbulent to laminar flame speed is a function of the engine geometry, turbulence intensity and reference laminar flame speed [45] :

$$FSR \approx \frac{S_T}{S_L} \approx \sqrt{1 + B \left[\frac{u'}{S_L} \right]^2} \quad Eqn. 2.7.10$$

The true definition of *FSR* is up for interpretation as several studies have found variations on this basis, but all show *FSR* as a function of turbulent intensity and a turbulent length scale.

Emissions have been shown to improve from the addition of swirl due to the improved lean limit characteristics. Also, with an increase in swirl ratio, COV of IMEP was found to drop due to the improved, orderly flow near the spark location [42, 44].

2.8 Combustion Similarity

Similarity investigations are common practice in engineering to reduce the number of experiments to run and the associated costs. Aerospace companies commonly achieve

similarity between full-size aircraft and detailed, scaled wind tunnel models. Simply scaling size does not always obtain a comparable system therefore relationships between non-dimensional parameters, such as the Reynolds number is often required.

Various levels of similarity exist; from simple size scaling to complex force and acceleration similarity between systems. The basic form of similarity, known as *geometric similarity*, concerns the ratio of a length scale from two or more systems resulting in a common scaling factor. This geometric similarity can be thought of as simply scaling a blueprint between various designs. Slightly higher complexity is obtained from *kinematic similarity*, where systems must meet the geometric similarity definition as well as retain equality between system kinematic motions, also based on a common factor. *Dynamic similarity*, the highest complexity, requires the system to meet both geometric and kinematic similarity and hold similarity accelerations between system components based off of a common factor. This level of comparison is difficult to achieve outside of complex parametric computational models, but kinematic similarity can be achieved by simple systems yields a wealth of information between designs [46].

2.8.1 Similarity Studies in Engines

Similarity studies in engines have been previously approached to ease the design of new engines. Purday's diesel engine design text from 1919, first suggested that the use of a similarity condition between engines of varying size and designs at the time "carried out the principle of similarity remarkably closely" [47]. Although the results of the study proposed simple scaling concepts, such as power scaling with the bore cubed [47], it constructed the idea of an equivalent condition between relatively similar designs from the same market. Lichty and Taylor continued this work into SI engines to a varying degree. Lichty

approached similarity from a design approach, but expanded the definition of an equivalent condition. In order to meet geometric, kinematic and dynamic similarity, the bore-to-stroke ratio, mean piston speed, compression ratio and volumetric efficiency should be equal. The jet velocity through the intake valves was determined to be proportional under these conditions. Lichty attributed this velocity as the main contributor to the cylinder flow field and therefore the main scaling influence to obtain combustion similarity [48].

Taylor expanded this work further by including the requirement of matching mean effective pressures [35]. Indicated mean effective pressures (IMEP) is defined to be the useful work output per cycle over the displaced volume [34]:

$$IMEP = \frac{W_{cycle}}{V_D} = \frac{\oint PdV}{V_D} \quad Eqn. 2.8.2$$

This value can also be considered to be the area enclosed the log-P, log-V curve (see Fig. 2.8.1).

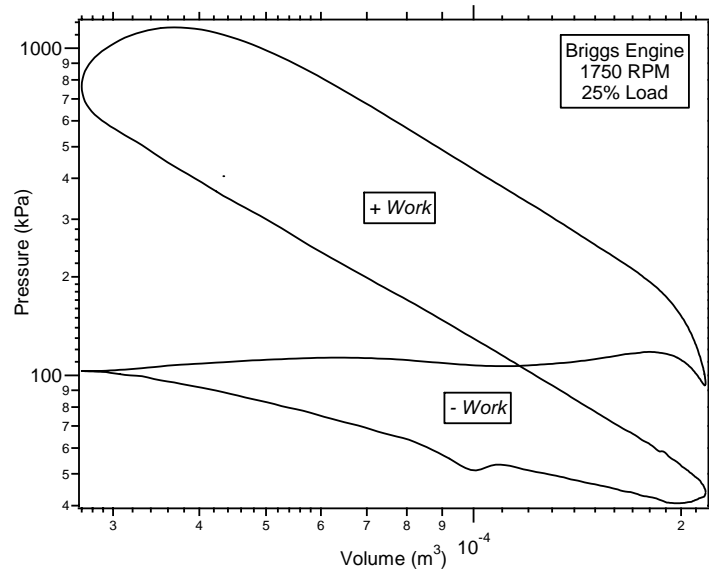


Figure 2.8.1: Log-P, Log-V Plot of an Engine Cycle

The use of IMEP rather than engine torque for an indication of load allows an independence of engine size definition [35].

Where other studies were only parametric arguments of scaling, Taylor conducted experiments on engines of varying size scaled from the same blue-print [35] (see Fig 2.8.2).

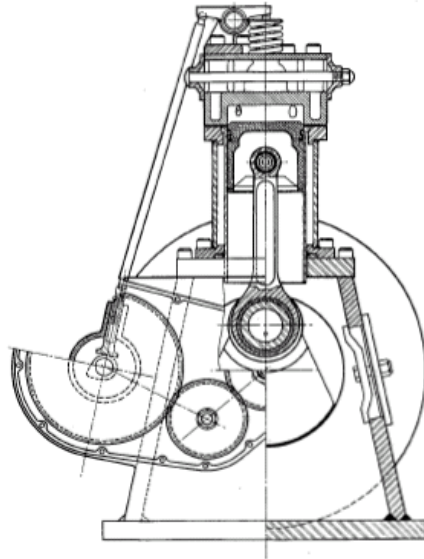


Figure 2.8.2: Technical Diagram of Scaled MIT Engines (from [35])

These MIT engines had varying bore sizes from 2.5 – 6 inches with simple overhead valve combustion chambers and similar intake systems [35].

The investigations were conducted to test the definitions of engine condition similitude and size-relationships on volumetric efficiency. Taylor states engines in the same service category already exist with a high degree of similarity in design and can provide a wealth of information about high efficiency designs. The volumetric efficiency of various engines at different conditions was found to collapse to a single curve there related to the inlet Mach number. This collapse indicated various engines could be compared at a properly defined operating condition; in this case rated engine speed at high-load [35].

The MIT engines were scaled such that a given piston speed would yield equivalent Reynolds numbers. Piston speed is defined to be [34]:

$$S_p = 2SN \quad \text{Eqn. 2.8.3}$$

Where S is the stroke (in meters) and N is engine speed (in cycles/second). This value relates engine speed to the engine specific geometry. This similarity also provided the MIT engines to have nearly identical volumetric efficiency at equivalent piston speeds and intake boundary conditions. Any deviation in η_v would indicate slight offset in the Reynolds number estimation. Taylor concluded, with engine scaled appropriately, the Reynolds number, a measure of inertial to viscous forces on the fluid, did not indicate significant viscous forces. Since these engines were designed with similar intake systems, volumetric efficiencies were able to be matched, but Taylor speculated small intake system geometry differs would be reflected with similarity studies [35].

Brandstetter provided a numerical analysis investigation using the method of characteristics to characterize the main parameters affecting the volumetric efficiency of scaled engines [49]. His numerical model required ten dimensionless ratios (from the geometry of two designs) from dimensional parameters of inlet velocity, ratio of intake volume to displaced volume, compression ratio, connecting rod length, flow coefficient, a modified flow coefficient, IVO phasing, IVC phasing, specific heat ratio and cylinder pressure. Conclusions presented from this study indicated the importance of high flow coefficient values to yield improved breathing through minor changes in the geometry. Late IVC timing was also found to increase volumetric efficiency when IVC was placed about 60°aBDC [49].

Performance scaling with respect to max power at rated speeds has been of special interest to motor sports teams, but largely ignored by commercial manufactures. Using a market data book of given engine information at various operating conditions, it was found that engines with similar bore-to-stroke ratios with relatively smaller bore sizes allowed for reduced flame travel distances and reduced flame quenching [50]. Across a decade of engine data, trends indicated the shift towards these small bore engines improve low-speed breathing. Varying the duration of the intake valve event and tailoring valve lift was also an indicated trend. Prior studies had indicated the higher valve overlap required due to the duration of the intake system was detrimental to combustion duration, quality and HC emission at low piston speeds [51].

A significant portion of the efficiency of smaller engines was attributed to wall heat loss [52]. Eilts investigated the effect of scaling and heat transfer through modeling various engines at scaled bore-to-stroke ratios, connecting rod-crank radius ratios, compression ratios and constant mean piston speed. Through simple estimations, nearly all terms required to calculate charge temperature per cycle were found to be size independent. The influence of the surface-to-volume ratio for various engines was found to be compensated by the effect of engine speed due to the constant mean piston speed assumption. The heat transfer coefficient was found to be highly size dependent due to the temperature profile at the wall. Assuming the Worchni correlation [34] and turbulent flow in a pipe the Nusselt number correlation was found to be inversely dependent on size. This was determined to be the source of decreasing heat loss with increasing engine size [52].

Similarity and parametric studies conducted by the motorsports industry have provided further insight to combustion duration correlation and influence of combustion

chamber geometry effects [53, 54]. Although these studies were presented as benchmarks from which a new engine could be built, the information is still applicable between engines of various designs. The burning duration was found to scale with bore size due to the influence of the piston motion on the in-cylinder flow motion [53]. The influence of size scaling on laminar flame speed and initial flame propagation (CAIgn-10) is highlighted and indicated as a source of significant difference [54]. It was found using the laminar flame definition:

$$S_L = S_{L,o} \left(\frac{T_U}{T_{U,o}} \right)^\alpha \left(\frac{P}{P_o} \right)^\beta \quad \text{Eqn. 2.8.4}$$

Where $\alpha \sim 2$, $\beta \sim -0.12$, and subscript o , is the reference engine values. Through some manipulation, it was determined that the initial flame propagation, or laminar flame speed, is then proportional the compression ratio through [54]:

$$CAIgn - 10 \approx S_L \propto \frac{1}{r_C^{0.54}} \quad \text{Eqn. 2.8.5}$$

On a physical time basis, similar engines provide different trends; physical time was found to scale with bore size at a constant combustion condition [53].

All of the studies pointed towards parametric investigation on engine combustion chamber shape, port design and valve lift profiles to provide the highest breathing ability and fastest burning rate [47, 48, 49, 50, 53, 54].

2.8.2 Combustion Chamber Geometry Effects on Combustion

As presented earlier, spark position is very influential on the combustion rate of a given engine. Various combustion chamber geometries have been found to accentuate certain parts of the combustion process as well. Small engines usually incorporate a “bath-

tub” combustion chamber shape which allows for a simple, overhead two-valve design.

Automotive engines commonly incorporate a pent-roof chamber which allow for significant flow motion and the use of four-valves per cylinder [55] (see Fig 2.8.3).

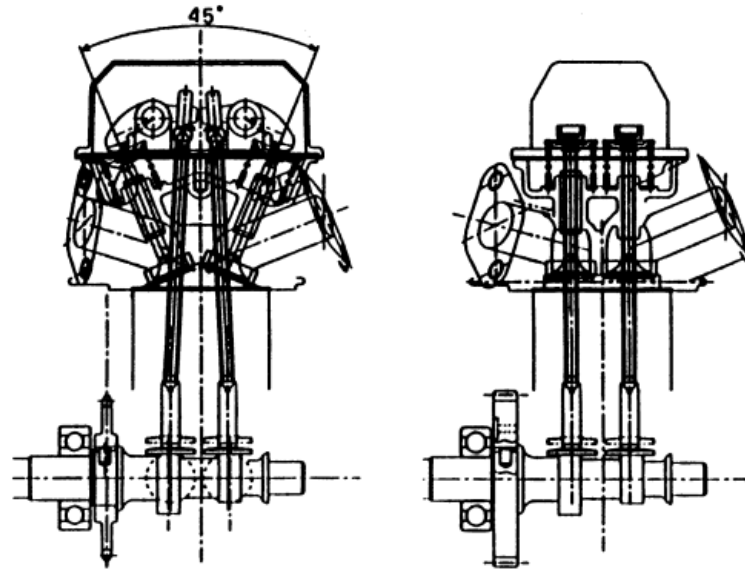


Figure 2.8.3: Pent-roof and Bathtub Combustion Chamber and Valve Arrangement (taken from [55])

In the development of a new small engine with a high burning rate, Mitsubishi investigated the differences between these two predominant combustion chamber shapes using CFD and experimental flow visualization techniques [55]. It was found the bath-tub combustion chamber shape provided a non-symmetrical flow pattern which varied significantly with increasing valve lift whereas the pent-roof chamber provided a consistent, organized flow across the valve lift (see Fig 2.8.4)

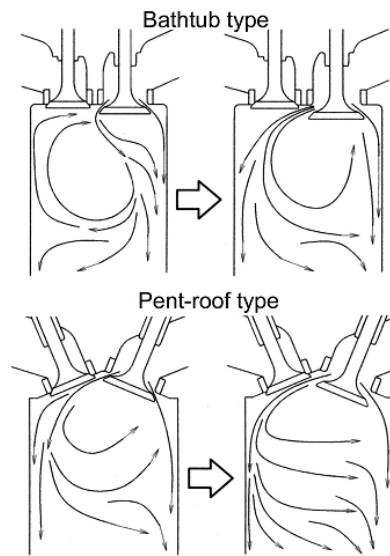


Figure 2.8.4: Variation of In-Cylinder Flow from a CFD Analysis (taken from [55])

The poor combustion duration in comparison to the pent-roof chamber was attributed to this highly variable flow pattern in the bath-tub chamber [55].

It was shown in other studies that for a given compression ratio, the combustion chamber design does not significantly affect the flame speed, but does change the burn rate [10, 56, 57]. Through equation 2.5.1, it was found the combustion chamber shape affects the mass burning rate by way of the flame speed in two ways; by changing charge temperature or turbulence through the cycle [56]. Increasing the compression ratio of the engine increases the charge temperature through the increased in-cylinder pressure during the cycle. Heat transfer from the charge to the chamber walls also provides an influence on the burning rate, removing energy from the system. Combustion chambers with large squish areas or directed valves, such as in pent-roof designs, allow for bulk motion through the entire cycle to TDC. The increased charge motion presents the flame with increased turbulence and increasing the flame front area [56, 57]. Pent-roof combustion chamber heads with 4 valves, a centrally

located spark plug and high compression ratio have been found to yield the best design for the highest combustion rate [34, 50, 55].

2.8.3 Valve Lift and Port Geometry Effects on Combustion

The intake port geometry and valve lift provide the boundary condition of the in-cylinder flow. As described in section 2.7.2.3, the flow coefficient characterizes the high valve lift performance when a majority of the mass flow is inducted to the cylinder [37]. As expected, port designs with the largest port diameter provide the highest flow coefficients [60]. It has been found that identical geometry ports with different scales will provide similar flow coefficients, but will not scale with mass flow rate due to the relative increase in flow obstruction of the valve stem and valve guide as well as increased frictional losses with the smaller geometry [60]. Increasing the flow coefficient has been found to significantly improve the flame speed ratio and reduce burn duration for similar combustion chambers [58].

Positioning the port to allow for an advantageous flow momentum (0° rather than 90° positioning in Fig 2.8.5) provides for an increase in swirling motion while retaining the same port geometry [4, 42].

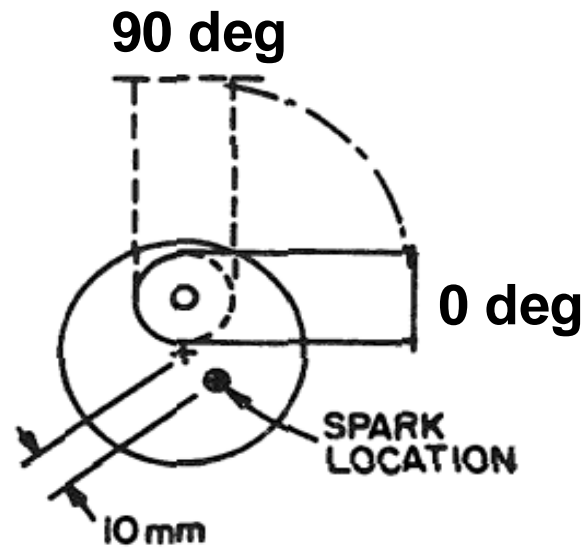


Figure 2.8.5: Port Positioning for Increased Swirl and Similar Geometry (taken from [42])

An investigation by Davis *et.al.*, scaling the turbulence between two engines of varying bore-to-stroke ratio through varying the valve lift provided an interesting view on size scaling and turbulence effects on combustion. By significantly reducing the valve lift, Davis was able to obtain similar turbulence levels throughout compression on two similar engines of varying bore-to-stroke ratios. It was determined the advanced combustion from the under-square engine (bore-to-stroke ratio = 0.8) was due to volume effects [59] (see Fig. 2.8.6)

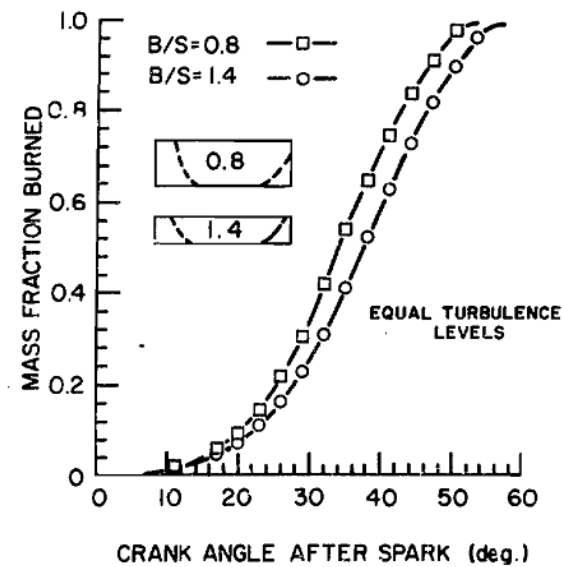


Figure 2.8.6: Similar Engines of Varying Bore-to-Stroke Ratio Combustion Rates (taken from [59])

The engine with the higher bore-to-stroke ratio provided for early flame contact with the piston significantly reducing the flame area therefore reducing the burning rate [59].

2.9 Residual Gas Effects

The use of residual gas, consisting of unburned fuel and combustion products, to improve emissions through exhaust gas recirculation (EGR) and valve overlap phasing strategies, have been investigated by prior studies to improve light-load performance. Many studies have been conducted on automotive engines, but due to significantly different intake conditions, a direct comparison to small engines cannot be assumed. Automotive systems allow for a known vacuum to exist during intake for control of internal residual gas movement. Small engine systems only allow for a vacuum to exist for a very short physical time quickly returning to atmospheric pressure due to the small intake runner volume [61].

2.9.1 Residual Gas Effects on Heat Release Rate

Trapped residual gasses consisting of exhaust gas from a previous cycle reduces combustion temperatures and retards combustion phasing [61]. Conditions with retarded combustion and therefore lower heat release rates were found to result in lower residual fraction in comparison to stock combustion phasing. This effect was attributed to the retarded combustion conditions providing a higher in-cylinder temperature at EVO provide for extra EGR burn up [61].

Haugle found that conditions with the highest diluents were found to produce the longest combustion duration (see Fig. 2.9.1) [62].

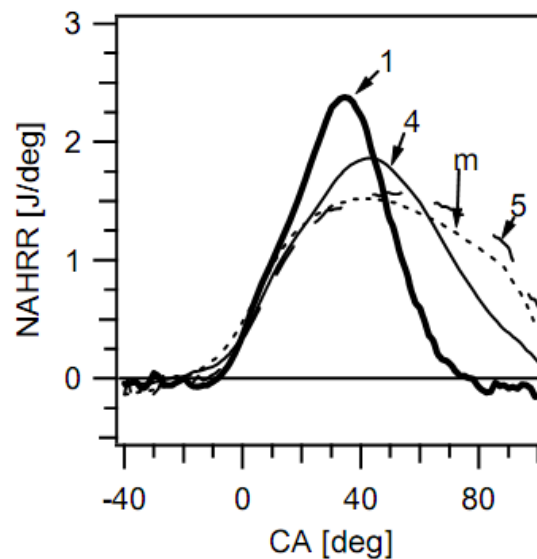


Figure 2.9.1: Increasing Combustion Duration with Increasing Residual Gas (taken from [62]). 1750 RPM, 10% Load; Case 1 – Stock cam, Case 4 – Increased EGR, Case 5 – Max EGR, Case ‘m’ – Maximum Valve Overlap, no extra EGR

It was found that engine speed significantly affects diluent retention and therefore heat release rate [61].

2.9.2 Residual Gas Effects on Emissions

The introduction of a diluent by way of internal retention or external EGR addition, in-cylinder combustion temperatures are reduced therefore reducing the NO_x generation. Retarding the combustion phasing by way of EGR provides for increased exhaust gas temperature and reduced peak pressures increasing the possibility of in-cylinder oxidation of HC and reduced ring-pack effects [62]. As small engines are required to meet HC+NO_x emissions regulations, EGR addition provides a path to reduce both emissions species. Addition of EGR reduces combustion quality, as measured by the coefficient of variance, COV defined as [34]:

$$COV = \frac{\sigma_{IMEP}}{\mu_{IMEP}} \quad Eqn. 2.9.1$$

Where σ is the standard deviation of IMEP and μ is the mean IMEP. Pockets of EGR-rich gas near the spark location provide the possibility of reduced ignitability and delayed combustion phasing and high COV of IMEP. It was found that conditions with high COV did not directly correspond to increased emissions [62].

3.0 Experimental Setup

3.1 Engine Description

All combustion experiments for this investigation involved the use of an air-cooled, single-cylinder, four-stroke, small utility engine. The engine, a Briggs and Stratton Intek™ overhead valve engine (model 128603) is rated at 7.0 HP, which falls under the EPA class of non-handheld class of mobile utility engines (less than 25 HP). The engine specifications are listed in Table 3.1.1.

Table 3.1.1: Briggs and Stratton Intek™ Model 128603 Specifications

| | |
|-----------------------|---------------------|
| Bore | 68.33 mm |
| Stroke | 51.82 mm |
| Connecting Rod Length | 85.52 mm |
| Displacement | 190 cm ³ |
| Compression Ratio | 8.0:1 |

The stock head has been modified with provisions for a pressure transducer and an alternate spark plug location (see Fig. 3.1.1).

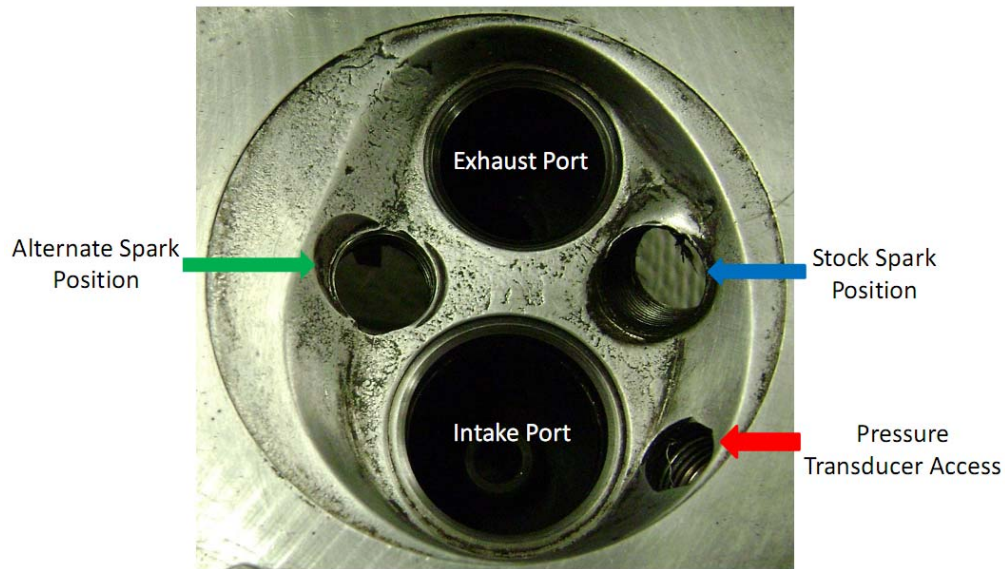


Figure 3.1.1: Modified Intek Head

The alternate spark location is diametrically opposed to the stock spark position, but still within the “bathtub” recess. The pressure transducer access allows for a flush mounting of the sensor in the chamber.

3.2 Engine Control System

The engine was controlled through the MotoTron suite of hardware and software. This system controlled the fuel injection, spark timing, spark energy, and throttle position. The engine control unit (ECU) is based on the Motorola PCM0312M processor. A peripheral wideband universal exhaust gas oxygen sensor (UEGO) and analyzer was used as an input to the ECU to allow for closed-loop control of the fuel injector.

The software used to build the control interface was developed through a MotoHawk toolbox for the Matlab Simulink language. Once the model was developed in Simulink, a Green Hills compiler (Multi2000 compiler v.3.5) assembled the setup files used in MotoTune,

the MotoTron control software package. MotoTune (v.8.13.5.580) communicates in real-time with the ECU via a controller area network (CAN) bus for fast, effective control.

To time the ECU to the engine, a 60-6 tooth trigger wheel rotates on the crankshaft and a half-speed wheel is used to replicate the camshaft speed

3.3 Ignition System

MotoTron ignition coils (SmartCoil 883778), an inductive coil ignition system, were utilized for both spark positions during all tests. As stated earlier, the spark timing and spark energy are controlled via the ECU. This system allowed both spark plugs to be fired independently or simultaneously with similar spark energies and timing.

Due to space limitations, the two spark plugs were not the same model. The alternate spark plug was drilled and tapped below the rocker arm and valve spring base plate therefore requiring a shorter plug. The stock spark position used the stock plug, a Champion RC12YC, and the alternate spark position used a shorter Champion RDJ7Y. A spark plug gap of 0.51mm was used to reflect the stock setup from the manufacturer. The ignition coil can provide a spark energy ranging from 5mJ to 85mJ. During all tests, the spark energy was held at a constant 50mJ to match the average magneto energy [63]. This required the coil dwell time to float based off of the provided battery voltage and desired spark energy, which was controlled by the MotoTune control software.

The stock spark timing was determined by matching the combustion performance of the engine magneto system. Spark timing was varied for the experiments via the MotoTune control software package and was monitored through the TTL signal output from the ECU to

the ignition coils. The spark timing was determined to be accurate within $\pm 0.25^\circ\text{CA}$ of desired spark timing.

3.4 Engine Dynamometer, Torque Sensor, and Shaft Encoder

All experiments were conducted using a vertical shaft, free-floating, DC engine dynamometer (Cox Instruments Model 83274). The dynamometer provided the engine with motoring and energy sinking capability. A Reliance controller allows the user to vary the engine speed. Engine speed was controlled to ± 5 RPM for motored tests and ± 10 RPM for fired tests.

A load cell (Interface Corporation Model SSM-AJ-250) is fixed to a stationary mount and to a 0.3 m torque arm. The load cell is an S-shaped link, utilizing strain gages to allow for steady-state measurements of the torque. A Newport INFCS strain meter converts the load cell strain gauge outputs to voltage measurements read into the National Instruments data acquisition system. Steady-state engine load from the torque measurements was determined from an average of five to seven minutes of recorded data through a National Instruments DAQ system. The engine load determined from the torque is also compared to the IMEP, calculated from the in-cylinder pressure data.

The angular crankshaft position was determined by an optical shaft encoder (BEI Model xH25D-SS-360-ABZC). The encoder output had a resolution of 1°CA and is routed through a buffer box for electrical isolation. Output signals from the encoder occur once per CA (A- and B- pulses) and once per revolution (Z-pulse). The Z-pulse is in phase with engine TDC as determined by using a dial indicator to find the piston position. Engine speed is displayed using a Newport P600A tachometer at the control panel and through an ECU input to the MotoTune control software.

3.5 Fuel System

The engine setup has two fuel delivery systems; a modified carburetor and a homogeneous mixing system (HMS); only the latter was used in this study (see Fig. 3.5.1 for a layout of the fuel and air systems of the test cell).

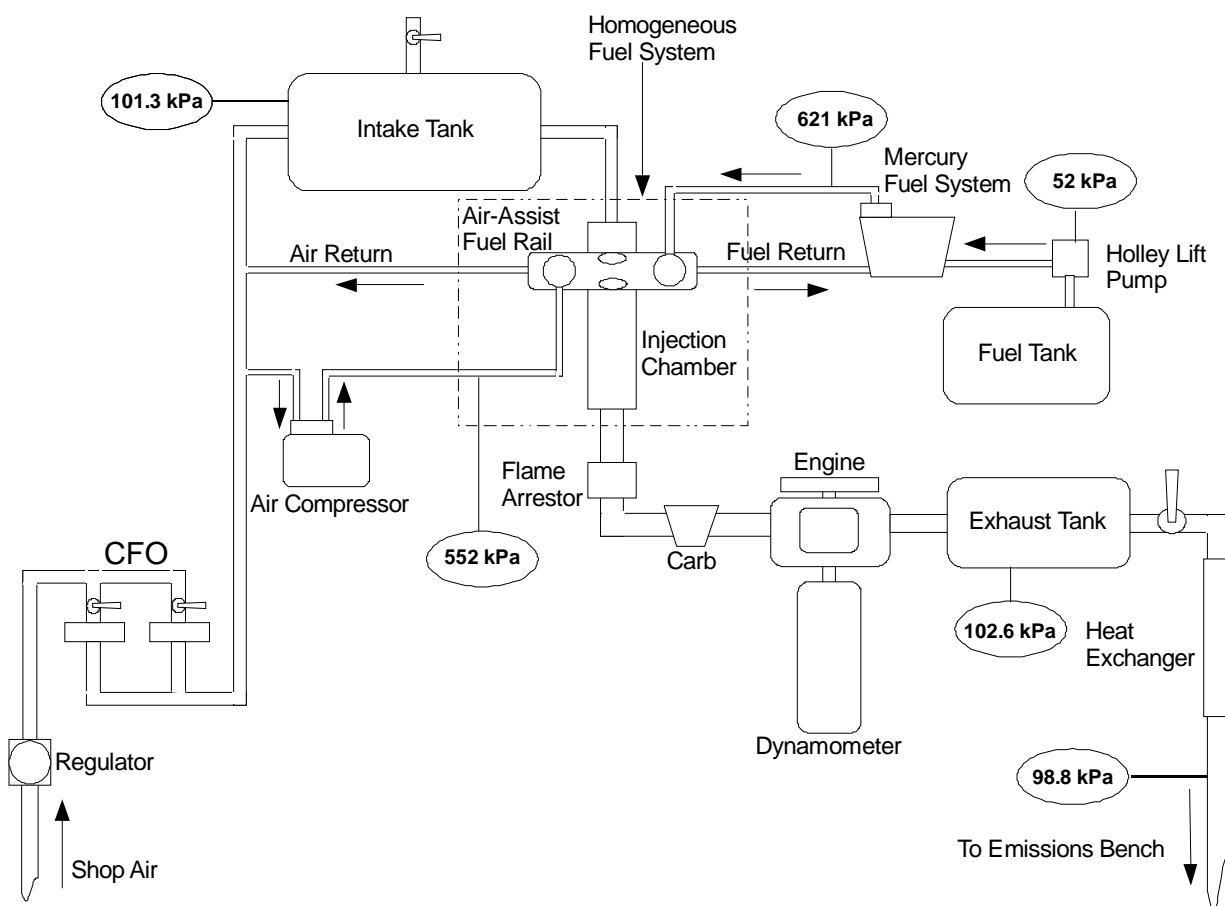


Figure 3.5.1: Test Cell Fuel and Air Layout

From the fuel tank, a low pressure Holley lift pump provides the fuel to the high pressure Mercury Marine fuel pump assembly with a built in filtering system. A differential regulator modulates the fuel pressure generated by the high pressure pump, which required an external air supply from an oil-less Thomas air compressor (model LGH-310). With this system, the fuel pressure at the fuel rail, was typically 69 kPa greater than the supplied air pressure. The

maximum air pressure supplied to the system is limited to 552 kPa gauge and a maximum fuel pressure is limited to 621 kPa gauge. The high pressure fuel is then diverted to the Orbital HMS system which houses the air and fuel injectors. An air and fuel overflow return closes the loop back to the upstream side of the high-pressure pump [1].

The fuel used for the experiments is a US EPA Tier II EEE Certification Fuel (HF0437) with specifications listed in Table 3.5.1.

Table 3.5.1: EPA Tier II EEE Fuel Specifications

| | |
|----------------------|------------------|
| Lower Heating Value: | 42973 [kJ/kg] |
| H/C Ratio: | 1.864 |
| RON: | 96.2 |
| MON: | 87.8 |
| Octane: | 92 |
| MW_{fuel} : | 13.89 |
| AF Stoichiometric: | 14.56 |

The experimental air-fuel ratio was calculated from the exhaust emissions measurements and the measured air flow rate from the choked flow orifices (see section 3.6).

3.5.1 Homogeneous Mixture System

The purpose of the homogeneous mixture system (HMS) was to provide a heated, vaporized, homogenous charge to the engine. This allows for a more consistent charge mixture without any stratification effects. The HMS includes an Orbital fuel rail, fuel injector chamber (FIC) and heat tape.

The Orbital fuel rail is an aluminum housing providing a mounting point for the fuel and air injectors, controlled via the ECU, as well as differential pressure regulators and an air pressure regulator. The injectors provide a vaporized fuel stream at a 45° angle to the air

flow of the FIC. The start and end of the air injection was fixed at 60° and 30° bTDC with a constant fuel-air-delay of 4ms. The duration of the fuel injection signal was dependent on the desired air-fuel ratio. The heat tape temperature was varied to keep a constant intake temperature at the throat of the venturi of 52° C for all conditions. This system was located 1 meter upstream of the engine and therefore the fuel and air injection had no impact on the operating condition.

3.6 Air Delivery System

Air was supplied to the engine from building compressed air system. This system was used to supply the engine with air, control the intake pressure, and measure absolute airflow through a choked flow orifice system. The air supplied by the UW Physical Plant is dried and filtered to remove moisture and oils. Prior studies indicated low relative humidity levels in the air supply. The compressed air properties were found to be an average temperature of 20° C, a supply pressure of 690 kPa gage and a dew point temperature of 4.4° C.

A regulator and a choked flow orifice (CFO) manifold allow for the accurate determination of the air mass flow rate to the engine. The regulator also allows the user to modulate the intake upstream stagnation pressure supplied to the CFO system. The CFO's are placed in parallel to reduce any pressure losses along the path to the engine (see [1] for calibration).

Downstream of the CFO manifold, a small throat venturi has been installed to allow for the use of an external loop EGR system (not used in this study). The air then enters an intake surge tank designed to meet the SAE J1088 standard [15] (100 times engine

displacement) to dampen any pressure pulsations. This allows for the intake pressure and flow to be constant allowing for greater engine stability during engine measurements.

Heater tape wrapped around the intake tank and fuel injection chamber (FIC) was controlled with an Omega temperature controller (Model CN132) to hold a constant intake temperature.

3.7 Exhaust System

The engine exhaust is vented through a modified exhaust manifold to a mixing tank and eventually to a building exhaust line. An emissions sampling tube is connected from the mixing tank running to the emissions bench and complies with the SAE J1088 regulations. The steel mixing tank has been plumbed for an external EGR loop (not used for these experiments), thermocouple ports, and pressure ports to determine engine back pressure. A globe valve at the exhaust tank exit allows the experimenter to modulate the exhaust back pressure to hold a constant pressure drop across the engine. In these tests the exhaust was maintained at 1.25 kPa (5 inH₂O) above the intake pressure. This value was selected to reflect prior experiments requiring higher exhaust pressure to drive an external exhaust gas recirculation system [1].

The modified exhaust manifold has provisions for thermocouple ports and an O₂ sensor. The steel pipe is connected to a flexible metal hose that directs the flow into the steel mixing tank. The hard steel pipe has a diameter of 2.54 cm which connects with a 3.81 cm exhaust diffuser with 50 radially drilled holes to equal twice the flow area. The exhaust gas thermocouple is placed 10 cm downstream with no viewing angle of the exhaust port. An

Horiba O₂ sensor (UEGO Model KX-721030F) is installed 25cm downstream of the exhaust valve.

3.8 Pressure Transducers

The accuracy of the in-cylinder pressure measurements during combustion events is critical for accurate heat release measurements. A fast-response, liquid-cooled, piezo-electric Kistler Model 6061 pressure transducer was used to measure the in-cylinder pressure, while a MotoTron MAP sensor (MotoTron 881879-9) measured the intake manifold pressure. The Kistler transducer signal was amplified and converted to a voltage signal by a Kistler Model 5010 charge amplifier. The charge amplifier was set at a sensitivity of 2.00pC/MU and gain of 50MU/Volt with a long time constant for all experiments. Both transducer voltage signals were measured and recorded with a high speed data acquisition system.

Calibration of the in-cylinder pressure transducer, along with all viable components, was accomplished by a dead weight tester. The gain was applied to the voltage signal in the high speed data acquisition system. The factory calibration of the MAP sensor was confirmed. The MAP transducer was found to have an acceptable response with a first order time constant of 0.87ms.

Calibration data of the in-cylinder and MAP pressure transducers are provided in Appendix A.1.

3.9 Air-Fuel Ratio Analyzer

The air-fuel ratio (AF) was determined using two methods; an Horiba oxygen sensor and through mass-based emissions sampling. The accepted and reported value for a given

condition was the exhaust emission samples, but the O₂ sensor provided the closed-loop control for the engine. The O₂ sensor used was a Horiba Mexa-110λ air-fuel analyzer with a heated universal exhaust gas oxygen (UEGO) sensor (Horiba Model KX-721030F).

The analyzer was calibrated to ± 0.3 at AF 12.5 with a prior experimenter at full load, 3060 RPM using the HMS fueling system. This range varied depending on the AF with a minimum at stoic, but all experiments were conducted around an AF 12. Again this sensor was used as an indicator for control rather than measurement in determining the actual AF for a given condition.

The output of the analyzer is a linear DC voltage from 0-1V in proportion to measured AF. Since this value was used for the closed-loop control over the fueling rate, the output signal is used to adjust the fuel injection pulse width compared to the desired AF provided by the user input in MotoTune.

3.10 Horiba Emissions Bench

The exhaust emissions were sampled using a Horiba emissions bench consisting of five gas analyzers for unburned HC, NO_x, CO, CO₂ and O₂. The HC analyzer (FIA-23A) utilized a flame ionization detector (FID) with an amplifier output (OPE-435). The NO_x analyzer (CLA-22A) is a chemiluminescent based analyzer with an amplifier output (OPE-235). The CO and CO₂ analyzers were identical non-dispersive infrared (NDIR) analyzers (AIA-23) with OPE-115 and OPE-135 output amplifiers. The O₂ analyzer (MPA-21A) is a paramagnetic analyzer with an amplifier output (OPE-335). The analyzers and amplifiers are housed in a non-EGR Horiba Emissions Bench (FWO-1432).

All emissions were measured on a dry mass basis. To ensure the exhaust gas sample from the engine was free of any moisture, the sample was first cooled in a heat exchanger supplied with city water. Downstream of the heat exchanger, a filtered trap collected any condensed liquid and large exhaust particles. A Teflon line from the filter trap to the emissions bench supplied the sample to analyzers. A gas sample was drawn from the exhaust surge tank via a vacuum pump to another bath (held near 0°C) in the emissions bench. The vacuum manifold pressure was held at a constant 62 kPa gage to allow for the proper flow rate required for the analyzers. After passing through another set of filters, the gas sample flows through a rotameter for each of the analyzers.

Before drawing an emissions sample, each analyzer was zeroed and spanned using calibration gases to ensure a proper reading. The voltage signal from each amplifier output was read into the DAQ system for real-time display through a Labview virtual instrument.

3.11 Engine Data Acquisition and Processing

To acquire the necessary pressure and emissions data to determine the heat release, two data acquisition devices were required. The in-cylinder and MAP pressure signals were sampled by a Hi-Techniques Win600 high-speed 4 channel, 12-bit system recorded on a 1° CA basis (limited by the encoder) with a 2MHz sampling rate. This system allowed for up to 200 cycles of data to be recorded for each condition. To trigger the DAQ system, the encoder A- and Z-pulses were used as inputs for the angular position and TDC reference signals respectively. The binary data file from this system was post-processed with a Wavemetrics Igor-based program to peg and averaging the pressure signals to obtain an

ensemble average pressure. The program also calculated the IMEP, COV of IMEP, peak pressure, and location of peak pressure for each of the recorded cycles.

A National Instruments Compact-DAQ chassis (NI c-DAQ-9172) with two NI-9211 thermocouple modules and a NI-9205 differential voltage module was used to record the engine thermocouples, torque voltage signal and emissions bench analyzer output voltage at 20Hz, down-sampled to 1Hz, for five to seven minutes per condition. A Labview virtual instrument allowed the user real-time values of AF ratios, mass flow of air and fuel, air and fueling rates per cycle, combustion, thermal, and volumetric efficiency, oil, intake charge, and exhaust gas temperature, as well as the corrected brake specific (BS), emissions index (EI) and raw values (ppm or percent concentration) of the emissions. The calibrations of the gas analyzers were applied in this program to allow for the recording of the corrected emissions values. Output of the sampling system was post-processed using a Matlab program that collects all recorded samples and outputs an averaged value in tabular format for easy data management and plotting.

The heat release was calculated using the cylinder pressure, air and fuel flow rates, intake and exhaust gas temperatures, and combustion efficiency of a given condition through a Matlab program developed by a previous student [2]. The output of the program provided the heat release rate, cumulative mass fraction burned, and heat transfer rate for each condition.

A ring-pack heat release and single-cycle heat release program provided further insight to the crevice mass and single-cycle influence of the system and was a variation on the Matlab heat release code described above [2].

3.12 Steady Flowbench

The steady-flow experimentation of this investigation was conducted on a SuperFlow 600 Flowbench outfitted with a swirl adapter to measure the angular momentum of the flow (see Fig 3.12.1 of the head and swirl adaptor attachment and Fig. 3.12.2 for the flowbench setup).

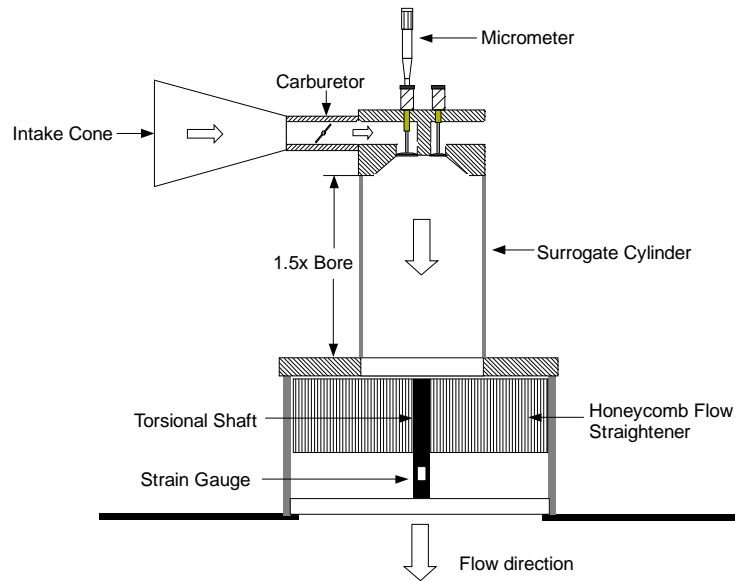


Figure 3.12.1: Engine Head and Swirl Adaptor Arrangement

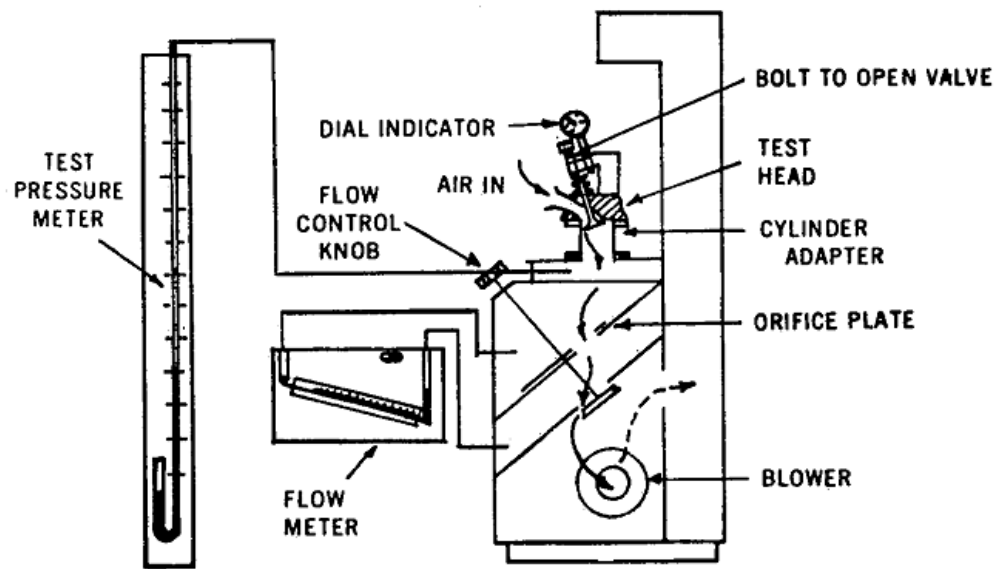


Figure 3.12.2: SuperFlow 600 Flowbench Setup (taken from [64])

The flow bench was capable of measuring flows up to 600 cfm with an accuracy of $\pm 0.5\%$ of the full scale. Six sharp-edged orifices allowed for the selection of a flow range. All of the tests were conducted using the first and second flow range, capable of 38 and 75 cfm, respectively. The airflow was pulled through the head and intake port configuration. The pressure drop across the head was controlled by the experimenter and was indicated by a 1.22 m water-filled manometer (test pressure meter in Fig. 3.12.2). The pressure drop was held constant at 9.96 kPa (40 inH₂O) for each condition. The selection of the pressure drop is an important factor in the value of the flow parameters and measured torque of the flow and is discussed in section 4.2. A water-filled inclined manometer (flow meter in Fig. 3.12.2) indicated the percent of full scale flow allowed for a selected flow range.

The engine valve lift was controlled by a modified Vernier caliper. Conditions were measured at 0.01 inch lift increments and at 25, 50 75 and 100% valve lift. Due to the relatively weak springs, the stock engine springs were retained for all tests. An intake cone attached to the carburetor/head intake system provided a smooth inlet.

3.13 Swirl Adapter

A swirl adapter was utilized for all of the flow bench tests to measure the angular momentum of the flow while providing a negligible pressure drop across the instrument. Any significant pressure loss across the instrument would be reflected in a change in the mass flow rate (see Fig. 3.13.1).

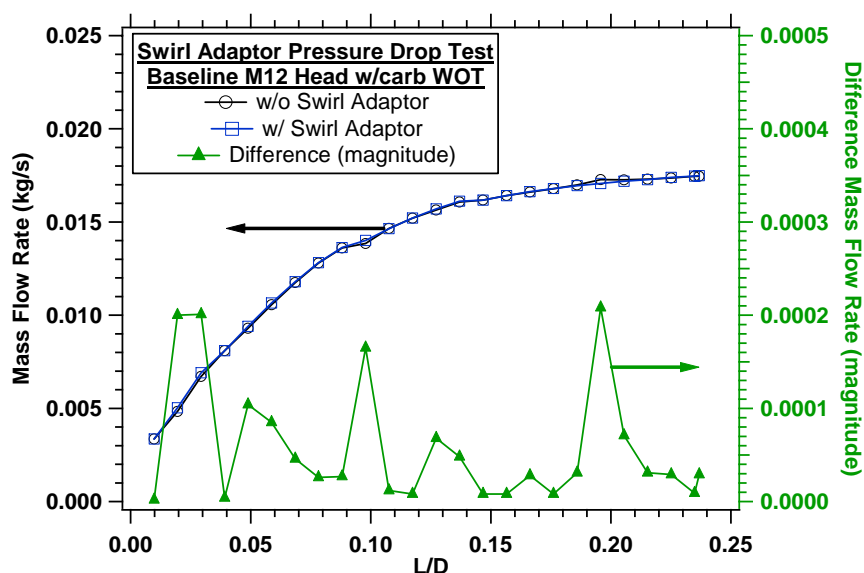


Figure 3.13.1: Negligible Flow Modification Due to Swirl Adapter

Since the difference in mass flow rate from tests with and without the adapter is within the error measurement of the flow bench, the adapter was left in place for all steady flow tests. In order to obtain a coherent vortex, a cylinder of diameter equal to the engine bore having a length of 1.5 times the bore was affixed downstream of the head. This surrogate engine cylinder centers the vortex axis of rotation without significantly degrading the angular momentum by friction. A high aspect ratio, flow straighter at the inlet to the swirl adaptor absorbs the small angular momentum and the resulting torque deflects a rigidly attached polycarbonate shaft. The polycarbonate shaft material was selected to have a large torsional

deflection under small applied torque. Two torsional strain gages (Vishay/Micro-Measurements CEA-13-062UV-350) are placed on opposing sides of the polycarbonate shaft to measure small deflections related to the flow. Each gage consisted of two complete grids set at 45° inclination to create a full Wheatstone Bridge (see Fig. 3.13.2)

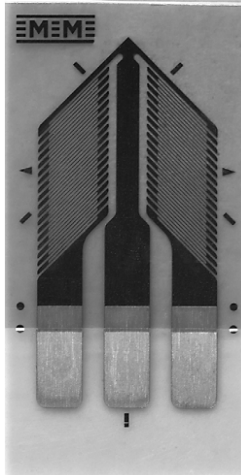


Figure 3.13.2: Strain Gage Pattern

The 350Ω gages were placed vertically (as shown in Fig. 3.13.2) to read a torsional deflection in the horizontal direction.

A strain gage amplifier (Omega DMD-465 Bridgesensor AC Powered Signal Conditioner) provided the excitation voltage as well as a method to electronically zero and span the system. The potentiometer used to span the system was set to provide a test voltage for a 10 gram weight on the dead weight tester of 1.9V. The excitation voltage for all tests was set to 12V with 100 mA supplied to the gages. A 15Ω resistor provided for a 4x external gain on the output amplifier.

A dead weight tester, consisting of a spindle, light weight monofilament, low-friction pulley hardware and two calibrated weight sets, provided the method to calibrate the swirl

adapter. With the calibrated weights and the diameter of the spindle, the applied torque is determined by equation 3.1.

$$TQ[Nm] = \frac{D_{spindle}[m]}{2} * 9.81[m/s^2] * \{(m_1[g] + m_2[g]) * 0.001 \frac{kg}{g}\} \quad Eqn. 3.1$$

Torque is applied in clockwise and counterclockwise directions and the test voltage from the amplifier is recorded to yield a linear calibration curve. This method was found to provide a torque response with accuracy of ± 0.002 Nm for both directions.

3.14 Flowbench Data Acquisition

Due to the minimal amount of flow motion generated by the stock Briggs head, measurement of the proper voltage output from the strain gages requires accurate measurement of small voltage changes. In order to obtain a clean signal, the test voltage was recorded with a National Instruments Compact DAQ (NI c-DAQ-9172). A NI-9205 differential voltage module and NI-9211 thermocouple module measured the test voltage and ambient temperature with real-time output through a Labview virtual instrument. The test voltage was recorded for 50 seconds per valve lift at 100Hz to obtain a repeatable time-averaged voltage.

In order to obtain the proper fluid conditions of the air through the system, the atmospheric pressure and relative humidity were also measured with an ambient pressure gage and digital hygrometer.

The flowbench and test voltage data were post-processed through a Matlab program to determine the non-dimensional flow parameters and global swirl ratio.

4.0 Steady Flow Characterization

4.1 Introduction

This chapter will present data collected during the steady flow experiments performed on the Briggs Intek head using a variety of flow field enhancement methods. The determination of the operating conditions, calibration and experimental methods of the steady flow bench will be presented.

4.2 Basic Flow Measurement

In order to obtain basic performance measurements of an engine head, a steady flow bench is used to measure the mass flow through the engine head and intake system for a given valve lift. A constant pressure drop is usually held between the vacuum chamber of the flow bench and the ambient pressure. To adjust the flow rate through the head, various orifice plates can be selected. Measuring the pressure upstream and downstream of the orifice plate defines the “percent flow” through the given orifice. By knowing the pressure differential across the head, the percent flow, and orifice plate diameter the volumetric and mass flow rates can be determined for a given valve lift. Through measurement of the output voltage from the strain gage amplifier, the angular momentum flux of the flow field can be determined. A counter-clockwise (CCW, looking down on the bore) torque value represents a positive swirl coefficient and a clockwise (CW, looking down on the bore) torque a negative swirl coefficient. The ambient pressure, relative humidity and intake temperature must be measured to determine the properties of the air. A micrometer provides the measurement of and method to change the valve lift. All of these measurements are required

to define non-dimensional flow parameters. Calculation of these parameters from recorded data was conducted by a Matlab code provided as Appendix A.2.

4.3 ΔP Selection

Although considered trivial for most systems, the ΔP selection was found to be extremely important in this experiment. The selection is commonly based on tradition; 10 inH₂O and 28 inH₂O are the most common values [37]. The only universal criterion for ΔP is the guarantee of turbulent flow ($Re > 2300$) through the port to ensure a fully developed flow representative of engine conditions [37].

The ERC SuperFlow flow bench creates a vacuum downstream of the head therefore the flow begins in the room and flows through the head to the bench. The system was run at a range of pressure drops from 10 inH₂O – 45 inH₂O. The goal of the pressure drop tests was to obtain a consistent, repeatable swirl coefficient data (refer to eqn. 2.7.7) and to characterize how this would affect the flow coefficient (refer to eqn. 2.7.5).

All pressures and valve lifts (25, 50, 75, 100% of max lift) were randomized to provide three points for each selected pressure and lift. Performance at max lift will be presented, but trends were consistent at other lifts. All tests were conducted with the stock Briggs head, carburetor and an intake cone.

The ΔP selection significantly affects the mass flow rate as expected. The mass flow rate change translates into a significant trend in C_F at max lift (see Fig. 4.3.1)

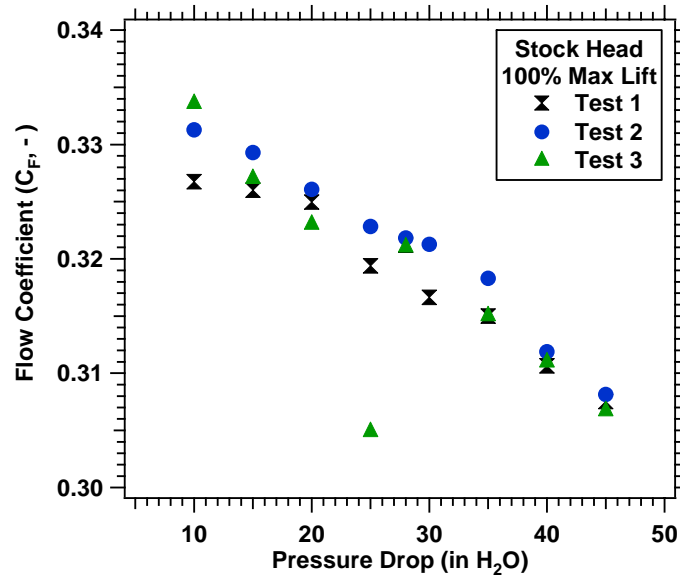


Figure 4.3.1: Flow Coefficient Response with Varying Pressure

This is to be expected as C_F highlights high lift performance.

Higher ΔP was found to produce a convergence of the swirl coefficient at high valve lift (see Fig 4.3.2). Because of the low flow rates, the torque measurement was susceptible to error. The higher flow rates with ΔP at 40 inH₂O mitigated these effects.

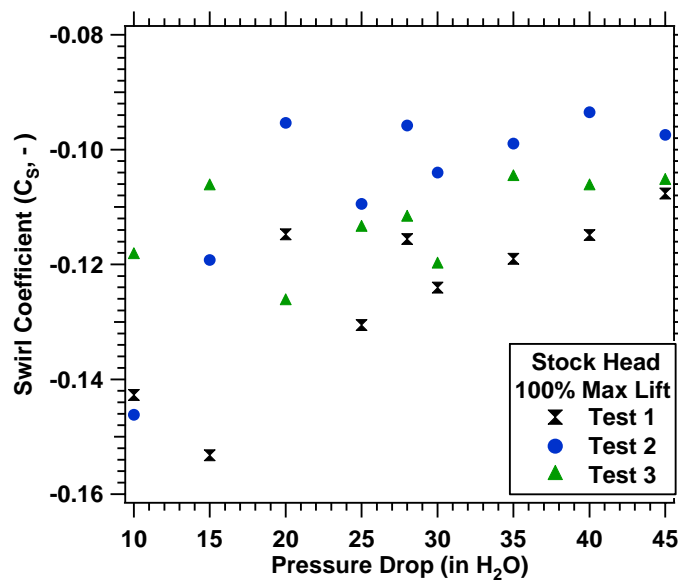


Figure 4.3.2: Swirl Coefficient Convergence with Increasing Pressure Drop

4.4 Data Acquisition

The small flow rates and momentum through small engine heads presented unique challenges for accurate data acquisition. An NI/Labview system was created to measure the variable voltage output from the swirl adaptor stain gauge amplifier. To gain confidence in the voltage output from this amplifier, a concentric orifice plate was created to act as a blockage to provide a given flow rate with zero assumed swirl. The orifice plate was placed at the top of the surrogate cylinder with the orifice positioned in line with the axis of the swirl adaptor, therefore the flow should have no measurable momentum (see Fig. 4.4.1).

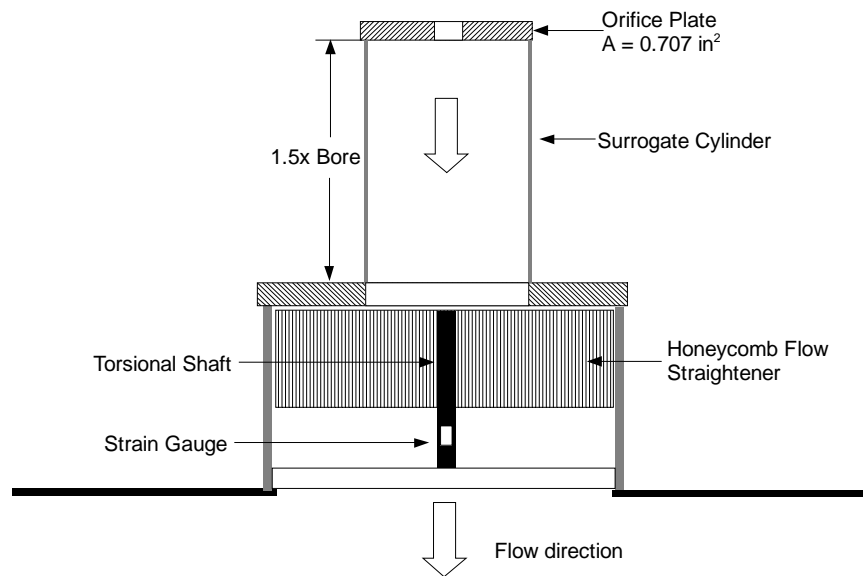


Figure 4.4.1: Orifice Plate and Swirl Adaptor Attachment

The orifice hole was sized to an area equal to the curtain area of the valve at maximum lift. This method also provided a check on the Matlab code calculating the flow parameters (C_D , C_F , etc., see Appendix A.2) as a circular hole in a flat plate theoretically will yield a $C_D \sim 0.6$ [66].

It was found that the orifice plate gave a swirl coefficient independent of the ΔP at an order of magnitude below the stock head maximum swirl condition (see Fig. 4.4.2).

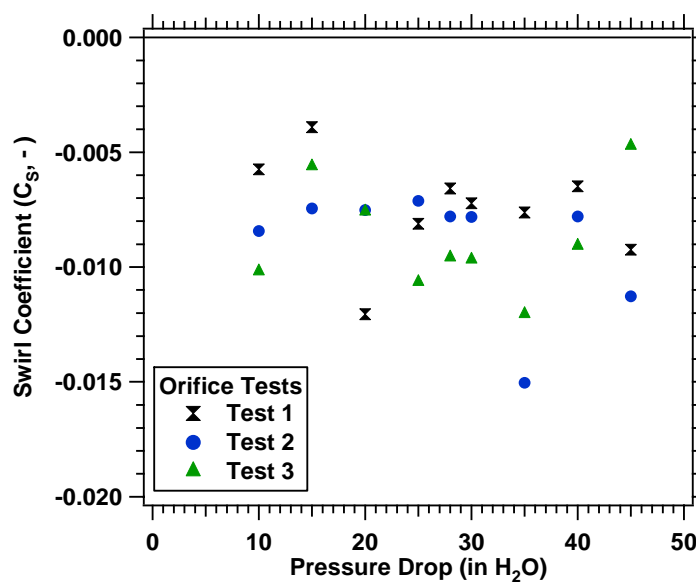


Figure 4.4.2: Orifice Plate Swirl Coefficient Response over Varying ΔP

Whereas the test on the head provided a convergence of C_s at high ΔP , the orifice plate did not seem to reduce in variability with higher ΔP . The absolute torque (see Fig. 4.4.3) was found to increase with ΔP , and hence the mass flow rate.

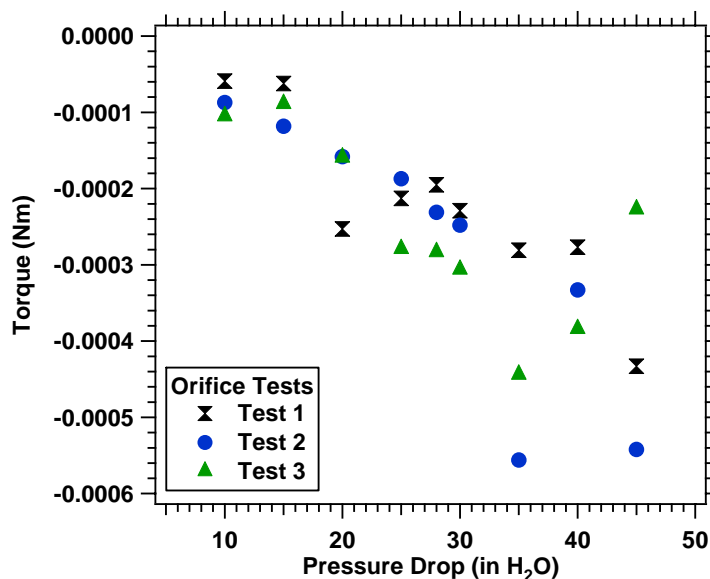


Figure 4.4.3: Orifice Plate Torque Response with Varying ΔP

Investigating these data on a time basis, large transients can be found at the higher ΔP (see Fig. 4.4.4).

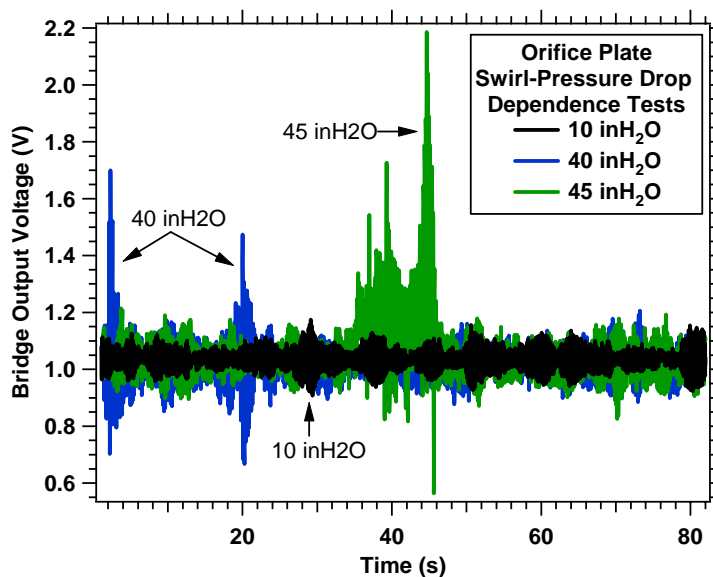


Figure 4.4.4: Output Voltage Time Varying Response with ΔP

These transients were found to bias the time-averaged voltage for high ΔP datasets as they could last a significant portion of the acquisition time leading to the variance in Fig. 4.4.4.

These transients were also associated with an audible change in the blower motor. The data

quality was found to be dependent on the sampling frequency. Sampling at 100Hz for approximately 60 seconds provided consistent, repeatable data and was short enough to allow for a full valve lift to be recorded without overheating the flow bench.

The minimal change in C_S across all ΔP in Fig. 4.4.2 provided significant confidence in the swirl data.

The discharge coefficient was found to increase with change in pressure which was expected due to the increase in mass flow (see Fig. 4.4.5).

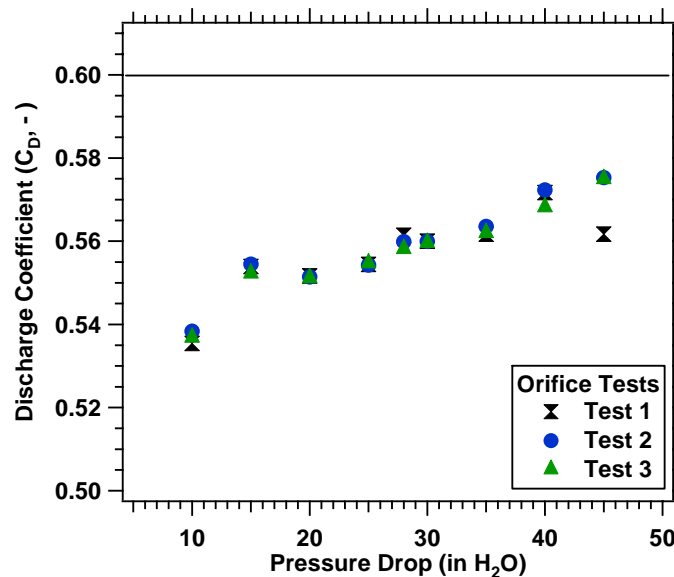


Figure 4.4.5: Orifice Plate Torque Response with Varying ΔP

The slight deviation from the theoretical $C_D \sim 0.6$ can be attributed to the viscous effects as the plate thickness was on the same order as the orifice diameter. Although slightly off from the theoretical value, again this provided significant confidence that the flow parameters are correctly measured and calculated.

4.5 Statistical Analysis of Uncertainty and Repeatability

Due to the minimal flow rates provided by small engine heads, care must be taken to accurately measure the momentum flux. Following the analysis developed by Bottom, the uncertainty for various valve lifts can be determined [4]. Four valve lifts (25, 50, 75, 100% of max lift) were selected to represent the lift profile. Fifteen data sets of the four valve lifts were collected at 40 inH₂O and randomized. The repeatability and uncertainty of the volumetric flow rate (Q), flow coefficient (C_F) and swirl coefficient (C_S) will be explored.

4.5.1 Volumetric Flow Rate

The volumetric flow rate, Q , is determined directly from the pressure drop, percent flow and orifice plate calibration from the flowbench. This value is used to calculate the mass flow rate and the rest of the non-dimensional parameters, therefore the uncertainty of Q is of particular interest. From Fig. 4.5.1, it is obvious that repeatability is quite good.

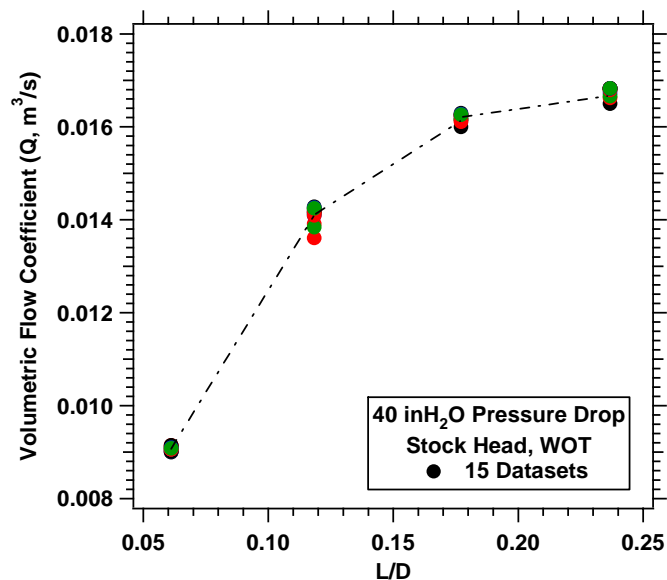


Figure 4.5.1: Repeatability from 15 Randomized Tests of the Volumetric Flow Rate

From Bottom [4], the uncertainty is determined by

$$u_Q = \pm t_{v,p} S_Q \quad \text{Eqn. 4.5.1}$$

Where t is a t-estimator value of 95% probability ($t = 1.761$, [65]) and S_Q is the standard deviation of the Q values. The calculated uncertainty for WOT and partial throttle tests are presented in Table 4.5.1 and Fig. 4.5.2.

Table 4.5.1: Uncertainty of Volumetric Flow Rate for WOT and Partial Throttle Tests Based off of Full Scale Mean Q Respectively

| Lift [L/D] | u_Q WOT [%FS] | u_Q Partial Throttle [%FS] |
|------------|-----------------|------------------------------|
| 0.06 | 1.23 | 0.315 |
| 0.12 | 1.28 | 0.216 |
| 0.18 | 2.06 | 0.212 |
| 0.24 | 1.13 | 0.157 |

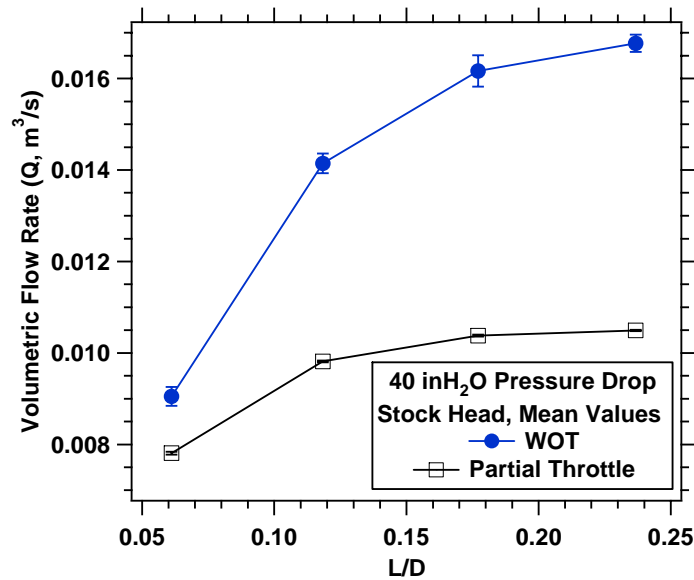


Figure 4.5.2: Mean Values of Volumetric Flow Rate with Uncertainty Error Bars

Both WOT and partial throttle uncertainty is at least an order of magnitude lower than measured values, and decreases with higher valve lifts.

4.5.2 Flow Coefficient

The flow coefficient, C_F , uncertainty is similar to the volumetric flow rate analysis using a 95% probability.

$$u_{CF} = \pm t_{v,p} S_{CF} \quad \text{Eqn. 4.5.2}$$

Again the repeatability is quite good between all tested datasets (see Fig. 4.5.3).

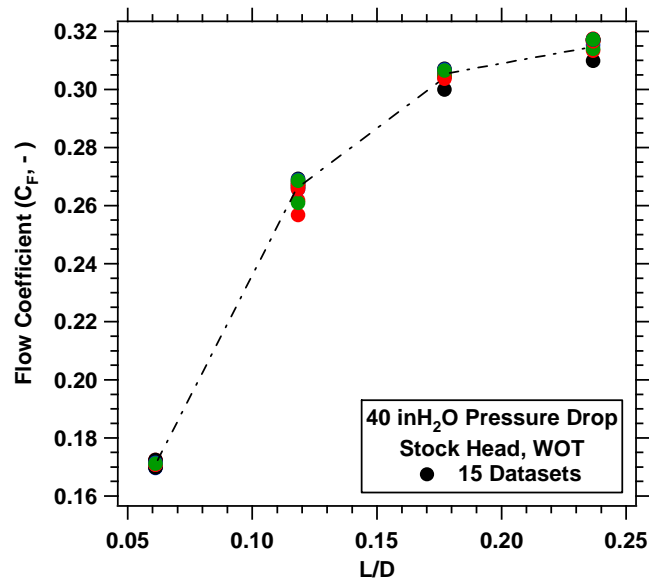


Figure 4.5.3: Repeatability from 15 Randomized Tests of the Flow Coefficient

The uncertainty is listed in Table 4.5.2 and Fig. 4.5.4.

Table 4.5.2: Uncertainty of Flow Coefficient for WOT and Partial Throttle Tests Based off of Full Scale Mean C_F Respectively

| Lift [L/D] | u_{CF} WOT [%FS] | u_{CF} Partial Throttle [%FS] |
|------------|--------------------|---------------------------------|
| 0.06 | 1.23 | 0.315 |
| 0.12 | 1.28 | 0.213 |
| 0.18 | 2.06 | 0.209 |
| 0.24 | 1.14 | 0.157 |

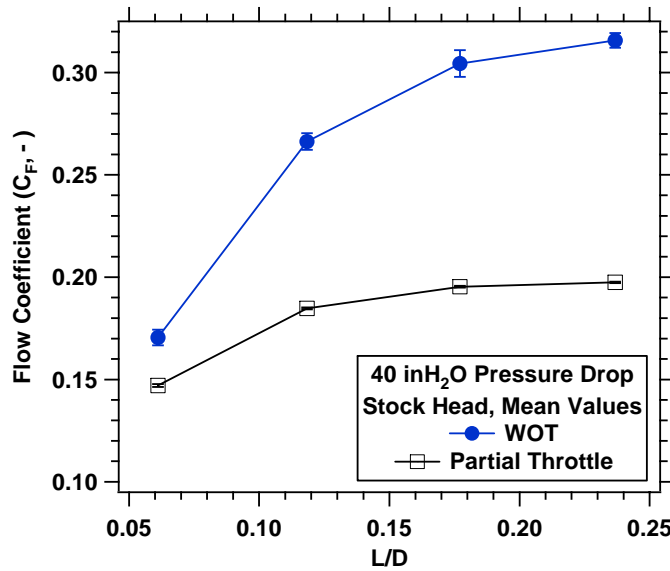


Figure 4.5.4: Mean Values of Flow Coefficient with Uncertainty Error Bars

As with Q , with an increase in valve lift, uncertainty improves. The uncertainty for all valve lifts is at least two orders of magnitude below measured values.

4.5.3 Swirl Coefficient

The swirl coefficient, C_S , is a function of various flow parameters and the measured torque output from the swirl adaptor:

$$C_S = f(\Delta P_{Head}, \rho_{mixture}, Q, TQ) \quad Eqn. 4.5.3$$

There is poor repeatability of the swirl coefficient at low lifts, but it improves significantly with increased valve lift. The repeatability of the swirl coefficient is not as good as previous parameters, but significantly improves with increased valve lift (see Fig. 4.5.5).

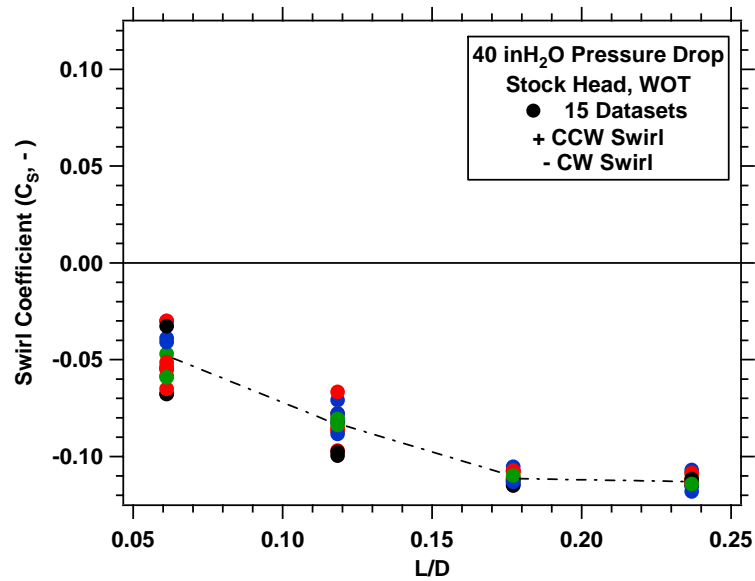


Figure 4.5.5: Repeatability from 15 Randomized Tests of the Swirl Coefficient

The poor repeatability at the low valve lifts can be attributed to low flow rates at the low values as well as minor flow variations through the bench (see section 4.4 and Fig. 4.4.4).

Examining three full valve sweep tests, it is evident a minimum valve lift is required before the data converge (see Fig. 4.5.6).

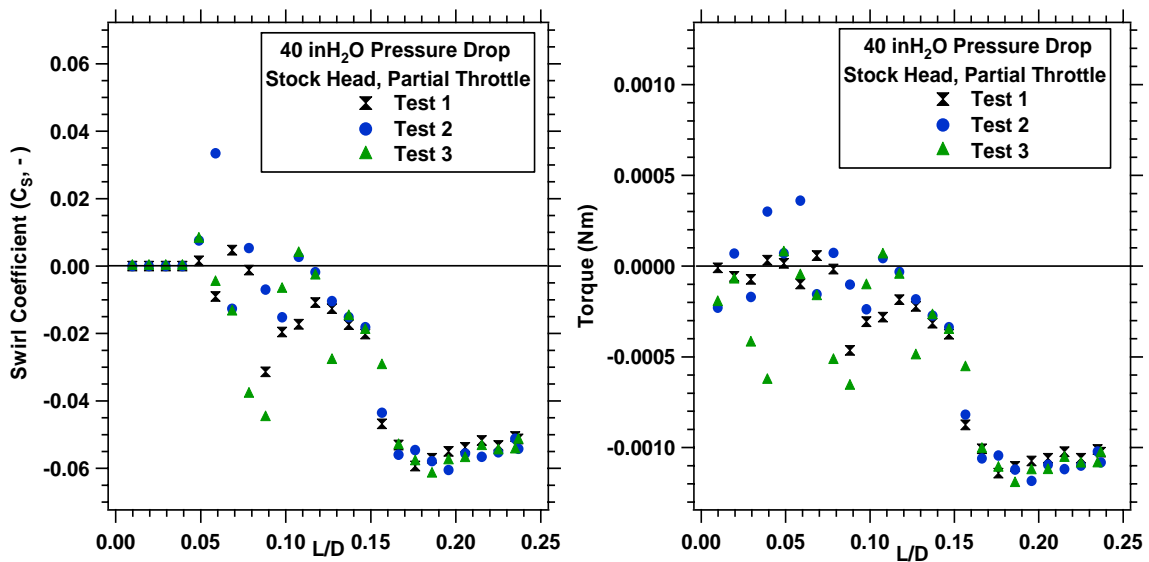


Figure 4.5.6: Swirl Coefficient and Torque Data Indicating Noise at Low Valve Lifts

Note the swirl data below $L/D = 0.05$ is artificially set to zero due to numerical errors induced by the very small flow rates and is similar to the method conducted by Briggs [63].

The uncertainty equation for swirl coefficient is modified from the form of equation 4.5.1 to reflect sensitivity of each parameter on the coefficient:

$$u_{C_s} = \sqrt{(\theta_{\Delta P} u_{\Delta P})^2 + (\theta_{\rho} u_{\rho})^2 + (\theta_Q u_Q)^2 + (\theta_{TQ} u_{TQ})^2} \quad \text{Eqn. 4.5.4}$$

Where θ is a weighting parameter for each variable (see [4] for further definition). Both WOT and partial throttle data indicated considerable uncertainty across all valve lifts (see Table 4.5.3 and Fig. 4.5.7).

Table 4.5.3: Uncertainty of Flow Coefficient for WOT and Partial Throttle Tests Based off of Full Scale Mean C_s Respectively

| Lift [L/D] | u_{C_s} WOT [%FS] | u_{C_s} WOT [-] | u_{C_s} Partial Throttle [%FS] | u_{C_s} Partial Throttle [-] |
|------------|---------------------|-------------------|----------------------------------|--------------------------------|
| 0.06 | 195 | 0.170 | 949.7 | 0.197 |
| 0.12 | 124.8 | 0.109 | 755.6 | 0.157 |
| 0.18 | 109.2 | 0.095 | 714.6 | 0.149 |
| 0.24 | 105.3 | 0.092 | 706.9 | 0.147 |

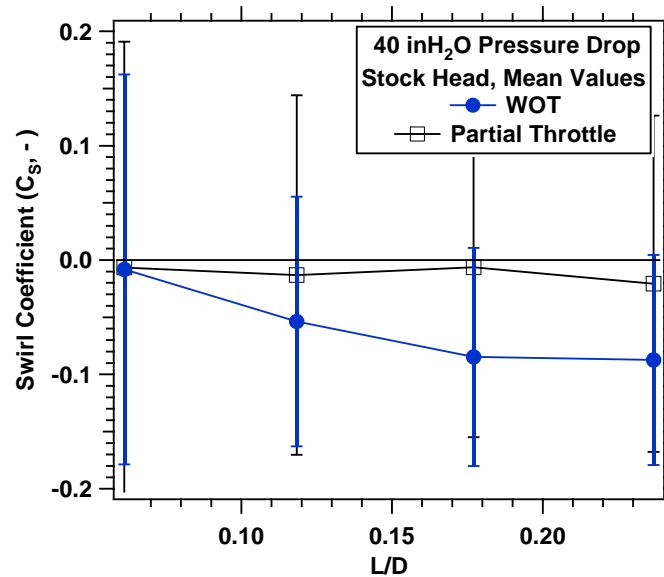


Figure 4.5.7: Mean Values of Swirl Coefficient with Uncertainty Error Bars

The large uncertainty, on the order of the measurement value, is primarily due to the uncertainty associated with the torque value. Although the uncertainty for the swirl measurement is surprisingly large, there is considerable confidence in the data because of the highly repeatable values at the high valve lifts (see Fig. 4.5.6).

4.6 Throttle Effects on Steady Flow Tests

This engine is equipped with a carburetor located at the entrance of the head. As one would expect, throttling the system by the carburetor results in a significant change in the mass flow rate and flow coefficient (see Fig. 4.6.1).

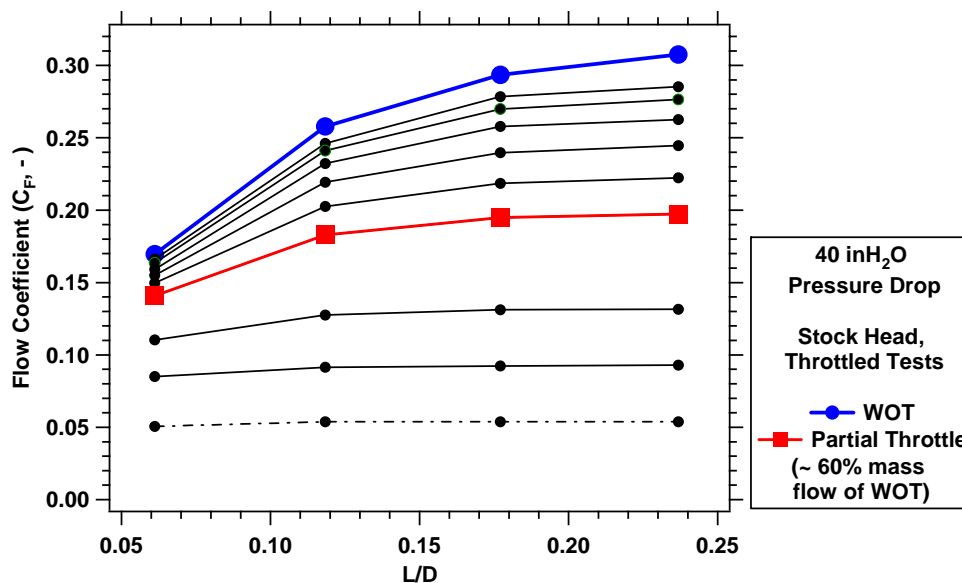


Figure 4.6.1: Effect of the Throttle Setting on the Flow Coefficient

The throttle dominates the system as the flow response decreases to a near flat line. As the throttle is reduced from WOT, the flow rate flattens out because the throttle plate is creating the minimum flow area rather the port and valve system. The goal of the partial throttle tests were to match the mass flow rate of the 25% load condition of the combustion tests and determine if the throttle plate at a given angle emphasizes a specific flow direction. The

calculated mass flow rate of the combustion tests fell below the flat line response indicated in Fig. 4.6.1 (dashed line) therefore the curve marked with large squares rate was selected for “partial throttle” testing. This flow rate provided sufficient response over the valve lift and represented 60% mass flow of the WOT condition.

The swirl coefficient changes significantly (see Fig. 4.6.2) from 0.1 at full lift to near zero with partial throttle conditions.

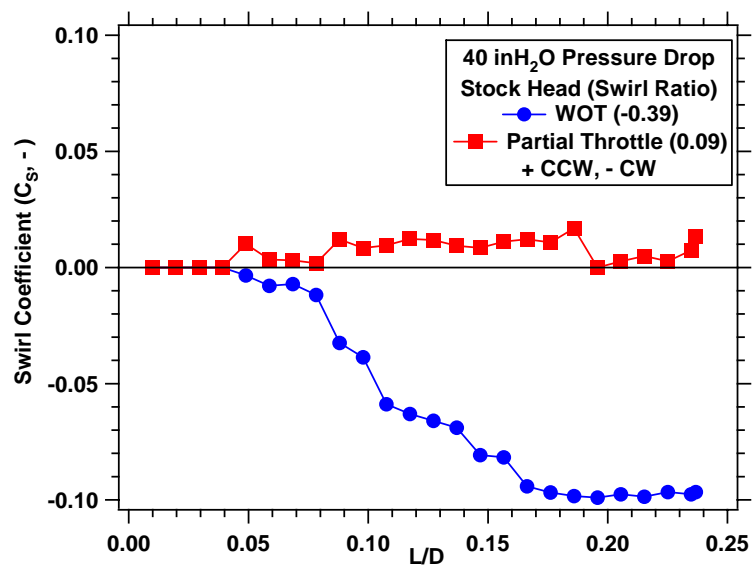


Figure 4.6.2: Swirl Coefficient Response with Partial Throttle Conditions

The trend as indicated in Fig 4.6.2 and the lower global swirl ratio for the partial throttle case follows the hypothesis of poor bulk motion at light-load conditions. This also indicates the throttle plate significantly affects the flow field (see Fig. 4.6.3).

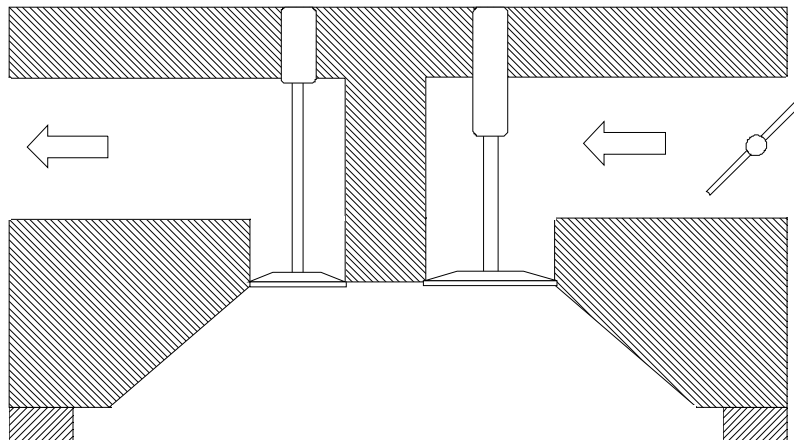


Figure 4.6.3: Diagram of the Throttle Plate Relative to the Combustion Chamber

The throttle plate arrangement is positioned to favor a tumbling motion, or a vortex axis perpendicular to the cylinder axis, rather than a swirling motion.

4.7 Modified Combustion Chamber Steady Flow Tests

To further understand the impact of the combustion chamber geometry and throttle under WOT and partial throttle conditions, the bathtub combustion chamber was machined out of the valve area resulting in a flat, pancake combustion chamber profile (see Fig. 4.7.1 in comparison to Fig. 4.17 for the stock chamber geometry).

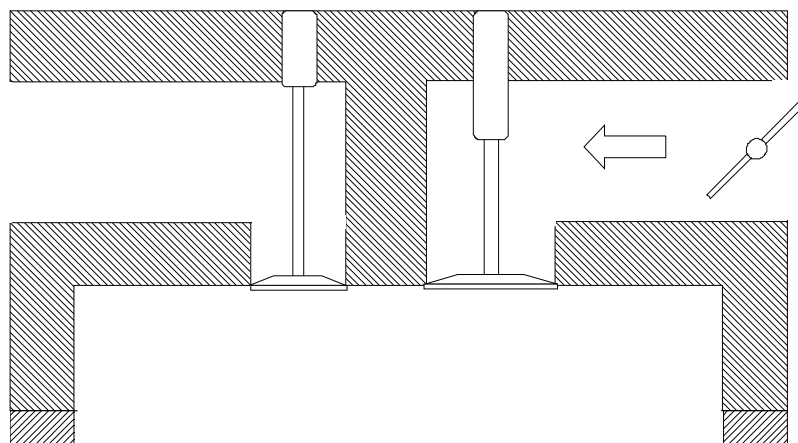


Figure 4.7.1: Modified Combustion Chamber; 'Decked' Geometry

From section 2.8.2 and 2.8.3 it was indicated the combustion chamber shape and port angle can affect the flow field; this modified head provides a method to directly determine the effect of the bathtub shape on the flow field momentum.

Bottom indicated the direction of the intake port can enhance the flow field independent of the combustion chamber shape [4]. The advantageous direction of the Briggs port should favor a CCW flow direction (see Fig. 4.7.2).

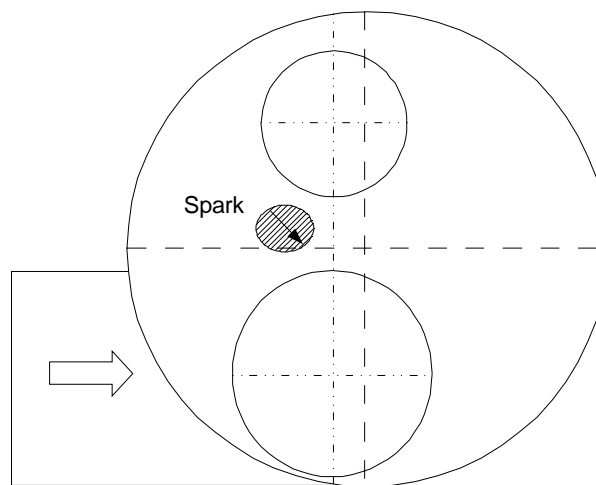


Figure 4.7.2: Port Configuration for “Natural” CCW Flow Momentum

At WOT, the decked head reduced the magnitude of the CW flow, but surprisingly, does not completely reduce this flow direction (see Fig. 4.7.3).

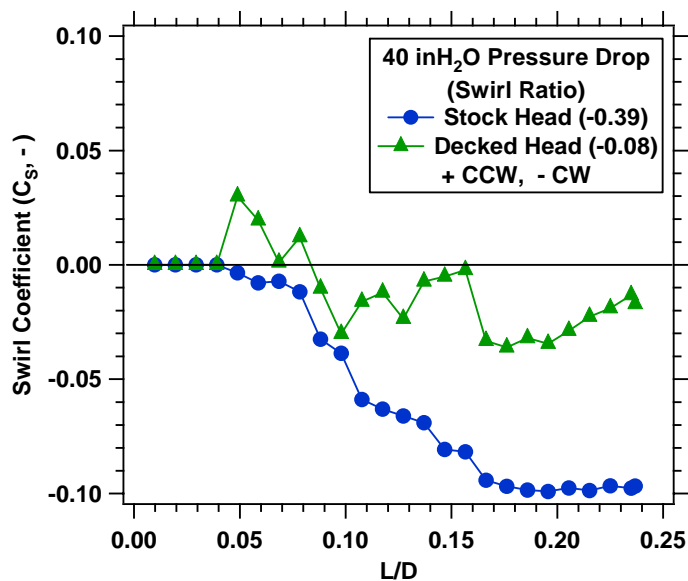


Figure 4.7.3: Swirl Coefficient Response to WOT “Decked” Combustion Chamber

The higher valve lifts ($L/D > 0.20$) indicate an upward trend towards a CCW flow as would be expected from this port configuration.

The influence of the port direction is only felt when the throttle is significantly affecting the system as shown in figure 4.7.4 for partial throttle conditions.

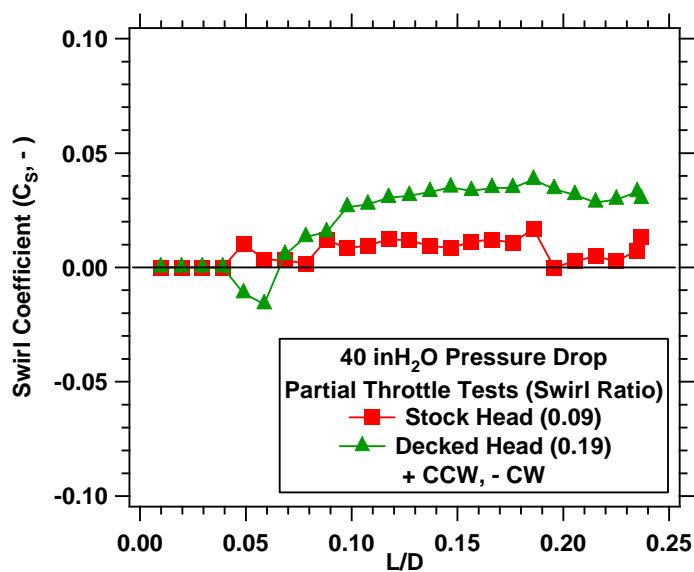


Figure 4.7.4: Swirl Coefficient Response to Partial Throttle “Decked” Combustion Chamber

There is a definite trend favoring CCW flow rather than the CW flow as indicated in Fig. 4.7.3 under WOT conditions. From this information, the partial throttle conditions allow for the favorable port position to be utilized.

As stated earlier, when the throttle is at a small angle, the mass flow rate is reduced and the flow coefficient shows little response with valve lift due to the minimum area created by the throttle, rather than the port/valve combination. Any flow modification at the valve face represents a boundary condition for the flow momentum into the combustion chamber. The near independence on the port direction on the flow then suggest the pressure losses in the port due to the sharp corner are significant enough to reduce the CCW flow to a quiescent charge. As the throttle angle is increased, the minimum area shifts and there are “distributed” pressure losses. This reduction in pressure losses at the valve face may allow for greater influence of the port direction. The influence of the throttle plate on directing the flow must be considered as well.

The mass flow rate did not change, as indicated by the flow coefficient (see Fig. 4.7.5) when the head was machined.

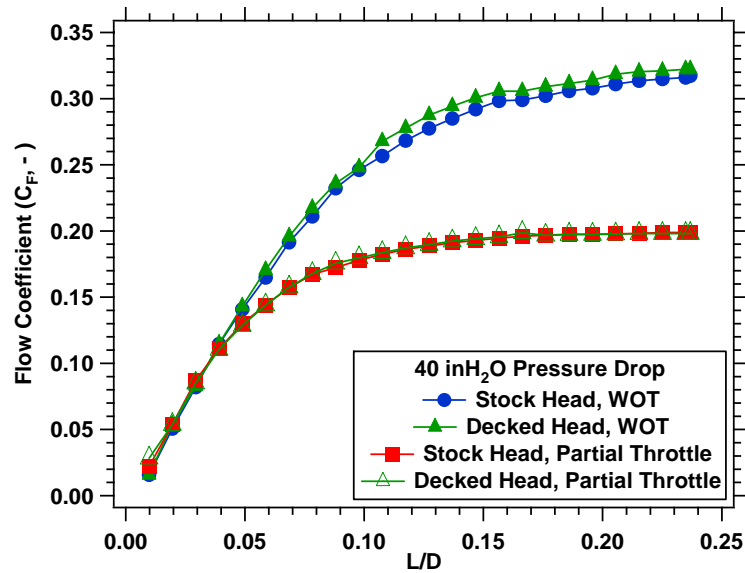


Figure 4.7.5: Flow Coefficient Response for the Decked Chamber Geometry

The minimal change in the flow coefficient indicates the various swirl responses is not due to a change in the mass flow rate.

4.8 Flow Modification

The flow modification was approached from two avenues; port and valve modifications. The port modifications consisted of large blockages placed far upstream of the valve face in the port/intake runner, or at the carburetor and head interface. The valve modifications consisted of blockages on the valve face or attachments on the valve stem. For brevity, only partial throttle data will be shown; WOT response plots are given in Appendix A.3.

4.8.1 Port Modifications

Blockages of the flow in simple port geometry, such as those common on small engines, will generate higher momentum but with a loss in flow rates due to the higher pressure losses.

4.8.1.1 Port Plates

Two “port plates” were created to direct the flow to favor one side of the port for either CCW and CW flow (see Fig.4.8.1).

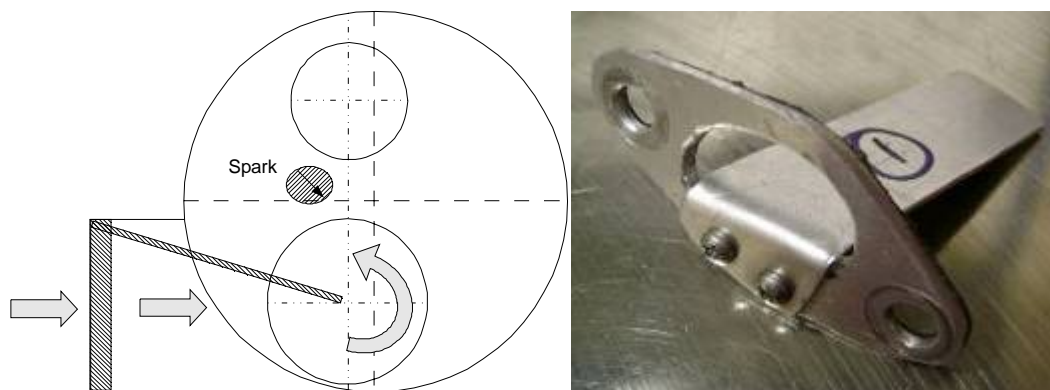


Figure 4.8.1: CCW Port Plate Design and Position in the Head

The port area decreased by 50% and the flow coefficient decreased (see Fig. 4.8.2), but the swirl coefficient and global swirl ratio dramatically increased (see Fig. 4.8.3).

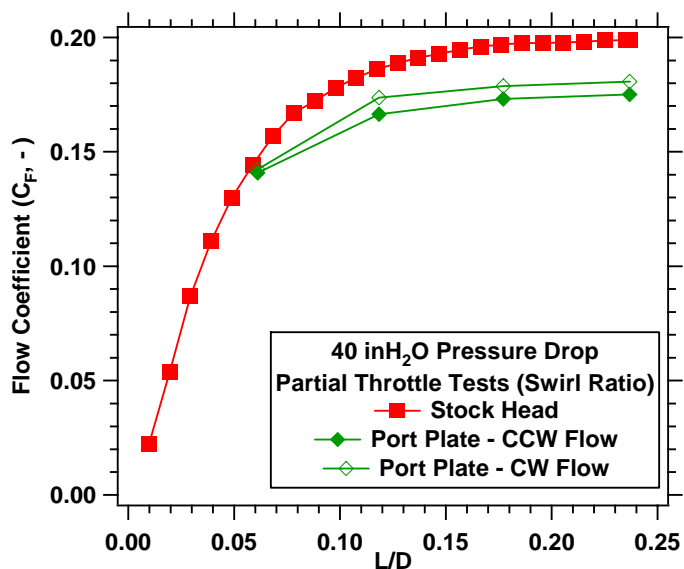


Figure 4.8.2: Partial Throttle Flow Coefficient Response Due to Port Plates Favoring CCW and CW Flow Direction

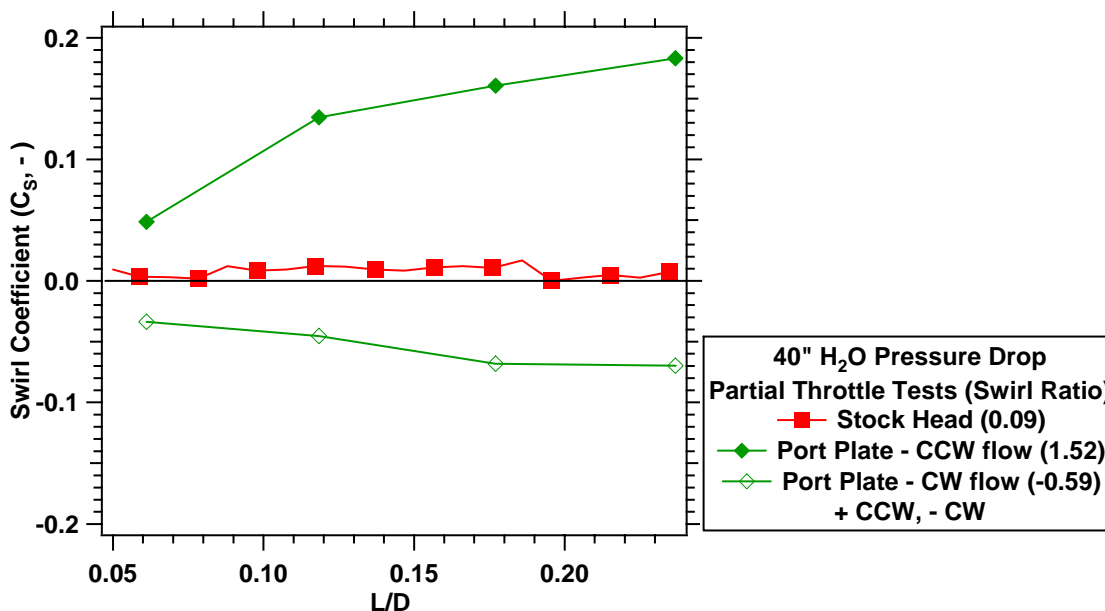


Figure 4.8.3: Partial Throttle Swirl Response Due to Port Plates Favoring CCW and CW Flow Direction

4.8.1.2 Charge Motion Control Valve

Automotive engines often employ a “charge motion control valve” (CMCV) during cold start transients to direct the flow towards one side of the port and acts as a second throttling area reducing the port area 50-75% [31]. During normal operation, the CMCV opens providing the full flow area. This technique was adapted for a small engine; creating a blockage at the interface of the carburetor and head (see Fig. 4.8.4).

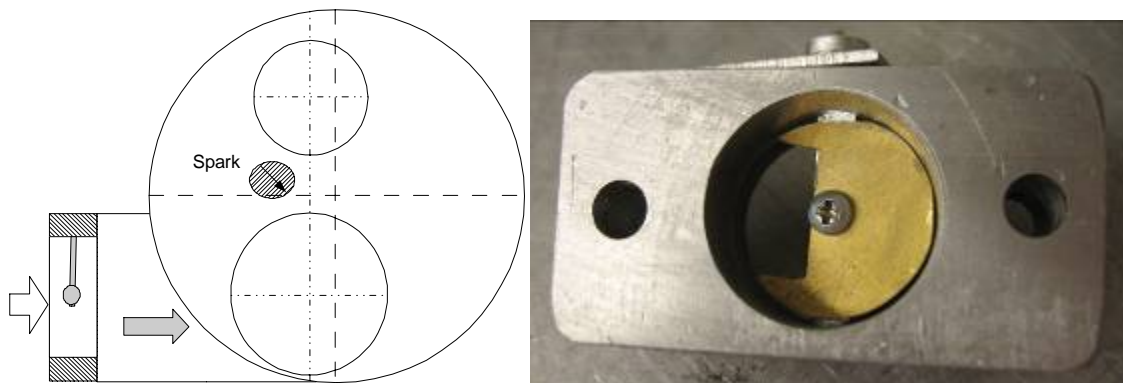


Figure 4.8.4: CMCV Design and Position in the Head

Various designs were investigated with 50% and 75% blockage; designs with the best swirl responses are shown in figure 4.8.5.

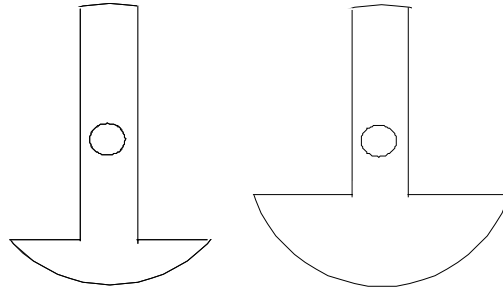


Figure 4.8.5: CMCV Plate Designs for 50% and 75% Port Area Blockage

The CMCV plates offer a blockage and mass flow rate change as expected (see Fig. 4.8.6).

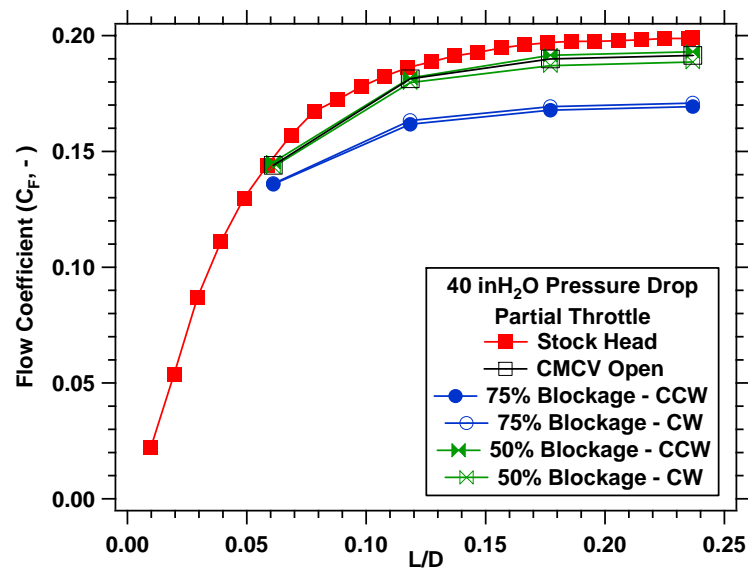


Figure 4.8.6: Partial Throttle Flow Coefficient Response Due to Various CMCV Plate Blockages

The 75% blockage plates significantly improve the swirl coefficient in comparison to 50% blockage plates (see Fig. 4.8.7).

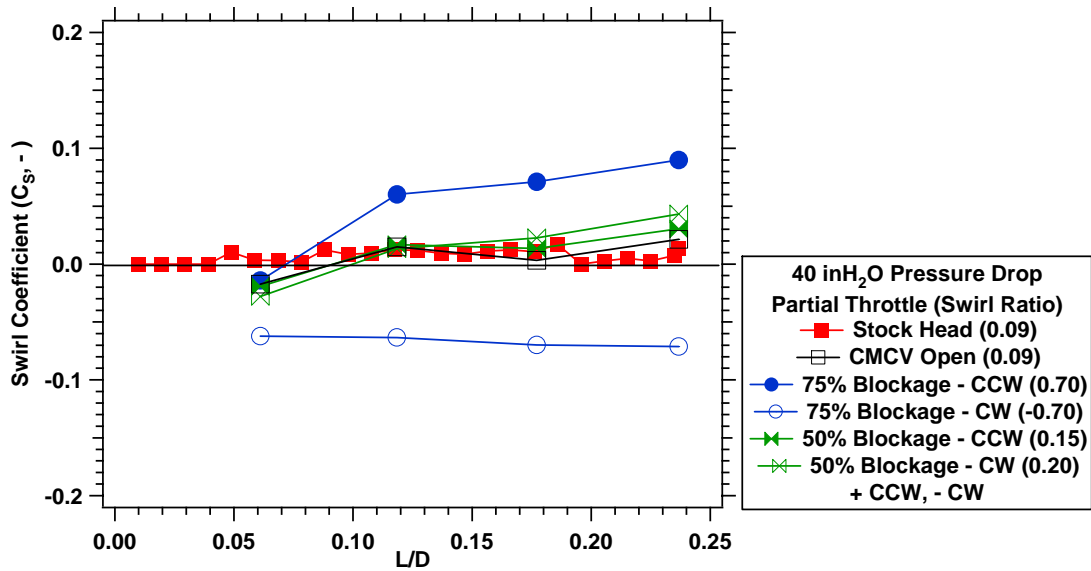


Figure 4.8.7: Partial Throttle Swirl Response Due to Various CMCV Plate Blockages

4.8.2 Valve Modifications

Valve geometry modifications are not commonly used outside of research engines due to increased valve dynamics, leading to more complex valve trains, and the fact that valve tends to rotate during operation [34]. Since the valve face and exit area act as the boundary condition for the intake jet, it is a favorable area for in-cylinder flow modification. Shrouded valves, “pin-wheel” valve stem attachments, and blockages are investigated in this section.

4.8.2.1 Shrouded Valves

A shrouded valve was created to provide directed flow at the valve face along 180 deg. of the valve diameter (see Fig. 4.8.8)

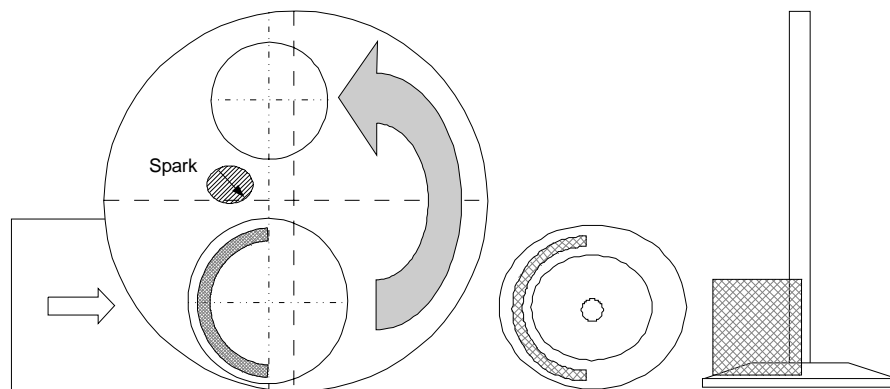


Figure 4.8.8: Shrouded Valve Design and Position in the Head

The shroud height (~6mm) allowed for the shroud to stay within the port during maximum lift, but not block the intake runner during low lift. The minimum “footprint” of the shroud allows for higher flow rates (see Fig. 4.8.9) while providing a significantly improved swirling flow field (see Fig. 4.8.10).

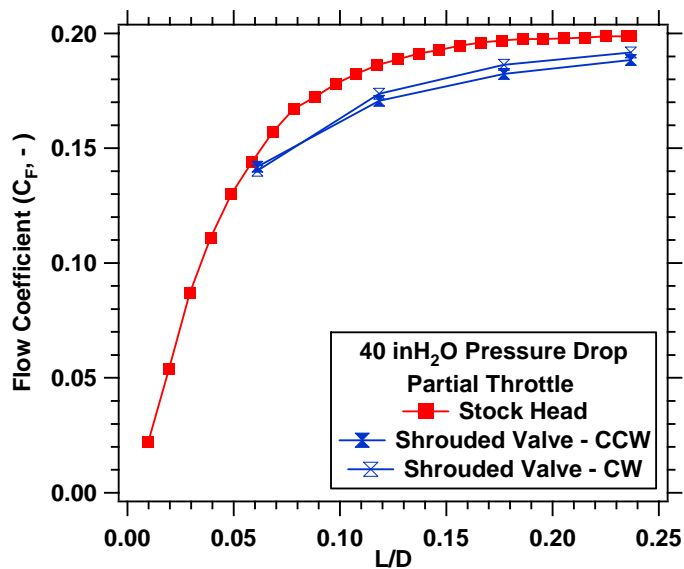


Figure 4.8.9: Partial Throttle Flow Coefficient Response Due to the Shrouded Valve

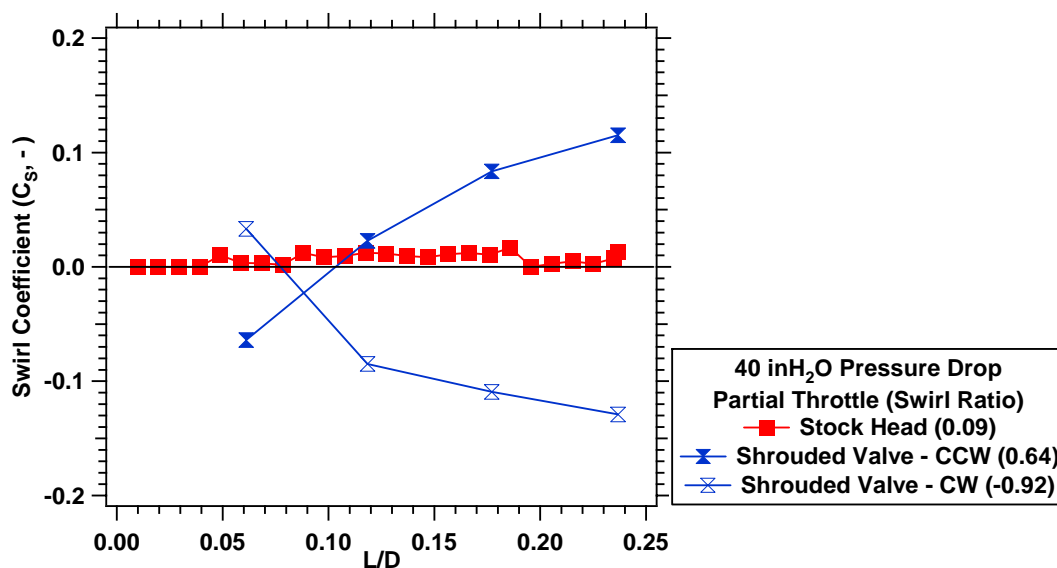


Figure 4.8.10: Partial Throttle Swirl Response Due to the Shrouded Valve

4.8.2.2 “Pin-Wheel” Blockage Valves

A “pin-wheel” blockage was created to fit over the valve face to provide directional vanes at the valve face. The number of vanes and vane direction were varied, but a constant angle-of-attack (AOA) to the incoming air-stream (see Fig. 4.8.11) was maintained.



Figure 4.8.11: Pin-wheel Blockage Design and Position on the Valve

The pin-wheel blockage height (~6mm) allowed for the top of the pin-wheel to stay within the port at max valve lift, but not interfere with intake runner air flow during low lift. The

significant blockage reduced the flow rates (see Fig. 4.8.12), but provided a significantly a higher swirl coefficient, specifically with the 4-vane blockage (see Fig. 4.8.13).

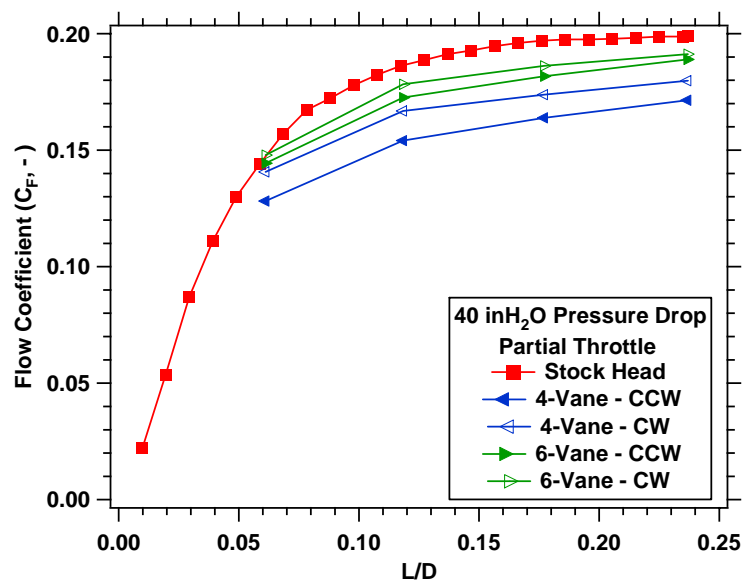


Figure 4.8.12: Partial Throttle Flow Coefficient Response Due to the Pin-Wheel Blockages at the Valve Face

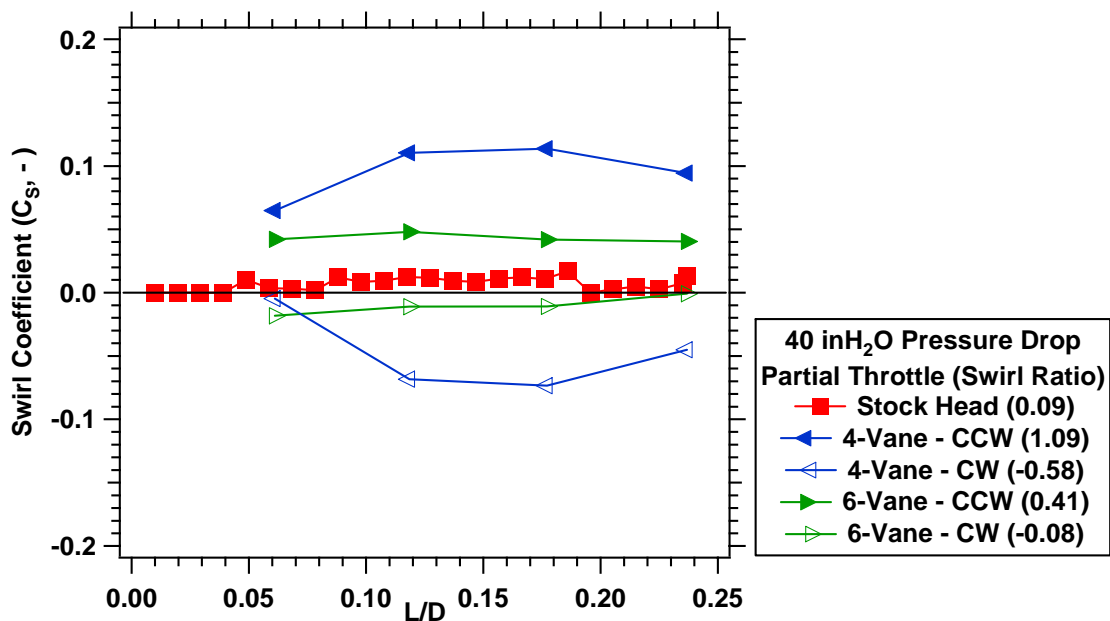


Figure 4.8.13: Partial Throttle Swirl Response Due to the Pin-Wheel Blockages at the Valve Face

4.8.2.3 “Pin-Wheel” Blockage on the Valve Stem

The pin-wheel blockages were reattached to the valve further up the stem to allow the blockage to be completely enclosed in the port for all valve lifts, forcing the entire port air flow through the blockage. At high lift, the bottom of the blockage would be in line with the port exit; at low lift, the blockage would significantly obstruct the intake runner flow (see Fig. 4.8.14).

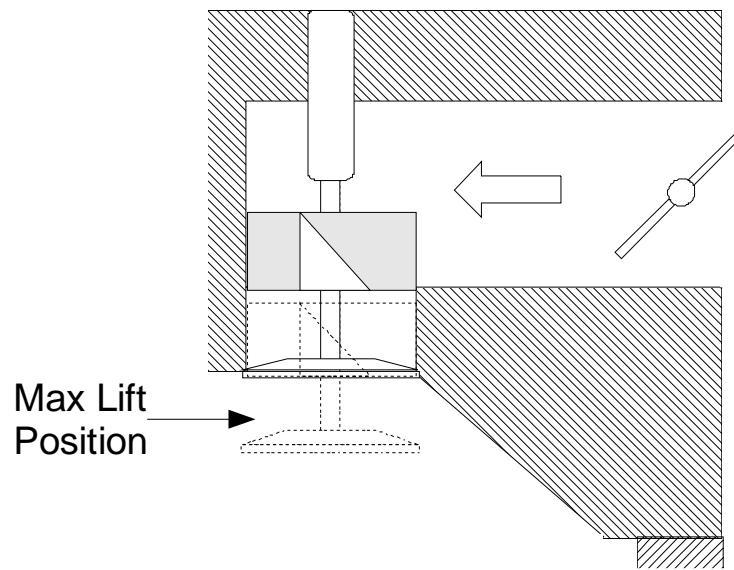


Figure 4.8.14: Pin-Wheel Blockage Position in the Head Attached to the Stem

Lower flow rates are seen with the pin wheel blockages (see Fig. 4.8.15), but they do result in higher swirl ratios (see Fig. 4.8.16).

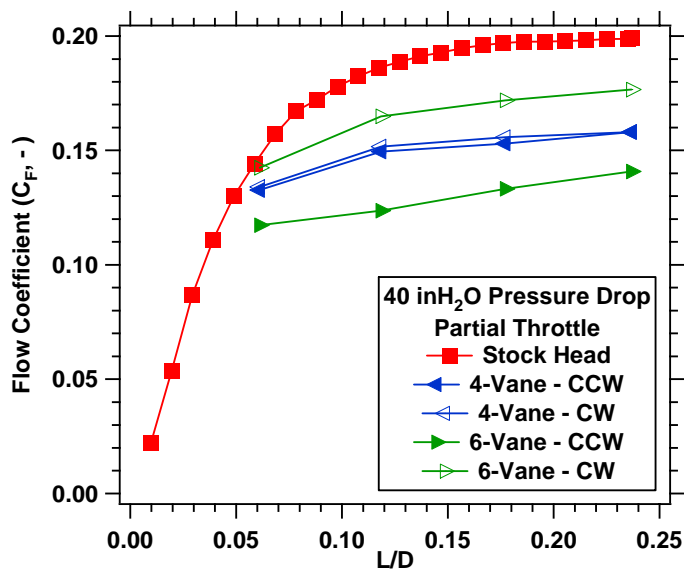


Figure 4.8.15: Partial Throttle Flow Coefficient Response Due to the Pin-Wheel Blockages Attached to the Valve Stem

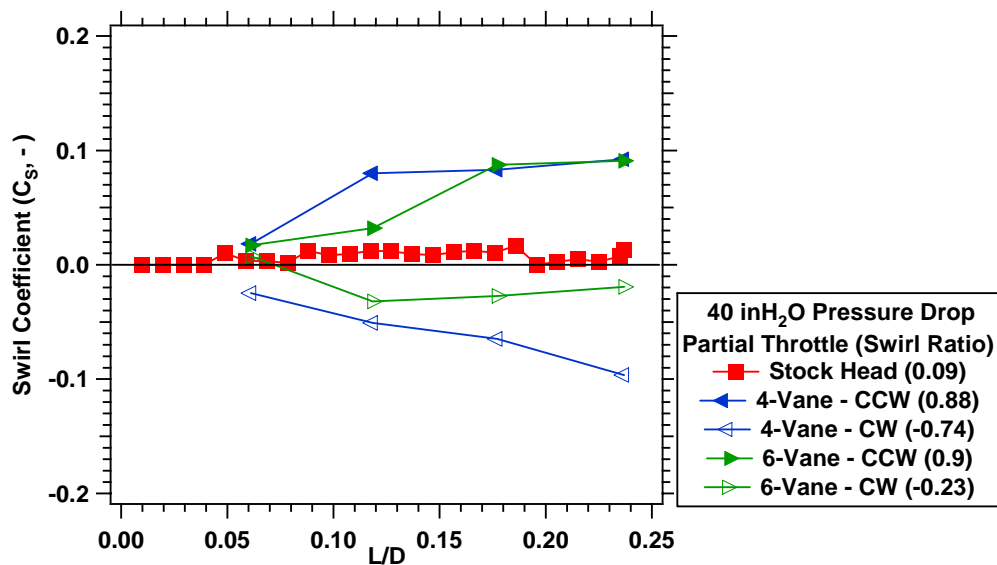


Figure 4.8.16: Partial Throttle Swirl Response Due to the Pin-Wheel Blockages Attached to the Valve Stem

The stem attachments provided slightly lower global swirl ratios than the attachments at the valve face, but the response curves are quite different. Whereas the stem attachments provide a continual increase of the swirl coefficient towards max lift, the face attachments provide a flat profile, modifying the flow equally across the valve lift.

4.8.2.4 Port Blockages

In order to determine if the flow was influenced more from the directional vanes or as a result of blockages, an aluminum plug was created to block the port area to force all of the flow through half of the valve. The blockage filled the space between the top of the port to the valve face, and firmly attached to the head (see Fig 4.8.17).

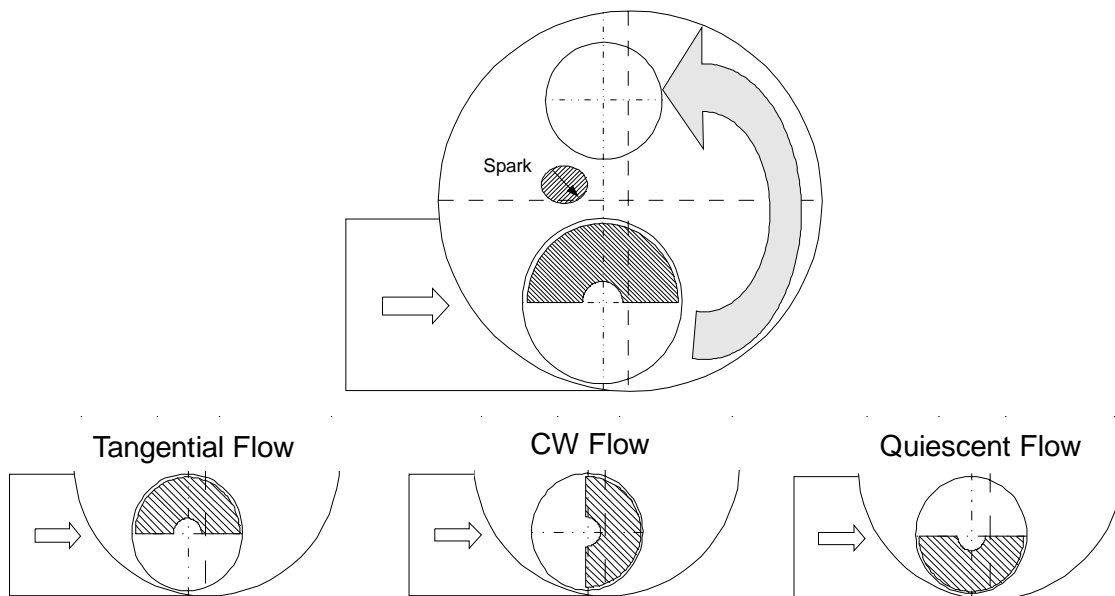


Figure 4.8.17: Tangential Blockage Position in the Head

With a significant portion of the port blocked with the aluminum blockage, the flow coefficient drops slightly (see Fig. 4.8.18). The blockage, however, produced a significantly higher swirl coefficient when oriented in the tangential flow position in Fig. 4.8.17 (see Fig. 4.8.19).

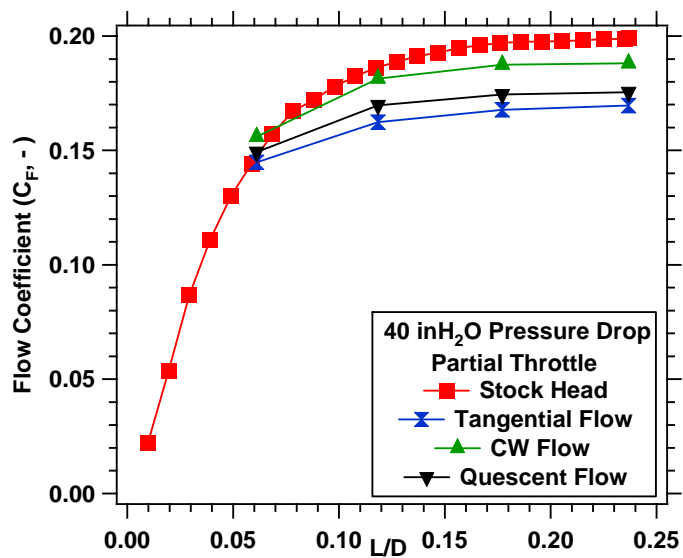


Figure 4.8.18: Partial Throttle Flow Coefficient Response Due to the Port Blockages

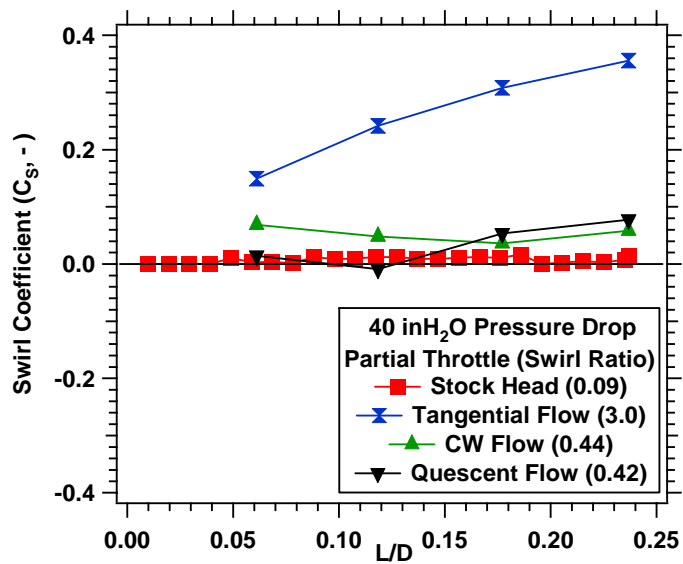


Figure 4.8.19: Partial Throttle Swirl Response Due to the Port Blockages

The tangential blockage provided for the highest global swirl ratio and was modified to allow for on engine combustion tests.

4.9 Steady Flow Conclusions

A steady flow analysis was performed on a stock Briggs & Stratton Intek head to determine a global perspective of the in-cylinder flow at WOT and partial throttle conditions. The flow and swirl coefficient provided insight into the flow rate and the momentum generated from various modifications to the valve, port and combustion chamber geometry. Although there is a large uncertainty associated with the swirl coefficient due to the low momentum produced by the flow field, high repeatability was achieved in the measurements.

Throttling the system with the carburetor to simulate a “light-load” condition significantly changed the swirl conditions in the head. At WOT conditions, the combustion chamber shape was found to produce a significantly different flow field than expected from the favorable CCW port arrangement. At partial throttle conditions the port geometry was found to impact the flow field to provide a weakly swirling flow in the direction of the port flow.

Flow modifications to the port, through port plates and the CMCV, provided a modest improvement in swirl coefficient due to the relatively long distance from the combustion chamber. Flow modification close to the valve face yielded higher swirl coefficients, but any changes to the valve significantly add to the valve dynamics and therefore are not favorable for on-engine experiments. Blockages provided higher swirling fields than directional vanes such as pin-wheel valve attachments or directional port plates. A blockage in the port to accentuate a tangential flow provided the highest swirl coefficient; a version of this modification was created for high-swirl combustion experiments (see Fig. 4.8.20 and Fig. 4.8.21).

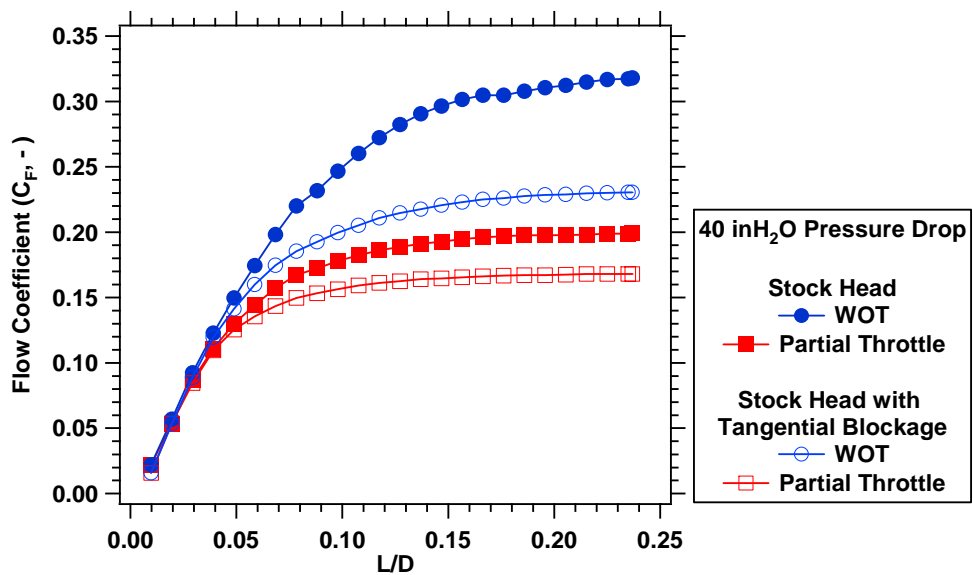


Figure 4.8.20: WOT and Partial Throttle Flow Coefficient Response Due to the Tangential Blockage Attached to the Head for Combustion Tests

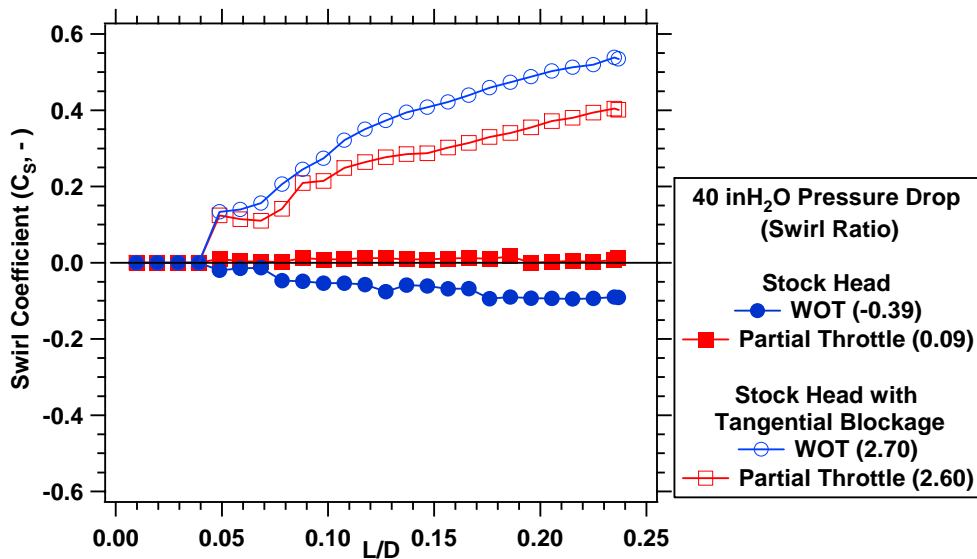


Figure 4.8.21: WOT and Partial Throttle Swirl Coefficient Response Due to the Tangential Blockages Attached to the Head for Combustion Tests

5.0 Engine Performance Characterization

5.1 Introduction

This chapter will present the experimental combustion data collected for common light-load, low-speed operating conditions. The load, speed and spark positions for each condition is presented in the test matrix (Table 5.1).

Table 5.1.1: Engine Test Matrix

| RPM | Load | AF Ratio | Spark Position |
|------------|-------------|-----------------|-----------------------|
| 1750 | 10 | 12 | Stock |
| | | | Alternate |
| | | | Dual Spark |
| 1750 | 25 | 12 | Stock |
| | | | Alternate |
| | | | Dual Spark |
| 3060 | 10 | 12 | Stock |
| | | | Alternate |
| | | | Dual Spark |
| 3060 | 25 | 12 | Stock |
| | | | Alternate |
| | | | Dual Spark |

The spark timing was swept to present combustion phasing both advanced and retarded from the stock spark timing. Cylinder pressure and emissions data were collected for each of the speed, load, spark position and spark timing conditions to determine heat release rate, combustion phasing, averaged emissions and engine performance.

5.2 Operating Condition Effects on Heat Release Rate

It is important to understand how operating conditions affect the heat release rate and burn duration. Burn duration, a parameter describing the length of heat release, is defined to be between 10 and 90% of the cumulative heat release. By understanding the influence of engine speed, load, spark timing and spark position on combustion performance, changes due to bulk fluid motion will be able to be isolated and analyzed.

5.2.1 Engine Speed Effects on Combustion Performance

For similar engine load, a minor change in the heat release rate due to engine speed on a crank angle basis is indicated in Fig. 5.2.1 and 5.2.2.

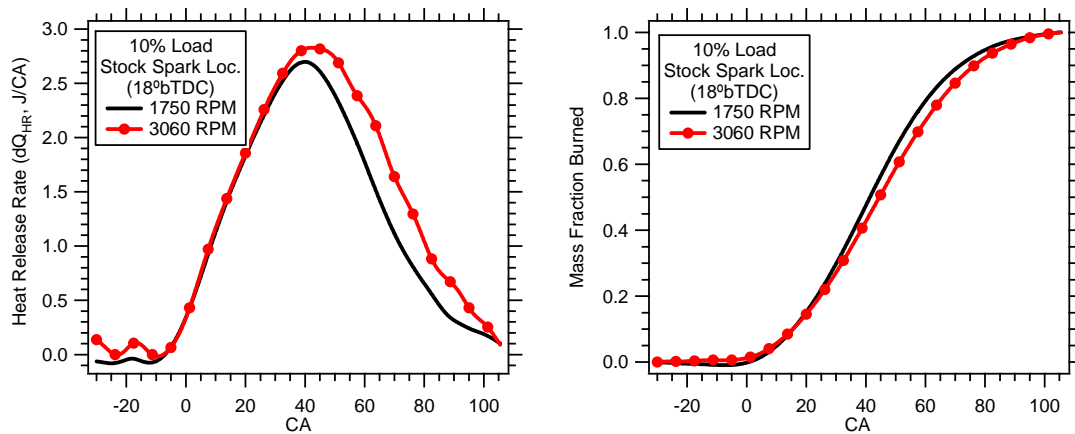


Figure 5.2.1: Variance of Heat Release at 10% Load

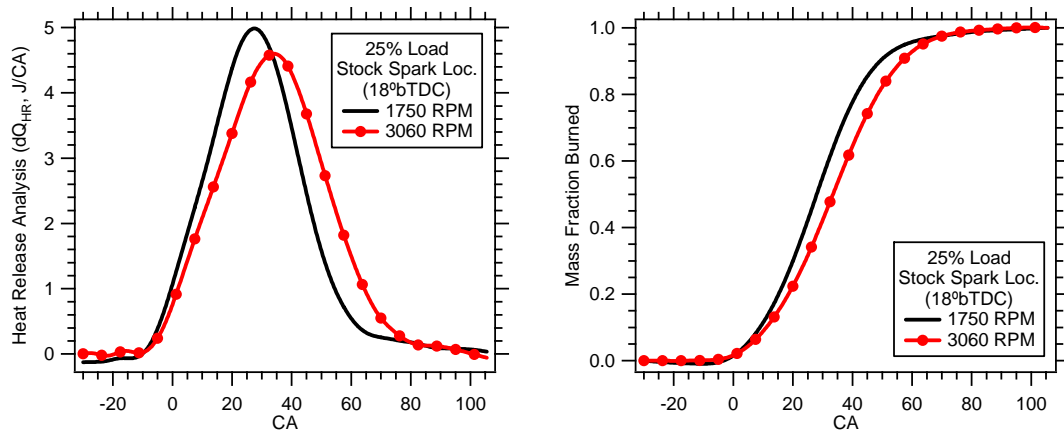


Figure 5.2.2: Variance of Heat Release at 25% Load

Previous studies [1, 13] have indicated a near independence of engine heat release rate with engine speed. It has been shown that a change of burn duration is indicated on a physical time basis, due to the change in turbulence intensity associated with engine speed, but little change is observed on a crank angle basis; a similar trend was indicated in these data. Tables 5.2.1 and 5.2.2 show the summary of data for the heat release traces shown above along with the calculated physical time of the burn duration.

Table 5.2.1: Combustion Performance Data for 10% Load Conditions

| Ign. Timing | Load | Speed | CA50 | CA10-90 | Time CA10-90 (ms) | COV |
|-------------|------|-------|------|---------|-------------------|-------|
| 18°bTDC | 10% | 1750 | 41 | 58 | 5.52 | 8.67% |
| | | 3060 | 43 | 63 | 3.43 | 9.80% |

Table 5.2.2: Combustion Performance Data for 25% Load Conditions

| Ign. Timing | Load | Speed | CA50 | CA10-90 | Time CA10-90 (ms) | COV |
|-------------|------|-------|------|---------|-------------------|-------|
| 18°bTDC | 25% | 1750 | 27 | 43 | 4.1 | 4.08% |
| | | 3060 | 33 | 47 | 2.56 | 4.74% |

From this analysis, there is a slight advantage for the lower speed at both loads on a crank angle basis. This trend was common for both single spark locations (stock and alternate locations) but was even more pronounced in the dual spark configuration. Although the crank angle time is similar, the physical time indicates the impact of engine speed on heat release rate. As stated earlier, increasing the piston speed increases the turbulence intensity which in turn increases the burn rate on a physical time basis.

5.2.2 Load Effects on Combustion Performance

With a throttled engine, increasing the load is a result of an increase in throttle angle and a higher charge mass flow rate. Higher flow rates can assist with in-cylinder bulk motion creating a favorable combustion condition. Increasing the load also results in a higher volumetric efficiency and a more favorable combustion condition. Varying the load on the engine results in a significant change in the heat release rates as indicated in Figs. 5.2.3 and 5.2.4.

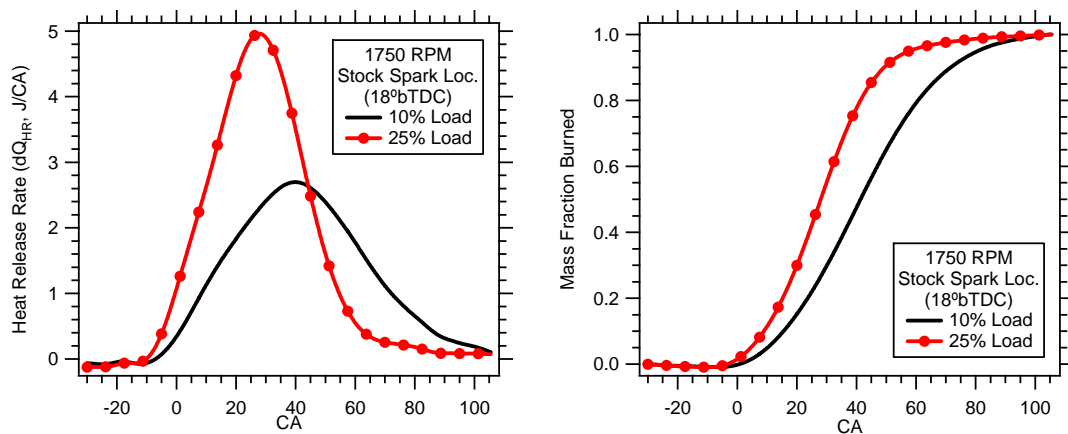


Figure 5.2.3: Variation of Heat Release at 1750 RPM

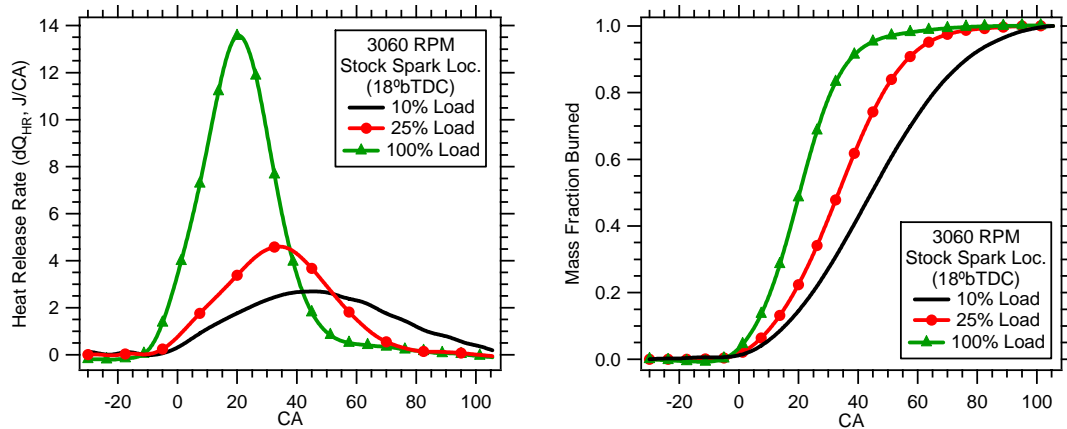


Figure 5.2.4 Variation of Heat Release at 3060 RPM

As indicated in the figures above, increasing the load advances the combustion phasing and decreases the burn duration. Tables 5.2.3 and 5.2.4 show a summary of the combustion data for the figures above.

Table 5.2.3: Combustion Performance Data for 1750 RPM Conditions

| Ign. Timing | Load | Speed | CA50 | CA10-90 | Time CA10-90 (ms) | COV |
|-------------|------|-------|------|---------|-------------------|-------|
| 18°bTDC | 10% | 1750 | 41 | 58 | 5.52 | 8.67% |
| | 25% | 1750 | 27 | 43 | 4.1 | 4.08% |

Table 5.2.4: Combustion Performance Data for 3060 RPM Conditions

| Ign. Timing | Load | Speed | CA50 | CA10-90 | Time CA10-90 (ms) | COV |
|-------------|------|-------|------|---------|-------------------|-------|
| 18°bTDC | 10% | 3060 | 43 | 63 | 3.43 | 9.80% |
| | 25% | 3060 | 33 | 47 | 2.56 | 4.74% |
| | 100% | 3060 | 20 | 33 | 1.8 | 1.45% |

This trend is consistent for both single spark locations, as well as the dual spark configuration.

5.2.3 Ignition Timing Effects on Combustion Performance

The primary effect of spark timing is to change the combustion phasing. Since the heat release reflects the combustion performance, there is a direct relationship between the spark timing and heat release phasing. With a spark timing around mean best torque (MBT), there is a reduction in the burn duration due to a favorable pressure situation balancing the positive and negative work on the piston. Retarding the spark timing, results in a retarded combustion phasing and an increase in burn duration. This effect is indicated in Fig. 5.2.5.

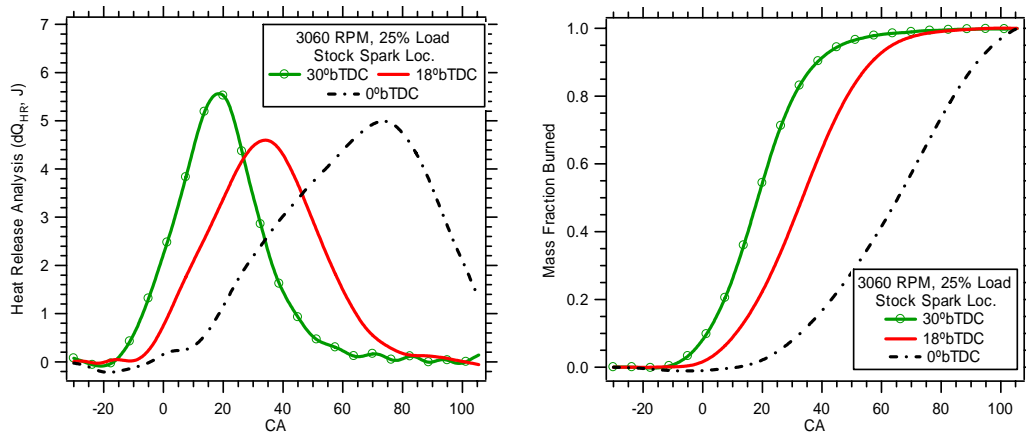


Figure 5.2.5: Variation of Heat Release with Spark Timing

The combustion performance data (refer to Table 5.2.5) shows a trend similar to that found with increasing load. This engine was not run at MBT therefore all phasing is based off of the stock spark timing at 18°bTDC; advancing and retarding the spark is relative to this stock timing.

Table 5.2.5: Combustion Performance Data for Ignition Timing Sweep

| Ign. Timing | Load | Speed | CA50 | CA10-90 | Time CA10-90 (ms) | COV |
|-------------|------|-------|------|---------|-------------------|-------|
| 30°bTDC | 25% | 3060 | 18 | 40 | 2.18 | 1.90% |
| 18°bTDC | | | 33 | 47 | 2.56 | 4.74% |
| 0°bTDC | | | 65 | 61 | 3.32 | 9.30% |

By retarding the spark timing, the burn duration increases significantly both on a physical and crank angle basis. With a majority of the combustion occurring after TDC, any fluid motion induced during the intake stroke has experienced compression, reducing the bulk flow motion and turbulence intensity. Ignition timing effects are independent of speed, load and depend weakly on spark location, therefore similar trends were observed at the other test points in the matrix.

5.2.4 Spark Location Effects on Combustion Performance

Spark plug location plays a significant factor on the heat release rate of a given combustion chamber design. Optimal plug location requires locating the ignition point near a region of high bulk flow motion for quick convection of the kernel or in an open, central location to allow the kernel to expand unabated by the chamber geometry. Due to packaging requirements for small engines, the spark plug is usually placed to allow easy access for maintenance, rather than optimal combustion performance. As shown earlier, (see Fig. 3.1.1) the stock and alternate plug locations are diametrically opposed in the cylinder, in between the exhaust and intake valves.

Although neither single spark position was optimized, Figs. 5.2.6 and 5.2.7 show that there are minor differences between spark location and heat release response

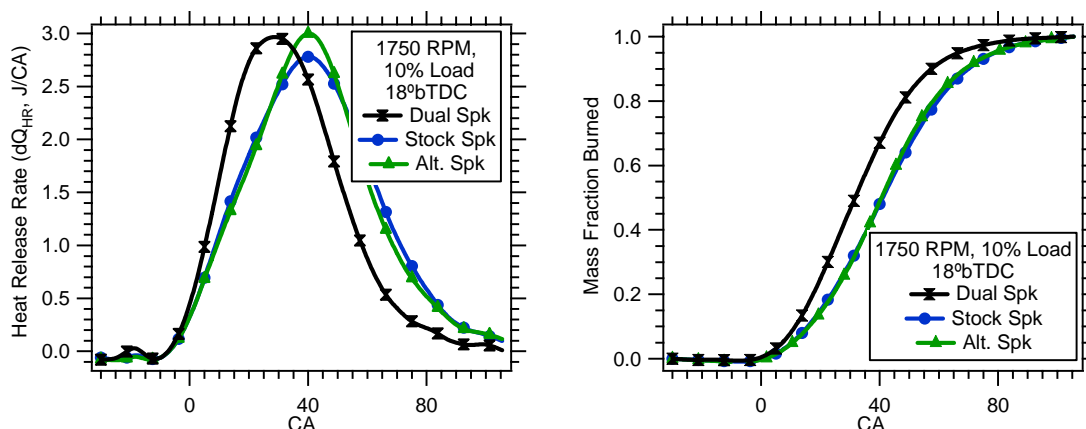


Figure 5.2.6: Variation of Heat Release Rate with Spark Position at 10% Load

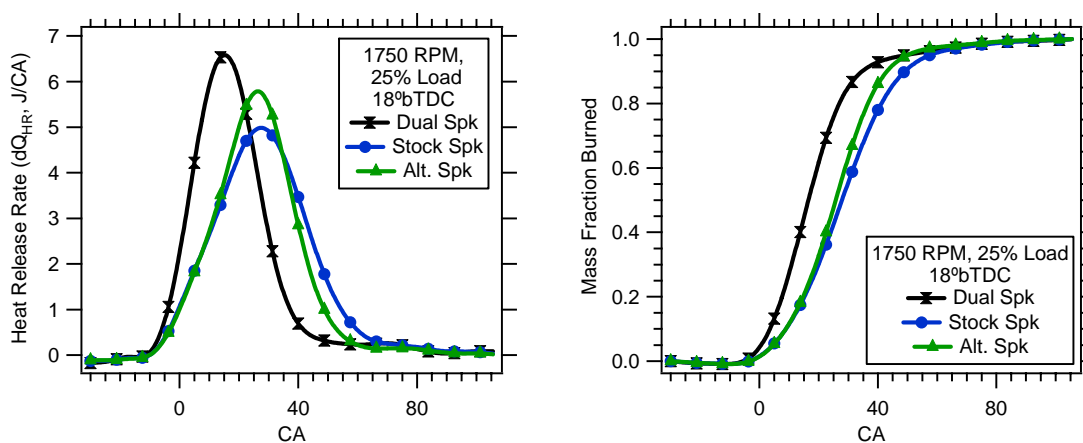


Figure 5.2.7: Variation of Heat Release Rate with Spark Position at 25% Load

As described previously, there is a significant change in heat release with load, but a near independence on engine speed on a crank angle basis, therefore only the two speed-load conditions are shown although similar trends exist at the higher speed.

The dual spark condition yields the highest heat release rate, effectively advancing the combustion phasing by entraining a greater volume of the chamber in the flame kernel earlier in the cycle due to the two independently propagating flame fronts.

Tables 5.2.6 and 5.2.7 represent the combustion performance for the different spark positions.

Table 5.2.6: Combustion Performance Data for 10% Load Spark Position Sweep

| Ign. Timing | Load | Speed | Spark Position | CA50 | CA10-90 | COV |
|--------------------|-------------|--------------|-----------------------|-------------|----------------|------------|
| 18°bTDC | 10% | 1750 | Stock | 40.5 | 58 | 8.67% |
| | | | Alternate | 41 | 56 | 10.12% |
| | | | Dual | 31.5 | 50 | 5.87% |

Table 5.2.7: Combustion Performance Data for 25% Load Spark Position Sweep

| Ign. Timing | Load | Speed | Spark Position | CA50 | CA10-90 | COV |
|--------------------|-------------|--------------|-----------------------|-------------|----------------|------------|
| 18°bTDC | 25% | 1750 | Stock | 27 | 43 | 4.08% |
| | | | Alternate | 25 | 36.5 | 4.02% |
| | | | Dual | 16 | 36 | 2.90% |

While the magnitude of the heat release rate of the alternate spark position is higher than the stock spark position the combustion phasing, as indicated by the mass fraction burned plot, only varies slightly from the stock position. The phasing advance indicated at the higher load can be attributed to the more favorable flow conditions at the plug gap relative to the stock position.

Note that there are significant differences again between the stock and alternate position single spark position in terms of burn duration and COV with similar combustion phasing. The dual plug consistently presents a lower burn duration due to the higher volume engulfed by the flame at the same given crank angle. This is also reflected in the decrease in COV resulting from a shorter time for variation in the flow to affect the kernel during the initial propagation phases.

The trends indicated in this section for a single spark timing are reflected through the spark sweeps presented in subsequent sections.

5.3 Dual Spark Sweep Effects on Heat Release Rate

To determine the effect of multiple spark locations on the combustion event, the spark timing was swept between 30°bTDC and 10°aTDC depending on the condition. Sweeping the spark timing allows the combustion to occur at different phasing to determine the influence of pressure, and flow pattern on combustion.

It was shown earlier that the dual spark conditions yield higher burn rates, as indicated by the advance of the mass fraction burned curve (refer to Figs. 5.2.6 and 5.2.7). To properly compare single and dual spark configurations, a similar combustion event must take place; this is accomplished by matching combustion phasing (CA50), i.e. the combustion timing effects in 5.2.3 are eliminated. In the following section, the combustion performance data are presented from a spark sweep of the conditions in the test matrix to study the effect of dual spark combustion across varying in-cylinder environments.

5.3.1 Combustion Phasing: CA50

In order to determine a location of a combustion event, one must choose the location of a “stable” point in the heat release rate and mass fraction burned curve away from any spark-induced noise and heat transfer effects. The location of 50% mass fraction burned (CA50) represents a stable point to reference the combustion phasing events relative to other parameters. Although halfway through MFB curve, CA50 still represents a linear relationship to the ignition timing (see Fig. 5.3.1).

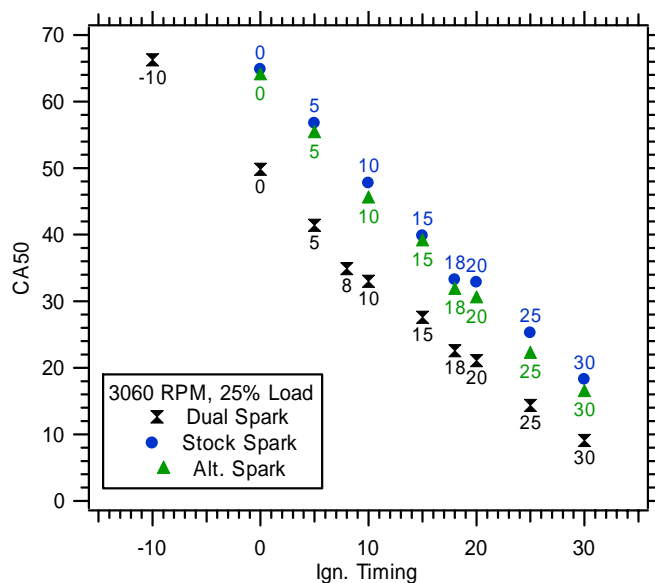


Figure 5.3.1: Direct Relationship between Ignition Timing and CA50 Phasing

The numbers listed next to the data symbols on Fig. 5.3.1 represent the spark timing for that condition; this convention will be used throughout the rest of the thesis. Examining the heat release rate and mass fraction burned curves, the similarity gained through matching combustion phasing is clearly evident (see Fig. 5.3.2).

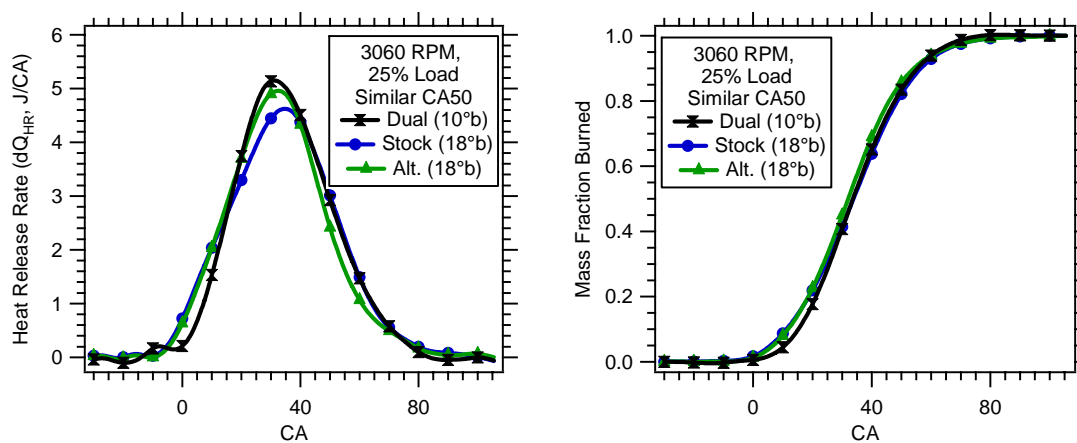


Figure 5.3.2: Matched Combustion Phasing Heat Release Rate Response

Only one speed and load condition is shown in the figure above but the linear trend between spark timing and CA50 was consistent independent of speed and load. This point represents

a stable value in the heat release unaffected by spark noise issues (common at earlier mass fraction burned positions, e.g. CA10) or heat transfer (an issue late in the cycle, e.g. CA90) and is within the turbulent flame regime.

5.3.2 Spark Timing Sweeps

Independent of speed and load, the combustion phasing is directly related to the spark timing. As shown in the previous section, CA50 is a stable combustion point on the mass fraction burned curve and will provide the indicator of combustion phasing relative to spark timing. As the combustion event changes significantly with CA50, there were significant changes in air and fueling rates in order to maintain a constant torque.

In §5.2.3, it was shown that spark timing can affect the heat release rate through the combustion phasing. Retarded spark timing pushes the combustion into an unfavorable decaying-turbulent regime resulting in long combustion duration. In section 5.2.4, it was shown that the combustion duration also is dependent on spark position in the combustion chamber. Both of these features can be indicated through the spark timing sweeps. In Fig. 5.3.1, the dual spark configuration shows an advanced CA50 phasing (6 to 14° advance) for equivalent spark timing at the single spark locations. The alternate spark location is consistently advanced from the stock spark location by 1 to 2°CA. These trends are consistent with those discussed in sections 5.2.2 and 5.2.3.

5.3.2.1 Mean Best Torque Spark Timing

“Mean Best Torque” spark timing, or MBT, presents the highest possible torque for a given air and fuel flow rate. MBT timing allows for an optimum balance of positive work (pressure after TDC) and negative work (pressure before TDC) that will reduce peak pressures and therefore temperatures, reducing the tendency for knock and engine noise. By

advancing the spark timing, a significant portion of the pressure generated from the heat release will result in negative work on the piston as it precedes TDC. Retarded spark timing results in a majority of combustion occurring after TDC with a receding piston, therefore the heat release and pressure forces are not utilized properly. Operating at MBT results in the best burn duration (CA10-90) for a speed and load condition due to the pressure effects. For a constant throttle position, MBT represents the highest torque possible for this given speed and load. Since all tests were conducted with constant speed and load, MBT can be indicated through a minimum in the brake specific fuel consumption (BSFC) (see Fig. 5.3.3).

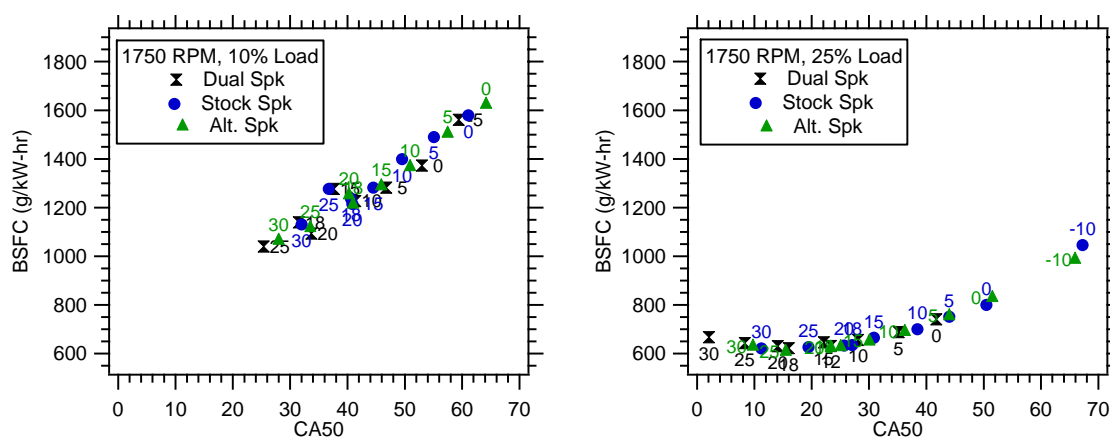


Figure 5.3.3: BSFC to indicate MBT for the Spark Sweep Tests

Fig. 5.3.3 represents two examples of the conditions experienced in the tests; all conditions, with the exception of 1750 RPM, 25% Load, responded as indicated by the 1750 RPM, 10% Load condition with a decrease in BSFC with advancing combustion. The 1750 RPM, 25% Load condition passes through a minimum around 25° and 20°bTDC for the single and dual spark configurations respectively, representing the MBT for this condition and spark position. Passing through this condition will be present in all subsequent data and must be taken into account.

5.3.3 Burn Duration

Burn duration is defined to be the period, in crank angles, between 10% and 90% mass fraction burned. This period describes a major portion of the lifespan of the flame; from initiation and transition to a turbulent flame (around CA10) to quenching (around CA90); the data are plotted against CA50, combustion phasing to allow a comparison between similar conditions with different spark timing. Fig. 5.3.4 presents the burn duration response for all test conditions across varying combustion phasing.

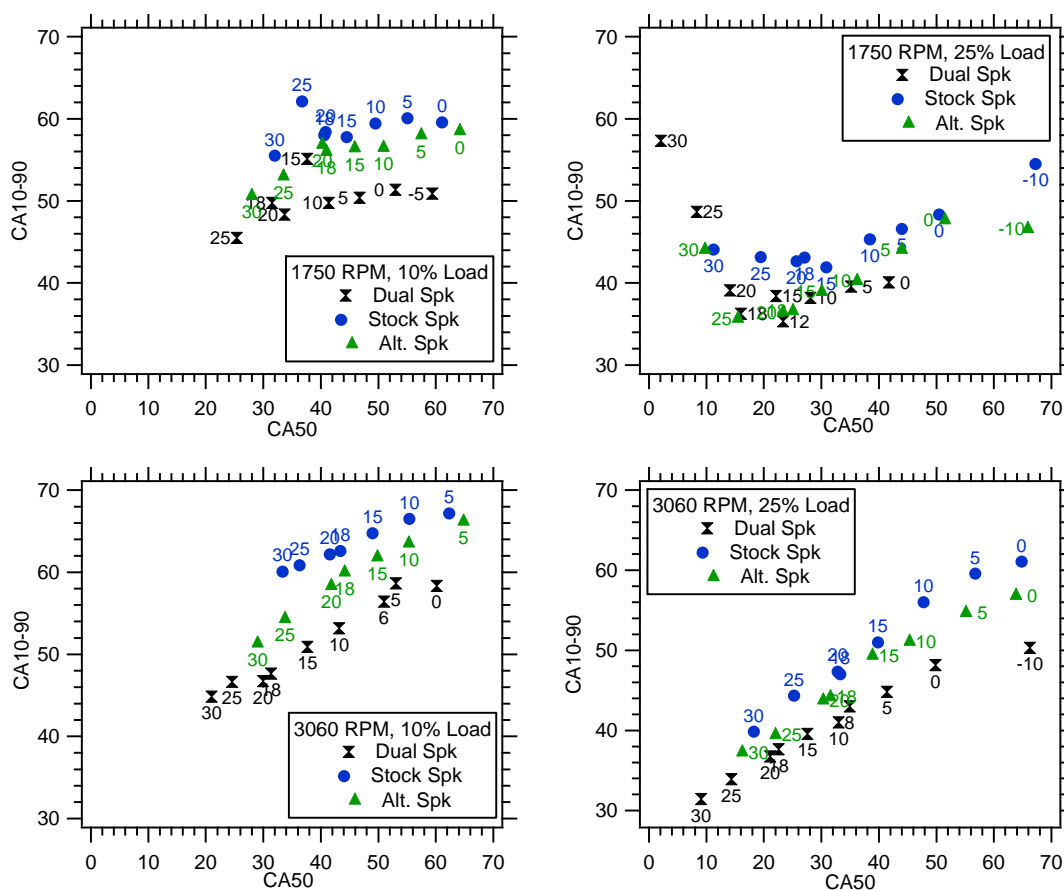


Figure 5.3.4: Burn Duration Response to Varying Spark Positions

The dual spark configuration for all conditions provides the lowest burn duration for a given spark timing due to the higher burned gas volume per crank angle from the two independent

flame fronts. Note that the nonlinear response at 1750 RPM, 25% load as described in section 5.3.2.1, is due to the system passing through MBT resulting in a minimum for the burn duration. Note that the dual spark and alternate spark location have similar trajectories; similar burn duration can be achieved with the alternate spark as the dual spark, albeit with slightly more advanced spark timing.

The stock spark position consistently yields the longest burn duration independent of speed and load. The differences between the stock and alternate spark location are indicative of differences of bulk motion experienced at each position.

By advancing the combustion at a constant torque, the engine can take advantage of the turbulence present near TDC allowing for a lower burn duration.

5.3.4 Flame Propagation

In order to achieve the highest burn rate with the dual spark configuration, the flame must be held independent of the walls and other flame fronts. Any interaction would be indicated as an increase in the flame propagation period (CA10-50) (see Fig. 5.3.5).

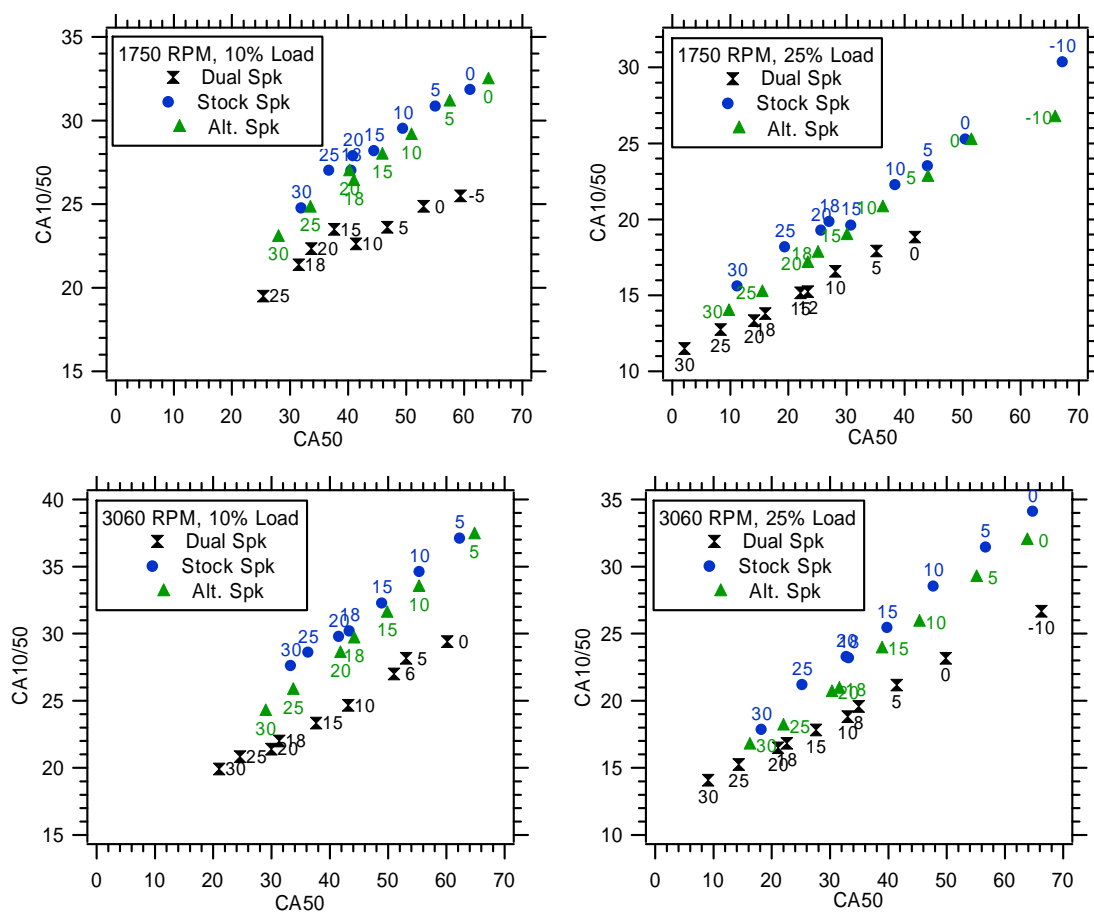


Figure 5.3.5: Flame Propagation Response to Varying Spark Positions

All conditions show the same linear response of CA10-50 to combustion phasing (CA50) as with the burn duration period. Again, as stated in literature, the dual spark configuration will yield the shortest burn duration during the period of independent flame propagation which should be indicated during the flame propagation period of CA10-50.

The dual spark configuration consistently reduces the flame propagation period 5 to 10°CA relative to a single spark position at the same spark timing. A condition with similar combustion phasing indicates a decrease in flame propagation of 5°CA. The decrease of CA10-50 is independent of speed and load. This can be attributed to the higher burned gas

volume per CA from the two flame fronts. With a higher burned gas volume, there is an increase in mass fraction burned presenting the advance in combustion.

At highly retarded spark timing, there is a more pronounced effect of the dual spark configuration compared to the single spark conditions. For similar combustion phasing at highly retarded spark timing, the dual spark configuration can decrease the CA10-50 period up to 10°CA. This can be attributed to the unfavorable turbulent conditions present later in the cycle. At these conditions, the dual spark configuration can take advantage of the poor condition because of the two independent flame fronts. The single spark location relies on the probability that the turbulence is near that location. The dual spark configuration increases the probability of favorable turbulence near both locations, also decreasing the COV therefore creating a stable flame front early in the cycle utilizing the unfavorable turbulent conditions.

The differences in flame propagation period between the stock and alternate spark location can be attributed to two conditions. First, the alternate spark location has an electrode that protrudes further into to the combustion chamber than the stock spark location. This can allow the young flame kernel to experience more of the in-cylinder turbulence, increasing the probability that a stable flame can be established early in the cycle. The stock spark location is slightly shrouded by the head which might also reduce the ability for the early kernel to experience any fluid movement. Secondly, heat transfer effects and the quenching effect from shrouding the spark plug can draw useful energy away from the initial flame kernel to the cylinder wall as waste heat.

5.3.5 Flame Termination

As the heat release progresses later in the cycle, the combustion becomes dominated by heat transfer effects. This late-cycle combustion period can be defined by the heat release rate between 50% and 90% of the mass fraction burned curve (CA50-90) as the flame interacts with the chamber geometry and quenches (see Fig. 5.3.6).

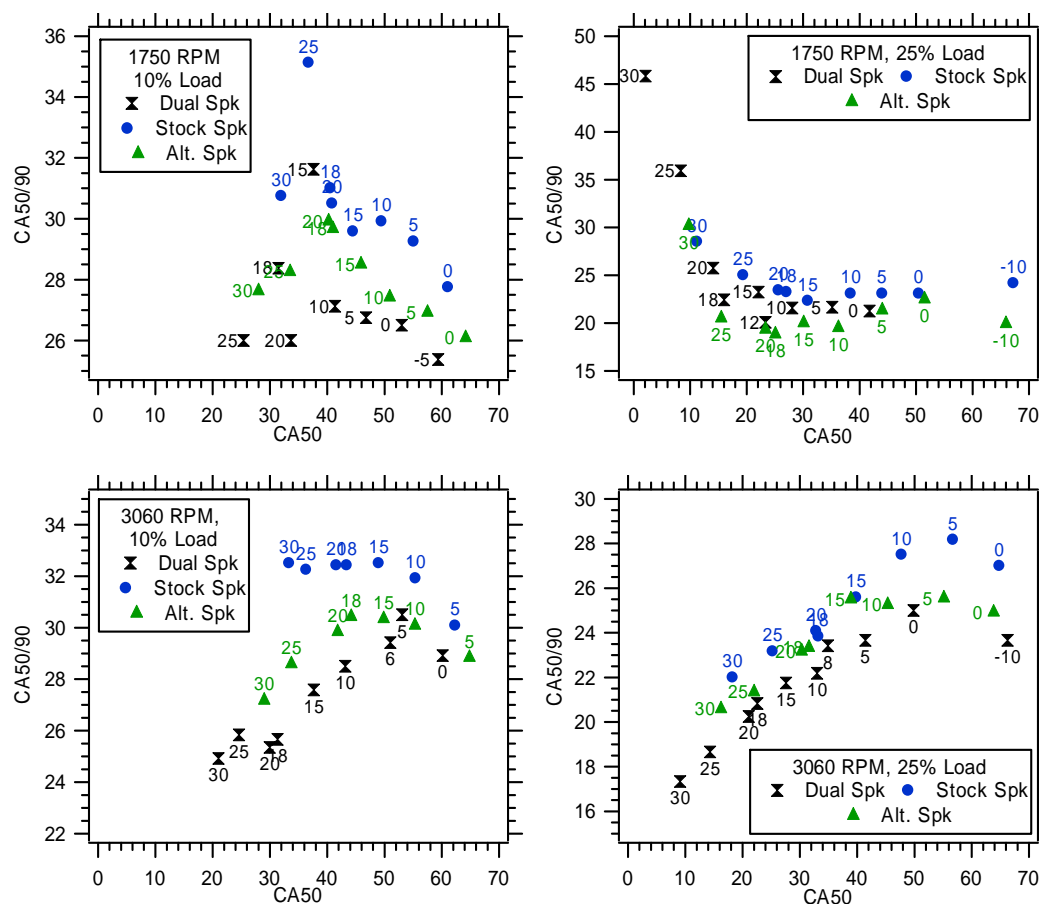


Figure 5.3.6: Flame Termination Period for Varying Spark Positions

Note the y-axis range of the flame termination period, CA50-90, is significantly smaller than for the flame propagation period, CA10-50. This highlights that there is little variation between conditions at this later heat release period yielding a small overall change in the heat release.

The dual spark configuration consistently yields the lowest CA50-90 period. The “peak” observed in the 1750 RPM, 10% Load, and 3060 RPM, 10 and 25% Load conditions is an indication of a condition with heat release past EVO. As combustion phases later, CA90 becomes less accurate as a significant portion of the heat release is after EVO resulting in a breakdown of the closed system assumption necessary for the First Law heat release equations. CA90 then becomes less and less sensitive to further retard while CA50 continues to follow a linear trend with spark retard.

Once the in-cylinder condition reaches CA50, there is less of an impact on burn duration from a dual spark configuration from the flame termination period than the flame propagation period. Literature suggests this is due to the dual flames now coalescing into a single flame front, losing the ability to quickly use up the in-cylinder charge. Although this experiment had no way to determine the flame front, the influence determined by the magnitude change during the flame propagation and flame termination period could be interpreted as an indication of independence during the initial stages of flame propagation. Since the magnitude between conditions during CA10-50 is larger (5 to 10°CA) than CA50-90 (about 2 to 3°CA) there is a greater influence on the combustion duration during the flame propagation leading to the assumption that the two flames are still independent during this period.

5.3.6 Heat Transfer Effects on Heat Release

Heat transfer effects on the heat release rate are not significant until late in the cycle due to the increasing surface-to-volume ratio exposed to the hot exhaust gas. Heat transfer to the cylinder walls can lead to a loss of energy converted to useful work. With the dual spark configuration there is an increase in burned gas volume at a given crank angle due to the

independent flame fronts, which leads to a significant portion of the combustion chamber exposed to hot product gases earlier in the cycle. From the energy balance in the first law heat release equations, the heat transfer rate can be calculated (see Fig. 5.3.7) for the entire cycle.

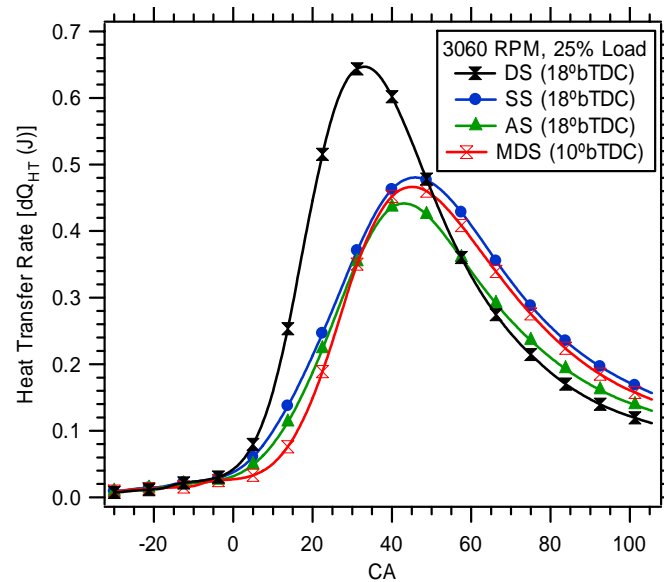


Figure 5.3.7: Heat Transfer Rate for Dual Spark and Single Spark Combustion

For similar spark timing, the dual spark configuration yields the highest heat transfer as would be expected from the advanced combustion. By retarding the spark timing, a similar heat transfer rate can be obtained as indicated by the matched dual spark timing (MDS) at 10°bTDC , which has the same CA50 phasing as the single spark conditions. Note that during the latter part of the cycle, heat transfer for the dual spark configuration at 18°bTDC has a lower response past a crank angle of 60° , indicating a lower exhaust gas temperature. As one would expect, with retarded combustion events the exhaust temperature was slightly higher.

Since the dual spark conditions yield the highest heat transfer rate, one can see this as a negative effect on the desired outcome of increased power from the engine. A significant portion of the energy released during the fast combustion results in heat loss to the chamber walls. This is one of the negative outcomes of advanced combustion and a dual spark configuration. Only one condition is shown here, but the trends were consistent across all speeds and loads of the test matrix.

5.3.7 Dual Spark Combustion Conclusions

A dual spark combustion chamber reduces the burn duration for a given condition by effectively advancing combustion. This is accomplished by the propagation of two independent flame fronts resulting in a higher burned volume fraction for a given crank angle assuming similar spark timing. For similar combustion phasing, CA50, the dual spark configuration yields the shortest burn duration. The main contribution to burn duration is evident in the flame propagation period, CA10-50, where two independent flame fronts exist (see Fig. 5.3.5). Once the flames coalesce into a single flame front, the benefit from dual spark combustion diminishes considerably as evident in the flame termination period, CA50-90 (see Fig. 5.3.6). Heat transfer poses a problem to dual spark combustion due to the increased flame surface area for small swept volumes increasing the heat transfer rate to the wall early in the cycle.

A dual spark configuration can reduce the light-load, low-speed slow combustion issues in utility engines, but due to the small combustion chambers, little room is available for a second spark plug and a second magneto system. Although the dual spark data presented above has indicated an increase in the combustion rate, this modification alone is not the ultimate answer to alleviate light load burn rate issues.

5.4 Combustion Phasing Effects on Emissions

As stated earlier, the main purpose of changing the spark timing is to change the combustion phasing; retarding the spark timing places main combustion later in the cycle. The effect of spark timing on the heat release rate was shown (in section 5.2.3) to be significant, by placing the main combustion in various in-cylinder environments of pressure and bulk motion decay. Changes in combustion strategy and heat release lead to a significant change in exhaust emissions. Phasing main combustion late in the cycle places heat release in the chamber with a rapidly retreating piston, reducing peak pressures. In Fig. 5.4.1, a minimum of peak pressure is reached with spark timing at each of the spark positions near TDC, i.e. retarded CA50.

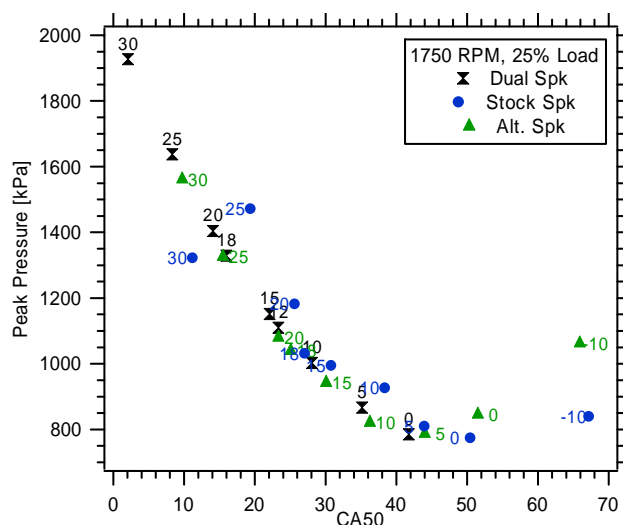


Figure 5.4.1: Peak Pressure Response with Retarded Combustion

With combustion occurring later in the cycle at spark timing after TDC, the polytropic compression becomes the dominant peak pressure in the system rather than combustion-induced pressure, hence the slight increase at highly retarded spark timings. Phasing the

combustion later in the cycle also increases the exhaust gas temperatures as less useful work is extracted from the charge (see Fig. 5.4.2).

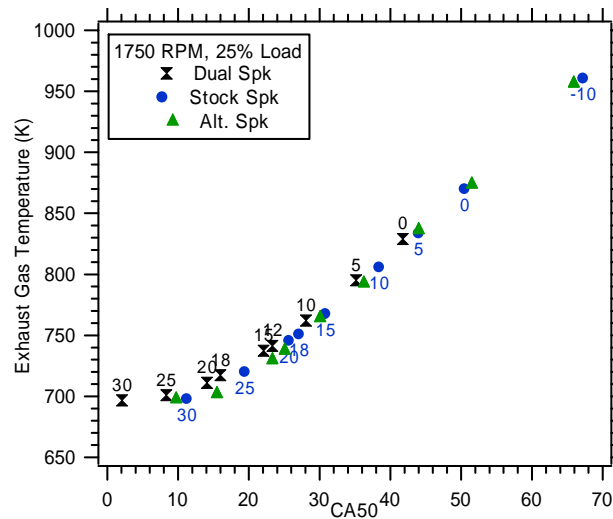


Figure 5.4.2: Exhaust Gas Temperature Response with Combustion Phasing

The exhaust gas temperature has a near linear relationship with combustion phasing independent of spark position. Although only one speed and load condition is shown in the preceding figures, all of the trends were consistent at other conditions.

5.4.1 Retarded Spark Timing Effects on Burn Rate

In section 5.2.3, it was shown that changing the spark timing has a significant effect on the heat release rate and therefore burn duration (refer to Fig. 5.3.3). Independent of spark position, speed and load, the burn duration increases for retarded combustion due to the decaying and unfavorable in-cylinder fluid motion.

5.4.2 Retarded Spark Timing Effects on HC Emissions

Retarded spark timing is common in a cold start of an automotive engine to increase the exhaust gas temperatures and quickly bringing the catalyst up to operating temperature. Without a retarded timing strategy, a slug of HC would escape the engine due to the cold and

ineffective catalyst. Although non-handheld utility engines do not currently employ exhaust after-treatment, retarded spark timing conditions present a simple method to reduce exhaust emissions.

5.4.2.1 EIHC Emissions Response

Emissions index (EI) expresses the amount of pollution independent of dilution of the product species or combustion efficiency [30]. Increased exhaust gas temperature and reduced peak pressures is favorable for reducing HC emissions through enhanced post-oxidation and reduced ring pack effects, respectively. As combustion is phased later in the cycle, the EIHC reduces nearly linearly (see Fig. 5.4.3).

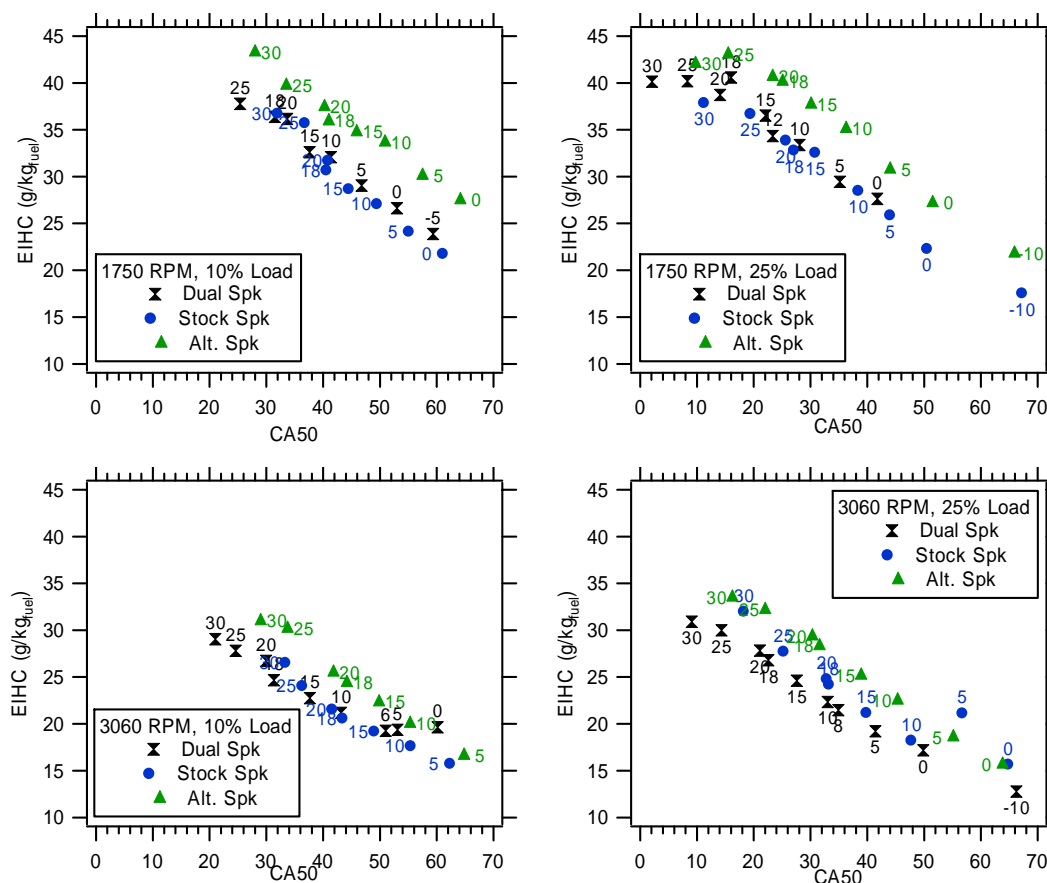


Figure 5.4.3: EIHC Emissions Response Due to Combustion Phasing

As clearly indicated in Fig. 5.4.3, spark position has a significant effect on EIHC emissions response. The dual spark and stock spark configurations follow a similar trend across nearly all speed and load conditions while the alternate spark position consistently yielded a higher EIHC. Since the dual spark configuration has higher peak pressures one would expect an increase in HC emissions in comparison to a single spark condition due to the importance of the ring pack, but this is not immediately evident. At similar spark timing, the single spark configurations yields similar HC emissions independent of position, but dual spark conditions are significantly higher primarily due to the ring pack effects. For an equivalent combustion phasing, pressure response is similar and for all spark configurations independent of spark timing, and the HC emissions are similar.

Using the ring pack HC model developed by Salazar [3], the influence of heat release on engine-out HC emissions was examined. The EIHC of mixture released from the ring-pack response from the end of flame propagation (CA90) to EVO was used to estimate the influence of the ring pack on the unburned HC available for in-cylinder oxidation (refer to Fig. 5.4.4).

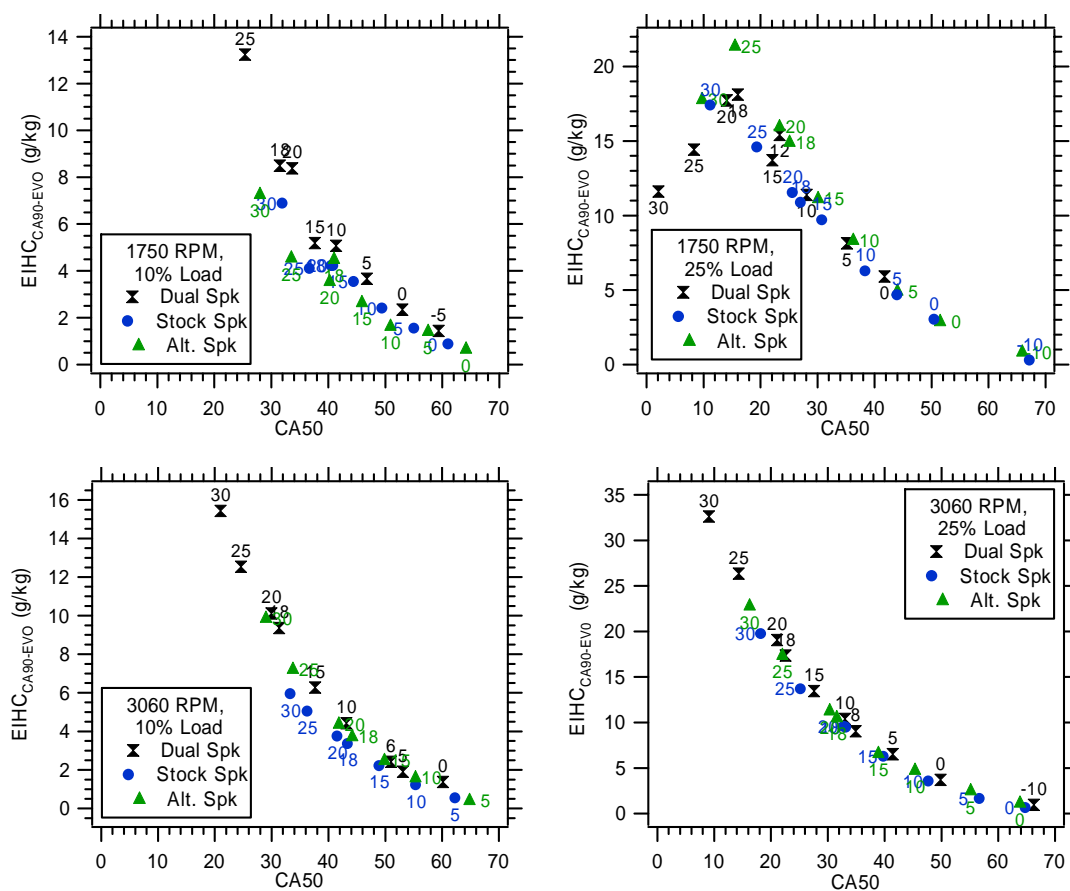


Figure 5.4.4: EIHC_{CA90-EVO} Emissions Response Due to Combustion Phasing

Independent of speed, load and spark position, the effect of the ring pack on engine-out HC emissions approaches zero with retarded spark timing. Increasing the load, results in higher ring pack loading due to increased peak pressures. Poor combustion quality and incomplete combustion have been found to be a significant contribution to HC emissions at light-load conditions as well [1]. For similar combustion phasing, the single-spark emissions value are the same as the dual-spark configuration, while for constant spark timing the dual-spark configuration gives the highest ring-pack HCs. From the ring-pack analysis it was determined that under highly retarded spark conditions, the effects of the ring pack on the engine-out HC emissions can be reduced independent of speed, load, number of ignition sites and spark position.

Returning to the overall EIHC response (see Fig. 5.4.3), the consistently high response from the alternate spark position is clearly not due to the ring pack (see Fig. 5.4.4). Since this position also yields a lower burn duration (see Fig. 5.4.2), incomplete combustion is not a main contribution as well. Poor in-cylinder mixing may retain a pocket of unburned HC near the exhaust valve with the alternate spark position, but without detailed in-cylinder flow visualization, this hypothesis is unproven. Uneven ring-pack loading or ring gap position relative to the spark position may yield higher ring-pack effects [3] due to a side spark location resulting in the EIHC offset from Fig. 5.4.3.

5.4.2.2 Mass-Based HC Emissions Response

From Figs. 5.4.3 and 5.4.4, it can be seen that the EIHC can be reduced up to 50% by retarding the spark timing from the stock timing. The reduction in EIHC is expected due to the increase in fueling rate by which the emissions index is normalized. On a mass basis, other trends emerge that reflect the change in fuel flow.

To determine the mass-based HC emissions on a cycle basis, the fuel per cycle and EIHC must be measured. This value represents the mass of HC leaving the engine, or exhaust HC (refer to Fig. 5.4.5).

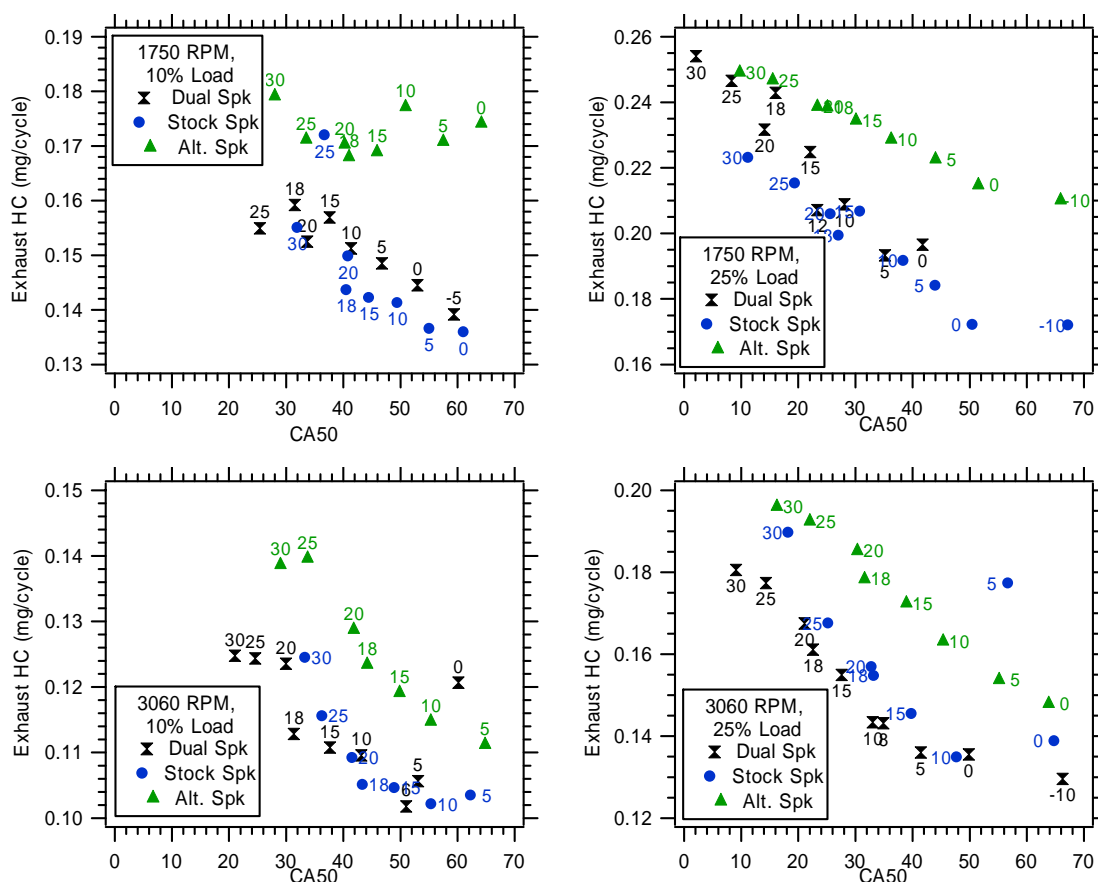


Figure 5.4.5: Exhaust HC Emissions Response Due to Combustion Phasing

The trends of exhaust HC emissions differ slightly from the monotonically decreasing EIHC response; (see Fig. 5.4.4) a slight non-linearity is observed at the highly retarded timing conditions. The alternate spark position consistently yields higher exhaust HC than the dual and stock spark configurations.

5.4.2.3 Oxygen Concentration Response

Although oxygen is very limited in a rich combustion regime, a linear decreasing trend in O_2 with retarded combustion phasing was observed in Fig. 5.4.6.

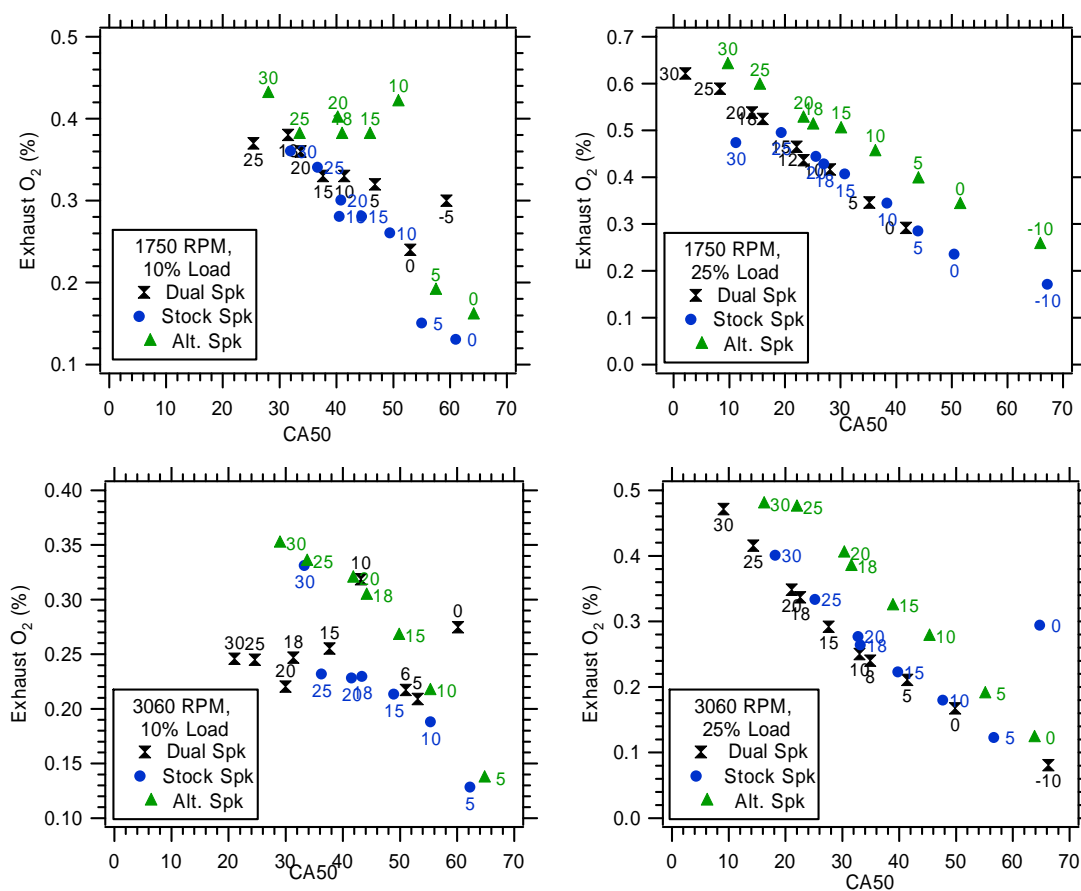


Figure 5.4.6: Exhaust O₂ Emissions Response Due to Combustion Phasing

The existence of any O₂ in the exhaust is puzzling, but two possibilities for the response in Fig. 5.4.6 can be suggested. As shown in Fig. 5.4.5, the ring pack can store a significant amount of the intake charge consisting of fuel and air. The small amount of O₂ stored in this crevice that escapes post-oxidation can explain the indicated response. Flame quenching also can create a protected region near the cool wall which can trap reactants escaping main combustion.

Since the OH radical has been found to be important in HC oxidation, the existence of O₂, or lack thereof, should indicate the size of the radical pool available for oxidation [14]. Comparing the mass-based HC emissions to the O₂ concentration indicates the maximum possible HC oxidation for a given operating condition (see Fig. 5.4.7).

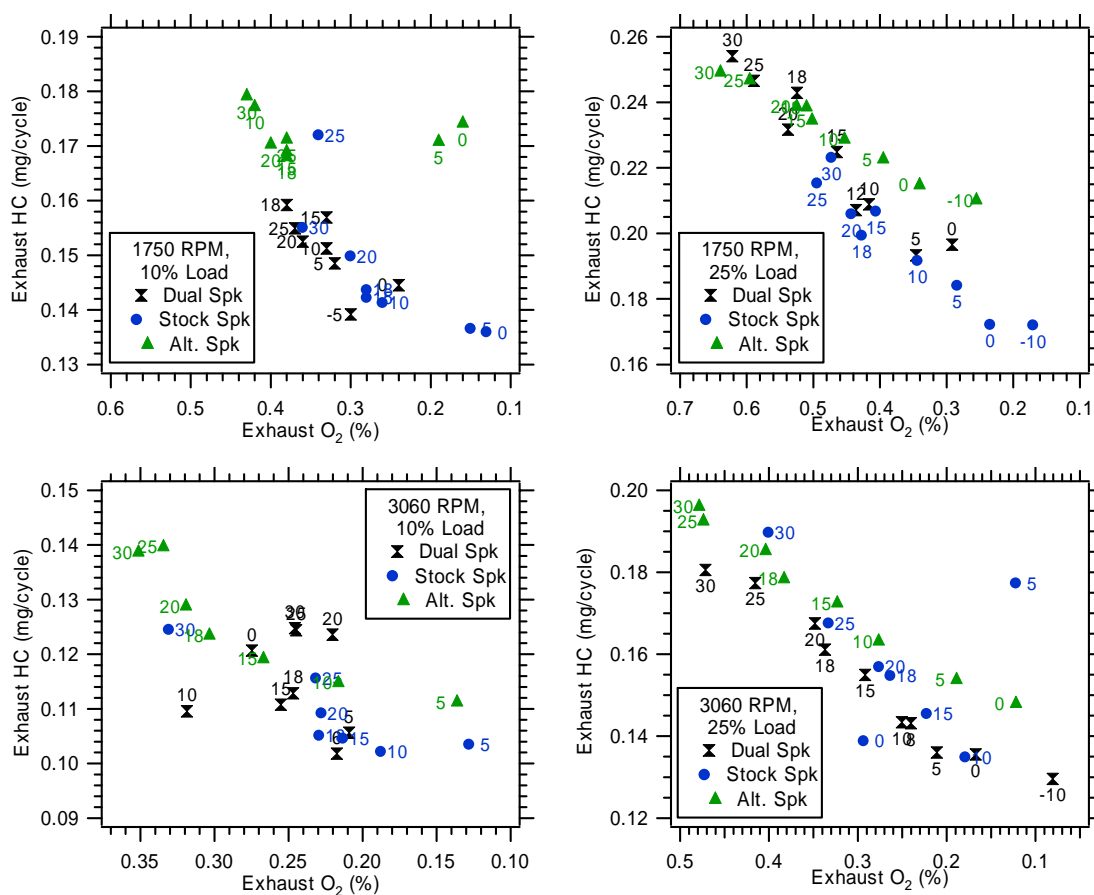


Figure 5.4.7: Exhaust HC Response to Reduced O₂ Levels

The plateau in HC, first indicated in Fig. 5.4.4, again reappears at O₂ concentrations between 0.2-0.3%. Once the O₂ concentration drops to a certain value, the production of the OH radical is insufficient to support any further HC oxidation. This plateau indicates any oxidation processes have run to completion due to an insufficient radical pool and the maximum HC in-cylinder oxidation has occurred.

5.4.3 Retarded Spark Timing Effects on NO_x Emissions

Increased in-cylinder temperatures favor NO_x formation as predicted by the Zeldovich mechanism. The response of NO_x concentration is then expected to decrease with retarded combustion phasing due to the temperature dependency, but this is not always realized (see Fig. 5.4.8).

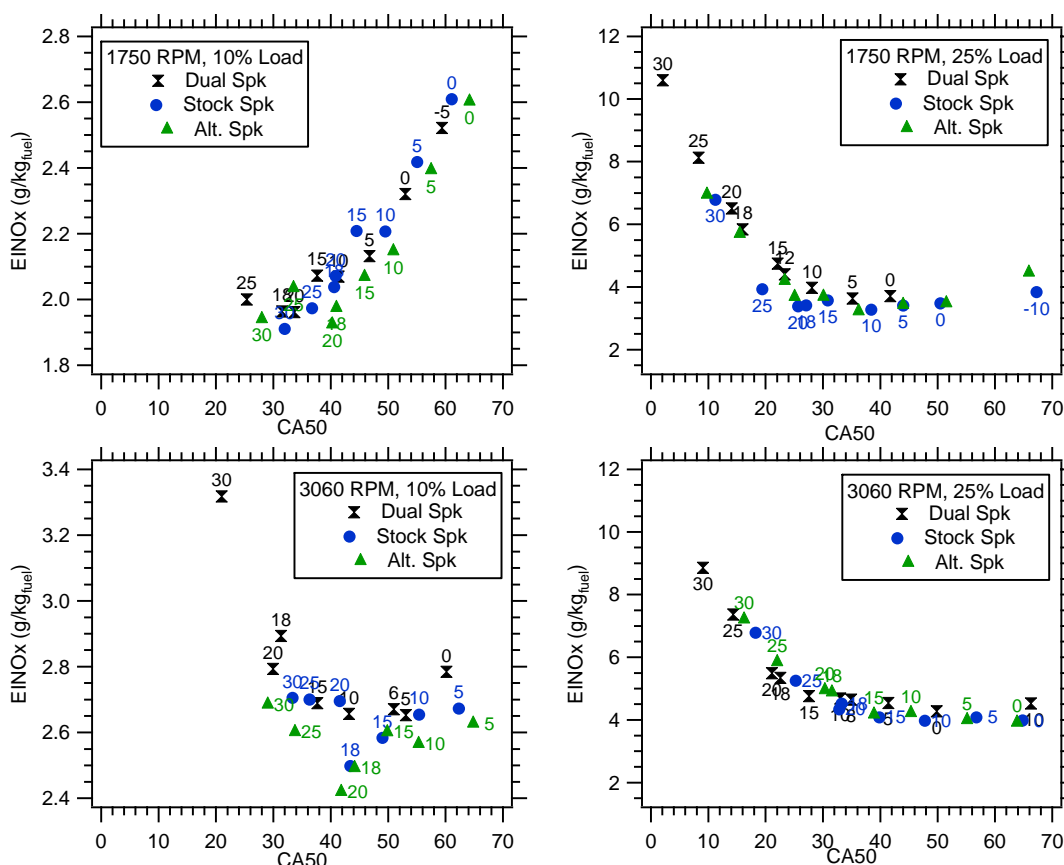


Figure 5.4.8: NO_x Emissions Response Due to Combustion Phasing

The overall trend for the conditions examined is a decrease in exhaust NO_x formation with retarded combustion phasing, except the 1750 RPM, 10% load condition which had a significant increase in NO_x although the magnitude is small compared to the HC levels. The trends are independent of spark location, with all configurations following the same path. Only highly advanced dual-spark combustion yields a significant change from this trend. This leads to the indication that two, locally hot regions (near the spark electrodes) do not yield a significant increase in NO_x under these conditions at constant CA50.

5.4.4 COV Effects on Heat Release

The coefficient of variance (COV) of IMEP is an indication of combustion stability and “driveability” in automotive engines. The COV for this engine is very dependent on load (see Fig 5.4.9).

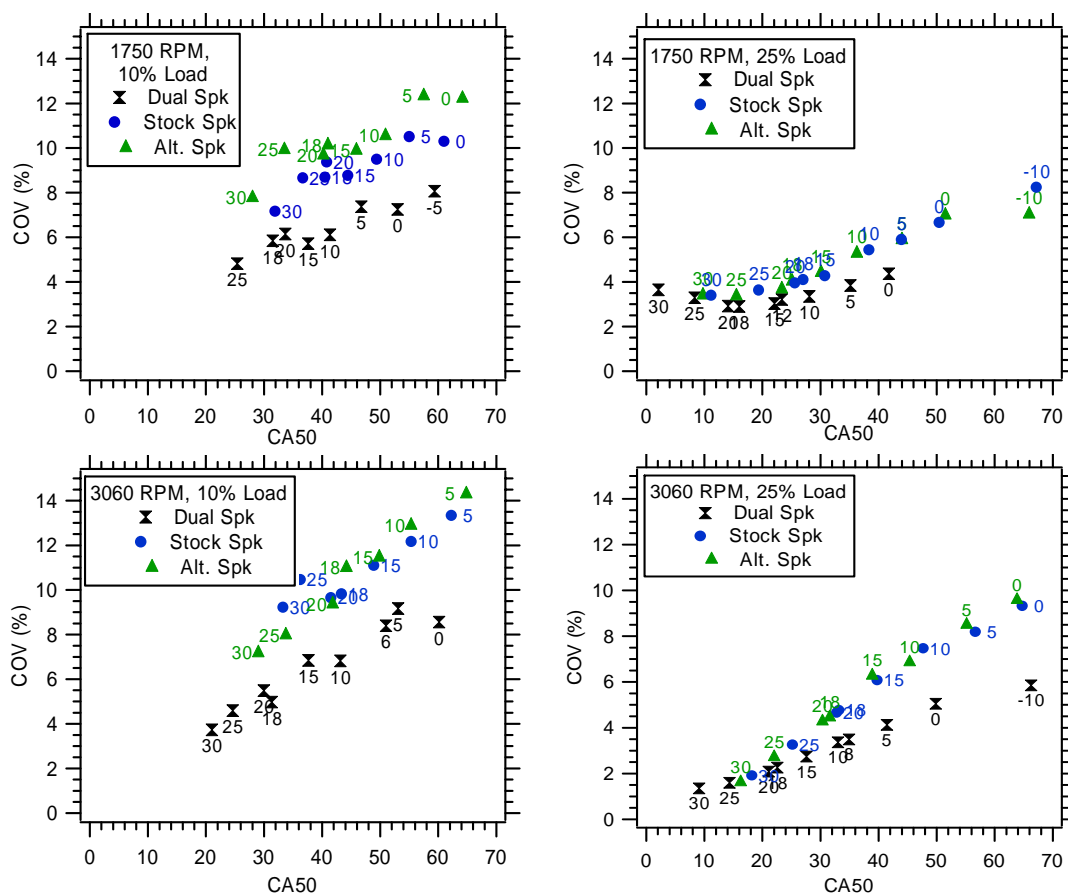


Figure 5.4.9: COV Effects from Dual Spark Combustion

From the figure above, it is obvious that the light-load conditions are highly variable, independent of engine speed. The COV for these conditions is highly dependent on the number of ignition points, rather than spark location due to the lower burn duration reducing the physical time that the influential flame size is on the order of the fluctuating turbulence. Once the flame reaches a sufficient size, enough of these small turbulent structures affect the

curvature of the flame so that the net effect is less noticeable. Again, this is due to the increase in burned volume for a given crank angle from the two independent flames.

5.4.5 COV Effects on Emissions

Previous work has shown that poor combustion quality (high COV) does not necessarily lead to poor emissions characteristics [1]. The HC emissions from dual-spark combustion is higher at fixed timing, than the single-spark combustion due to the ring pack effects, but the COV for dual-spark conditions are significantly lower. From Fig. 5.4.10, the COV is not necessarily a clear indicator of poor HC emissions.

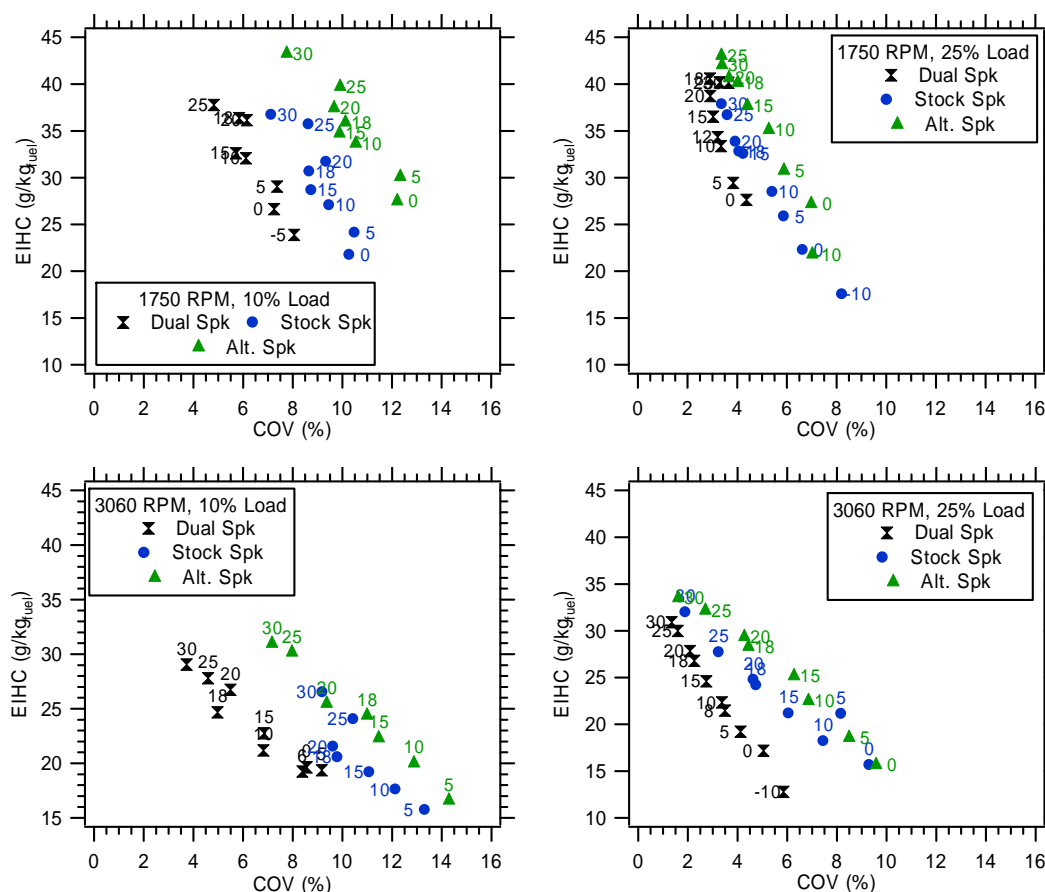


Figure 5.4.10: EIHC Emissions Response from COV Effects

The overall decreasing HC with increased COV is an opposite trend of those expected. This effect is driven by the change in combustion phasing.

The $EINO_x$ emissions also have little relationship to COV (see Fig. 5.4.11).

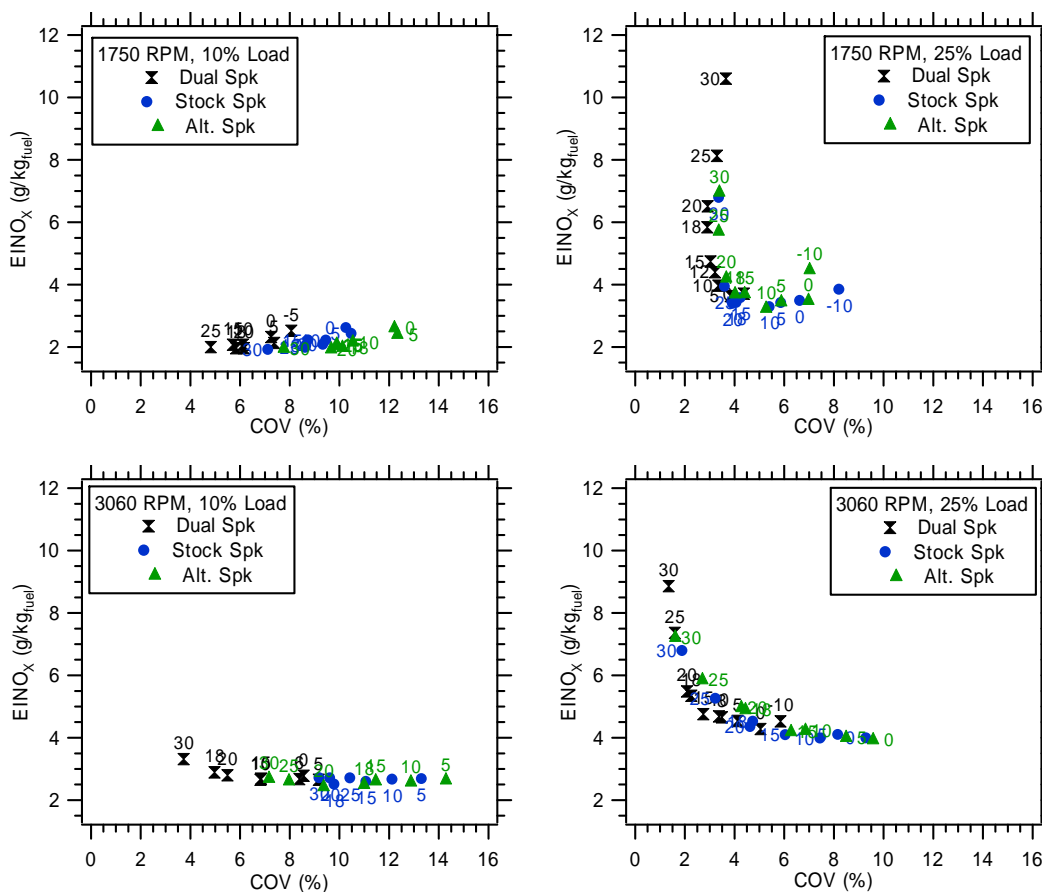


Figure 5.4.11: $EINO_x$ Emissions Response from COV Effects

Independent of speed and load, $EINO_x$ collapses along the same path for each spark position. The single-spark conditions, which have similar COV, have similar NO_x trends whereas the dual spark conditions tend to have slightly higher NO_x for similar spark timing and COV.

Both EIHC and $EINO_x$ show little relationship to COV and therefore combustion quality. For highly retarded spark timing, the COV increases due to the unfavorable in-cylinder bulk motion, but as found by Haugle poor emissions characteristics are weakly dependent due to combustion instability [1].

5.4.6 Combustion Phasing Emissions Conclusions

A significant reduction in HC emissions can be realized independent of speed, load, number of ignition points and spark location through retarded spark timing. This effectively reduces peak pressures and increases exhaust gas temperatures greatly aiding the oxidation of hydrocarbons escaping main combustion. HC oxidation was shown to be dependent upon combustion phasing, to allow enough time for an out-gassing of stored ring-pack products, and on O₂ concentration, to allow for the chemical kinetics reactions to have a sufficient radical pool for oxidation. The EIHC response was found to hide significant trends due to the normalization based on the amount of fuel used for combustion. Mass-based HC response indicated an effective minimum level of emissions possible for a given operating condition based on combustion phasing and oxygen content. With significant combustion phasing, all of the cycles are completing after EVO, but no significant increase in HC is indicated. NO_x emissions were found to be independent of the number of ignition points and decrease with retarded combustion even with the increase in exhaust gas temperature. This effect was attributed to the reduced in-cylinder temperature at the time of ignition. All of these factors contribute to an improved emissions response from retarded combustion phasing.

5.5 Engine Replacement

Over the course of the data collection for this thesis, the engine block was replaced with a new, identical engine block. This was done to ensure a constant response from the emissions. This particular engine has to meet EPA emissions standards for 125 hours with a

useful life span of 250 hours. It was found after 140 hours, the HC emissions were trending upwards with each consecutive test.

The HRR and MFB curves are nearly identical for the two engines (see Fig. 5.5.1), but the emissions are considerably different (see Table 5.5.1, Fig. 5.5.2, Fig. 5.5.3 and Fig. 5.5.4).

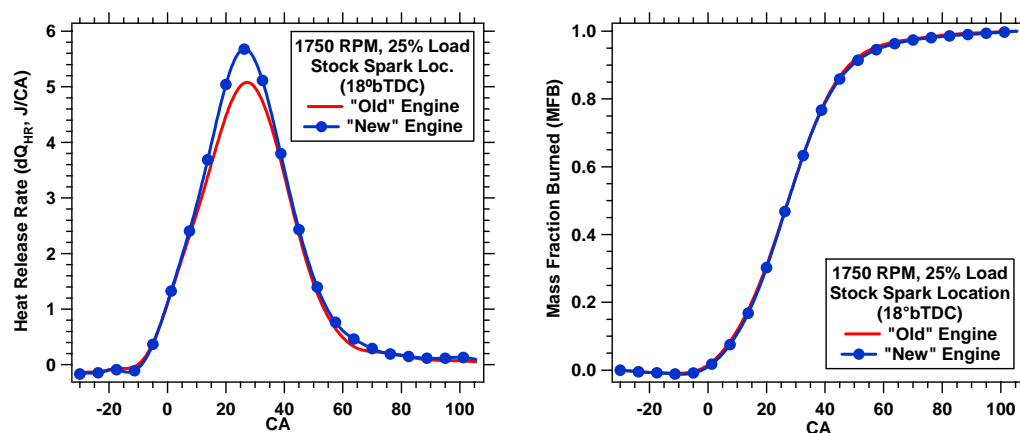


Figure 5.5.1: HRR from the Old and New Engine

Table 5.5.1: Engine Comparison of HRR and Emissions

| Engine | CA50 | CA10-90 | EIHC [g/kg] | EINO _x [g/kg] |
|--------|------|---------|-------------|--------------------------|
| Old | 27 | 39.5 | 32.8 | 3.41 |
| New | 27 | 40 | 25.9 | 4.48 |

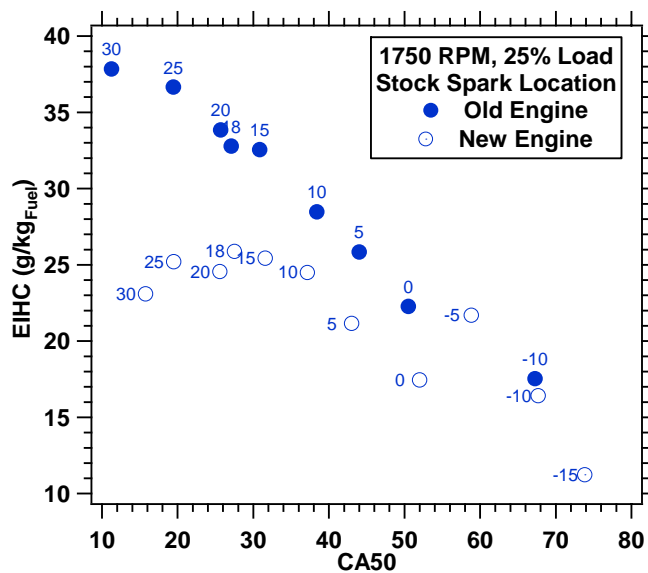


Figure 5.5.2: EIHC Response with Retarded Spark Timing Sweep from the Old and New Engine

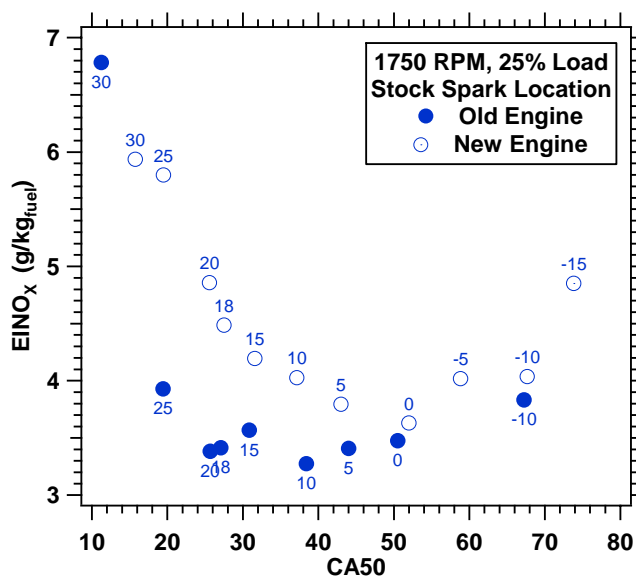


Figure 5.5.3: EINO_x Response with Retarded Spark Timing Sweep from the Old and New Engine

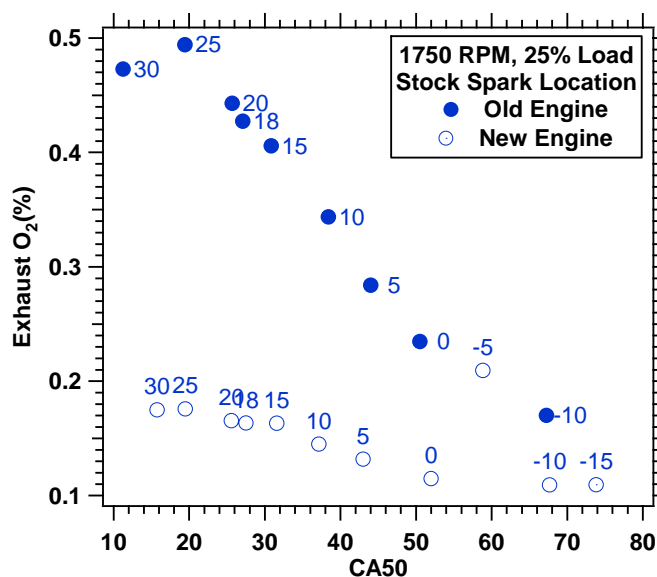


Figure 5.5.4: Exhaust O₂ Response with Retarded Spark Timing Sweep from the Old and New Engine

Although the engine block was replaced, the same head was used, but cleaned between tests. The data shown in subsequent sections of this chapter was recorded using the “new” engine block.

5.6 Swirl Enhanced Flow Field Effects on Heat Release

5.6.1 Swirl-Enhanced Condition Comparison

Across all of the speeds and loads, the swirl-enhanced condition provided an advanced combustion phasing. The improved bulk flow advanced the combustion and reduced the burn duration and COV to levels similar to that of the dual spark combustion conditions (see Tables 5.6.1 through 5.6.4), and indicates a significant advance in the combustion as indicated in the MFB curve (see Fig. 5.6.1 through 5.6.4).

Table 5.6.1: Variation of Heat Release Parameters with Spark Position and Swirl for 1750 RPM, 10% Load

| Spark Position | CA50 | CAIgn-10 | CA10-50 | CA50-90 | CA10-90 | COV % |
|------------------------------|------|----------|---------|---------|---------|-------|
| Stock | 41.5 | 34 | 25.5 | 29.5 | 55 | 8.7 |
| Alternate | 42 | 35 | 25 | 28 | 53 | 10.1 |
| Dual Spark | 32 | 29.5 | 20.5 | 26 | 46.5 | 5.8 |
| Stock with Swirl Enhancement | 30 | 26.5 | 21.5 | 24 | 45.5 | 3.8 |

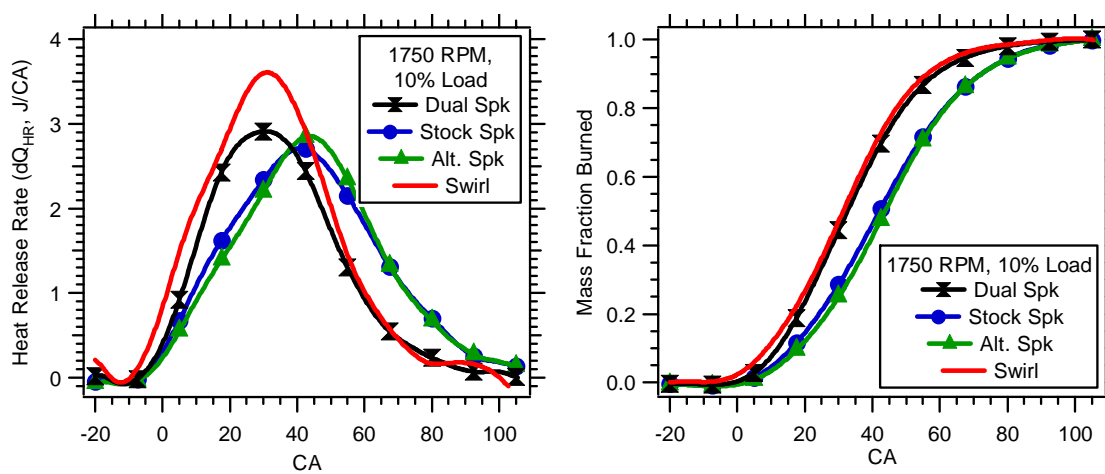


Figure 5.6.1: Variation of Heat Release with Spark Position and Swirl for 1750 RPM, 10% Load

Table 5.6.2: Variation of Heat Release Parameters with Spark Position and Swirl for 1750 RPM, 25% Load

| Spark Position | CA50 | CAIgn-10 | CA10-50 | CA50-90 | CA10-90 | COV % |
|------------------------------|------|----------|---------|---------|---------|-------|
| Stock | 27 | 27 | 18 | 22 | 40 | 3.2 |
| Alternate | 26 | 27 | 17 | 17 | 34 | 3.8 |
| Dual Spark | 16 | 21 | 13 | 17.5 | 30.5 | 3.2 |
| Stock with Swirl Enhancement | 18 | 20.5 | 15.5 | 19 | 34.5 | 1.6 |

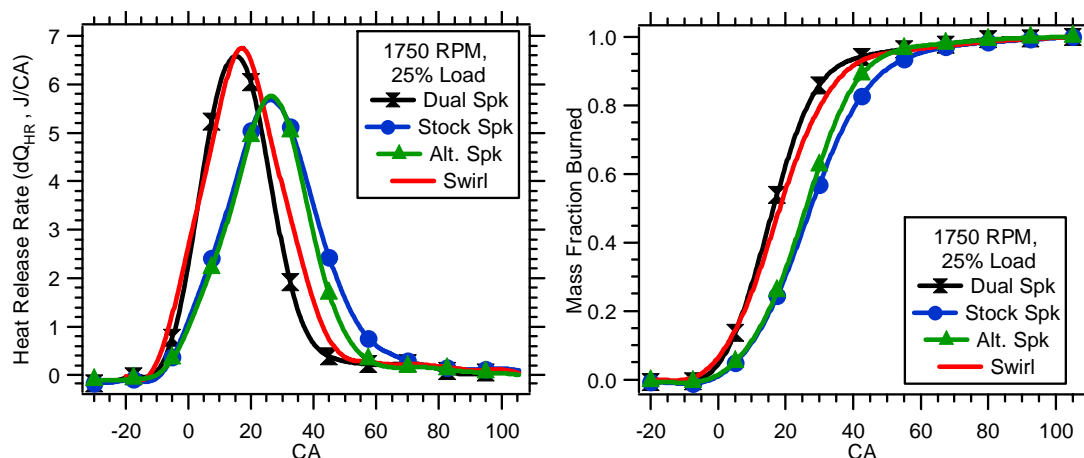


Figure 5.6.2: Variation of Heat Release with Spark Position and Swirl for 1750 RPM, 25% Load

Table 5.6.3: Variation of Heat Release Parameters with Spark Position and Swirl for 3060 RPM, 10% Load

| Spark Position | CA50 | CAIgn-10 | CA10-50 | CA50-90 | CA10-90 | COV % |
|------------------------------|------|----------|---------|---------|---------|-------|
| Stock | 44 | 32 | 30 | 32 | 62 | 9.8 |
| Alternate | 45 | 34 | 29 | 29 | 58 | 10.9 |
| Dual Spark | 32 | 28 | 22 | 24 | 46 | 4.9 |
| Stock with Swirl Enhancement | 31.5 | 28 | 21.5 | 23.5 | 45 | 3.8 |

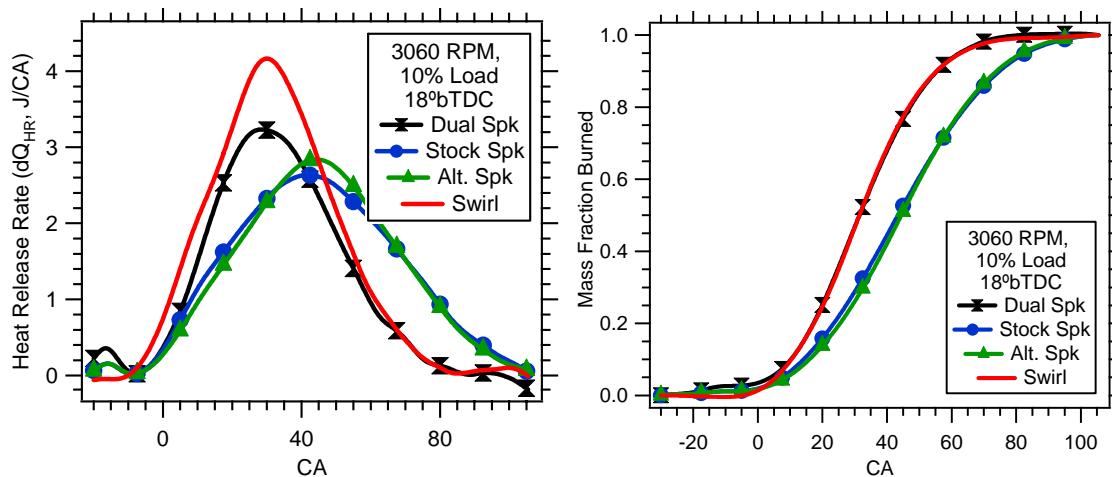


Figure 5.6.3: Variation of Heat Release with Spark Position and Swirl for 3060 RPM, 10% Load

Table 5.6.4: Variation of Heat Release Parameters with Spark Position and Swirl for 3060 RPM, 25% Load

| Spark Position | CA50 | CAIgn-10 | CA10-50 | CA50-90 | CA10-90 | COV % |
|------------------------------|------|----------|---------|---------|---------|-------|
| Stock | 34 | 29 | 23 | 23 | 46 | 9.8 |
| Alternate | 32 | 30 | 20 | 22 | 42 | 10.9 |
| Dual Spark | 23 | 24.5 | 16.5 | 19 | 35.5 | 4.9 |
| Stock with Swirl Enhancement | 22 | 23 | 17 | 20.5 | 37.5 | 3.8 |

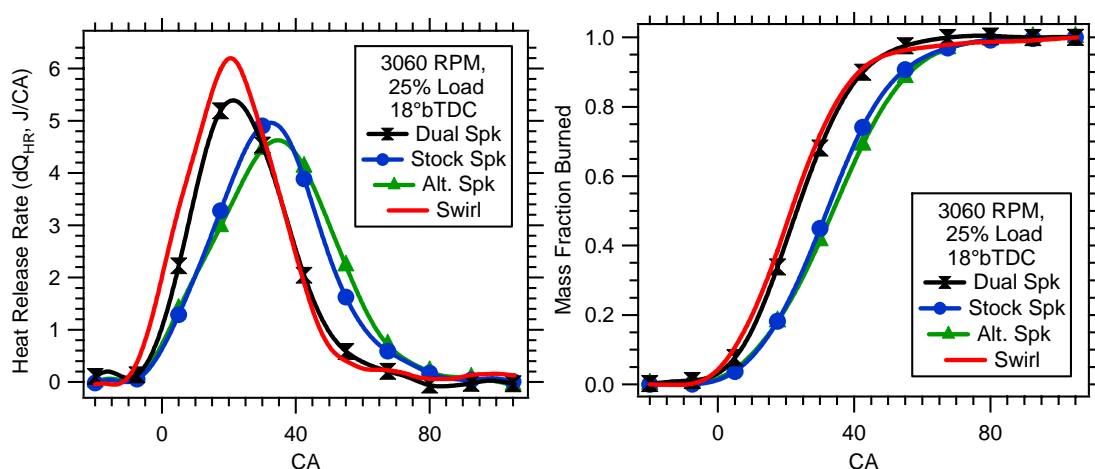


Figure 5.6.4: Variation of Heat Release with Spark Position and Swirl for 3060 RPM, 25% Load

The main impact of improving the flow field was advanced combustion for equivalent spark timing. The advantage of the swirl-enhanced conditions occurs early in the cycle with nearly a 5-7°CA advance of the CAIgn-10 and CA10-50 early flame propagation phases for all speeds and loads.

5.6.2 Emissions Response from Swirl-Enhanced Conditions

The 1750 RPM, 25% load condition was further investigated through a spark sweep to determine the impact of combustion phasing on emissions for the swirl-enhanced flow

field. Note that these data are compared to a spark sweep taken with the new engine block (see section 5.5).

5.6.2.1 HC Emissions Response with Swirl-Enhancement

The HC emissions from the high-swirl condition follow similar trends of a decreasing EIHC response with retarded spark timing (see Fig. 5.6.5).

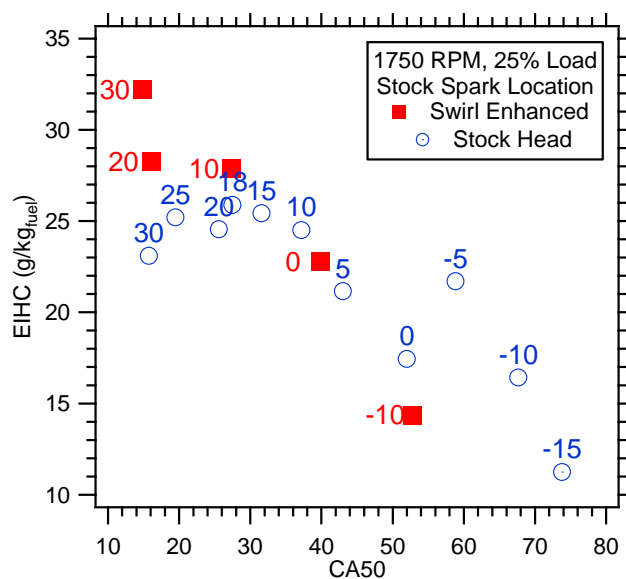


Figure 5.6.5: EIHC Response with Swirl Enhancement

On a mass basis the swirl-enhanced condition again follows the stock configuration trends (see Fig. 5.6.6)

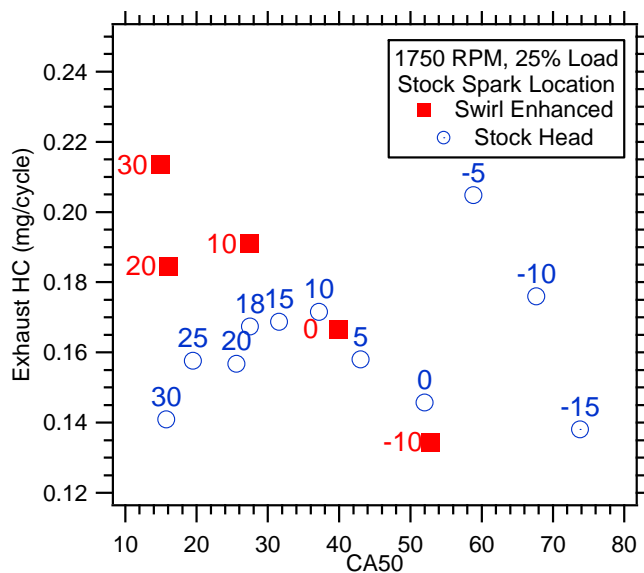


Figure 5.6.6 Mass-based HC Response with Swirl Enhancement

For a constant CA50, the swirl condition provides similar HC emissions, but comparing constant spark timing, the stock condition has lower HC emissions on a mass basis. This result is likely due to higher ring pack loading with the advanced combustion of the swirl-enhanced conditions.

5.6.2.2 NO_x Emissions Response with Swirl Enhancement

The NO_x emissions were found to increase with the swirl enhanced conditions (see Fig. 5.6.7) at a constant spark time.

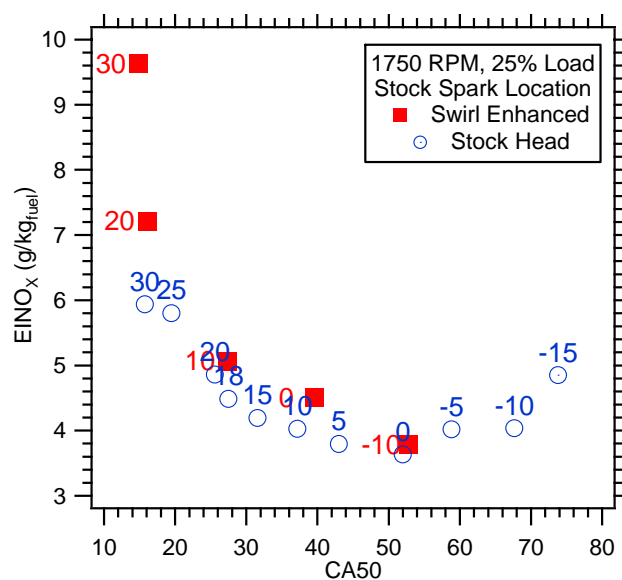


Figure 5.6.7: EINO_x Response with Swirl Enhancement

This can be attributed to the higher pressures and temperatures generated by the advanced combustion for a given spark timing relative to the stock spark condition. When combustion phasing is matched between the swirl-enhanced conditions and the stock head, a similar NO_x response can be obtained.

5.6.2.3 O₂ Emissions Response with Swirl Enhancement

The exhaust O₂ emissions concentration was found to decrease significantly with the introduction of swirl in the flow field (see Fig. 5.6.8).

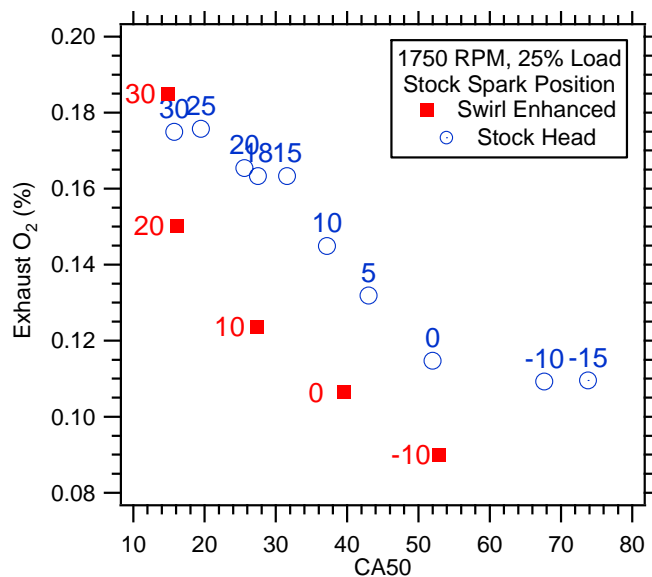


Figure 5.6.8: O₂ Response with Swirl Enhancement

5.6.3 COV with Swirl Enhancement

The COV was significantly reduced with the swirl-enhanced case (see Fig. 5.6.9) as expected from the shorter burn duration.

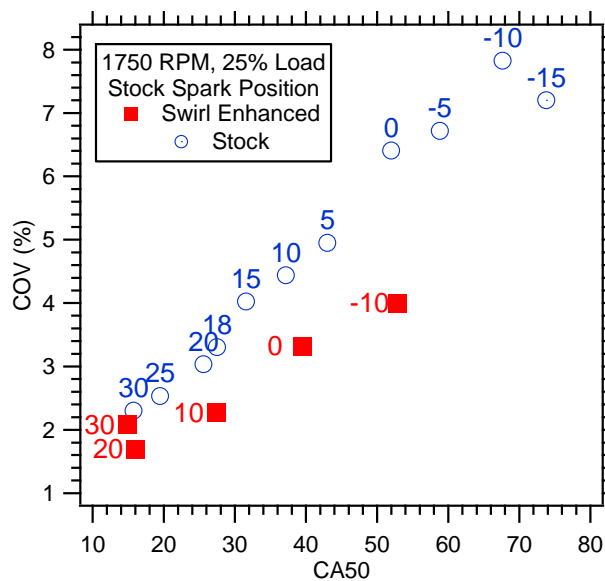


Figure 5.6.9: COV Response with Swirl Enhancement

The “ordered” flow pattern of the swirl-enhanced condition provides the combustion event with a more consistent, repeatable flow pattern rather than the random flow field of the stock condition.

5.6.4 Combustion Duration with Swirl Enhancement

Combustion duration improved significantly from the stock conditions (see Fig. 5.6.10).

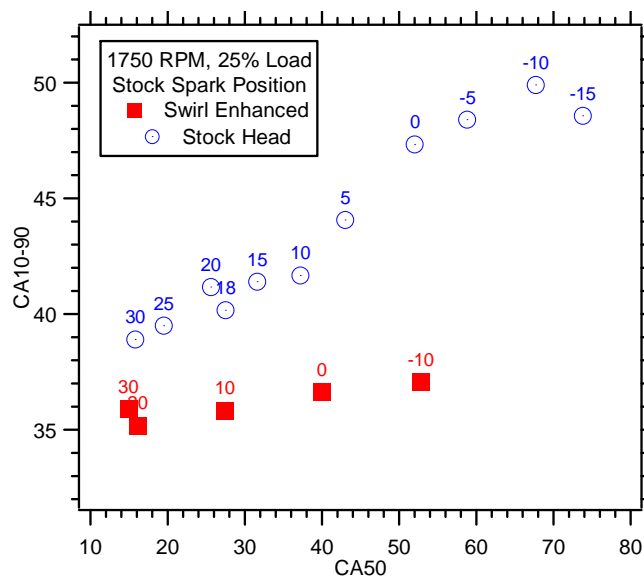


Figure 5.6.10: Combustion Duration Response with Swirl Enhancement

This is a clear indication that the flow field has a significant influence on the whole combustion process, not just the ignition and early kernel growth phase.

5.6.5 AF Ratio Exploration with Swirl Enhancement

Prior studies of swirl-enhanced conditions have found the ability to extend the lean combustion limit [42, 44]. The small, air-cooled engine combustion regime operates within the rich region; the ability to move into “leaner” conditions is limited by reduced fuel-cooling along the cylinder wall, decreased combustion stability and a increase in combustion duration.

The swirl enhancement improves both COV and combustion duration as indicated in Figs. 5.6.9 and Fig. 5.6.10.

An AF ratio sweep was conducted with constant CA50 to determine the influence of the AF ratio on burn duration (see Fig. 5.6.11).

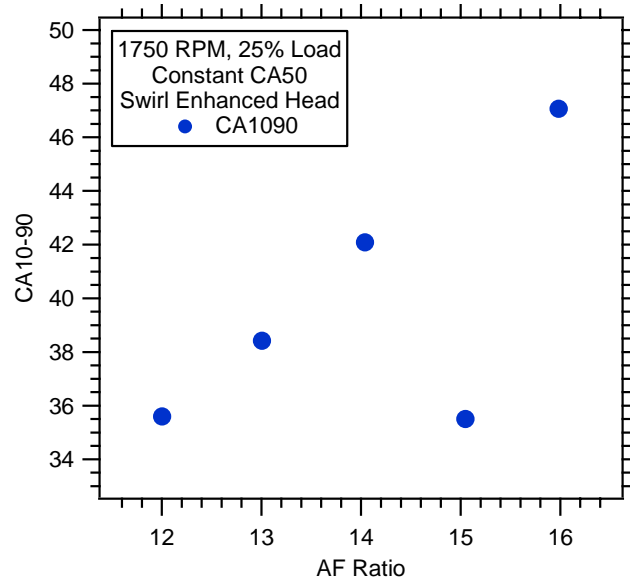


Figure 5.6.11: Combustion Duration Response with Varying AF Ratio

Fuel-lean conditions provide lower HC emissions, but an increase in NO_x emissions. The result is overall in an increase in the HC+NO_x parameter (see Fig. 5.6.12).

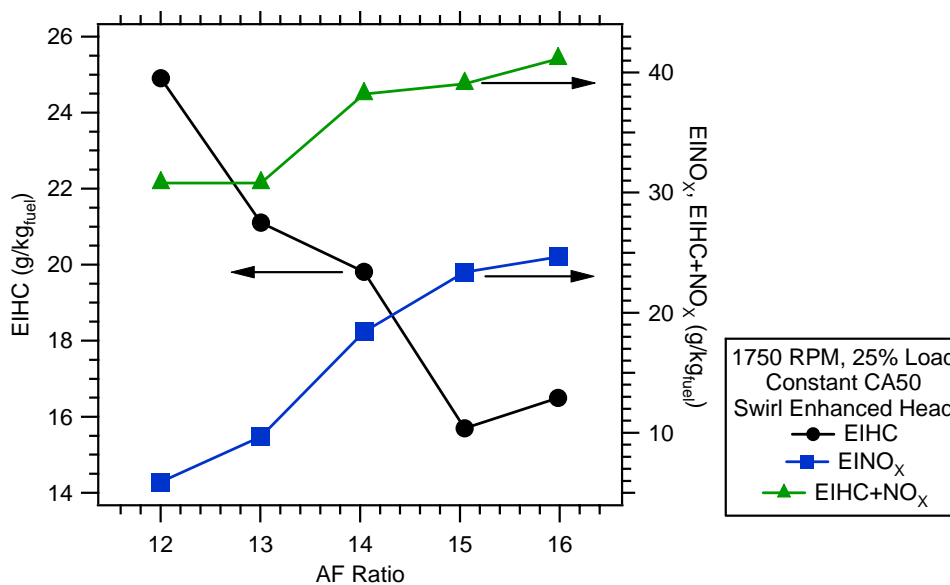


Figure 5.6.12: EIHC, EINO_x, EIHC+NO_x Response with Varying AF Ratio

It was determined that the engine could safely be operated at AF 16 lean condition therefore a further study with retarded spark timing at this AF ratio was conducted.

5.6.6 Lean, Retarded Combustion Phasing with Swirl Enhancement

As with earlier trends, retarded spark timing yields an increased burn duration independent of AF ratio and flow field (see Fig. 5.6.13).

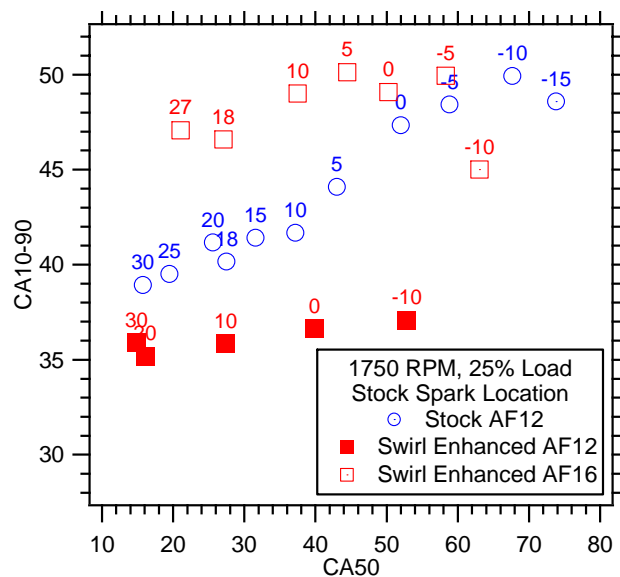


Figure 5.6.13: Comparison of Stock and Swirl Enhanced Conditions of Varying Combustion Phasing and AF Ratio

The swirl-enhanced conditions have a lower slope than the stock conditions with retarded combustion phasing indicating a weaker dependence of phasing to burn duration independent of AF ratio.

5.6.6.1 HC Response with Lean, Retarded Combustion Phasing and Swirl Enhancement

Fuel-lean mixtures have a lower concentration of fuel therefore the HC emissions are significantly lower than rich conditions (see Fig. 5.6.14). In addition, the presence of O₂ in the produces aids in the post-oxidation process. In Fig. 5.6.14, it can be seen that the retarded AF16 conditions provide HC emissions of around 2 g/kg.

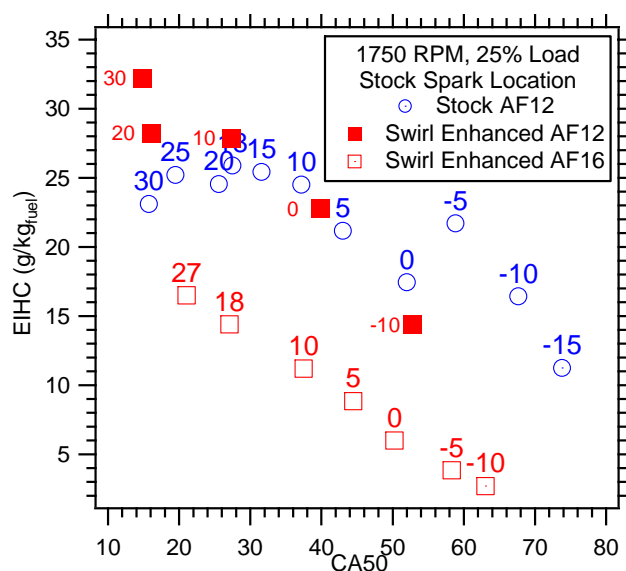


Figure 5.6.14: EIHC Response with Lean, Retarded Combustion Phasing and Swirl Enhancement

A similar trend is found with the mass-based emissions (see Fig. 5.6.15), where the retarded conditions give HC emissions of 0.02 mg/cycle.

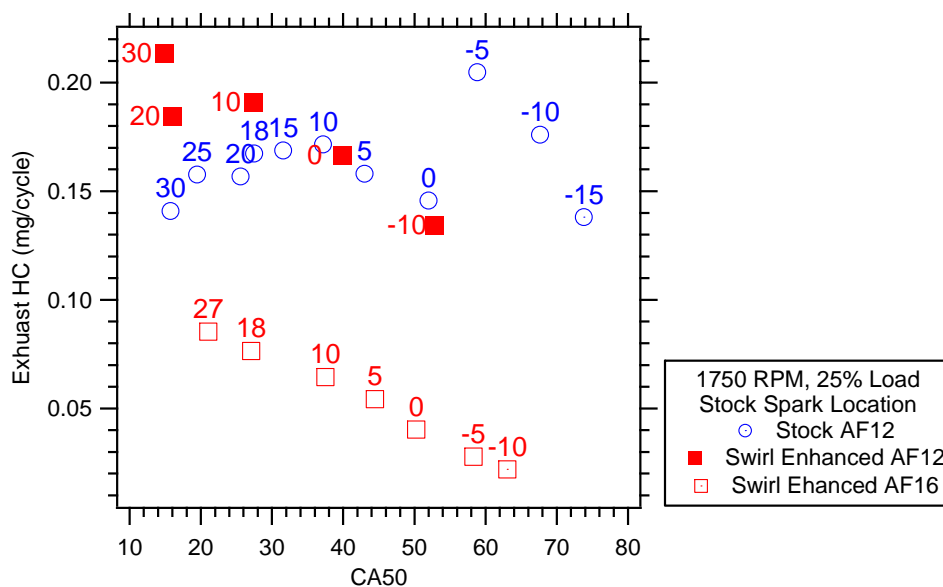


Figure 5.6.15: Mass-Based HC Response due to Lean, Retarded Combustion Phasing and Swirl Enhancement

The potential ring-pack contribution follows a similar trend for all conditions (see Fig. 5.6.16).

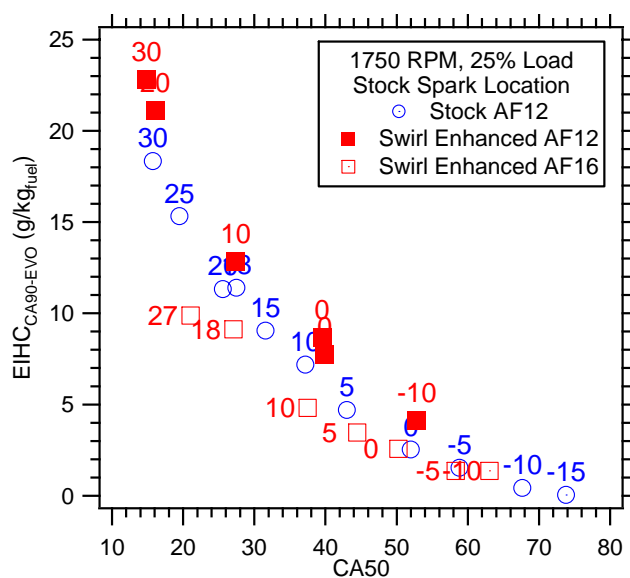


Figure 5.6.16: EIHC_{CA90-EVO} Emissions Response Due to Lean Combustion Phasing and Swirl Enhancement

Note that the detrimental influences from the improved flow field the resulted in a higher ring pack loading can be compensated by leaning the combustion mixture. This allows the improved burn duration to be retained by swirl enhancement with nearly identical combustion phasing.

5.6.6.2 NO_x Response with Lean Retarded Combustion Phasing and Swirl Enhancement

The EINO_x increased significantly from the rich AF conditions, but still decreased with retarded combustion phasing (see Fig. 5.6.17).

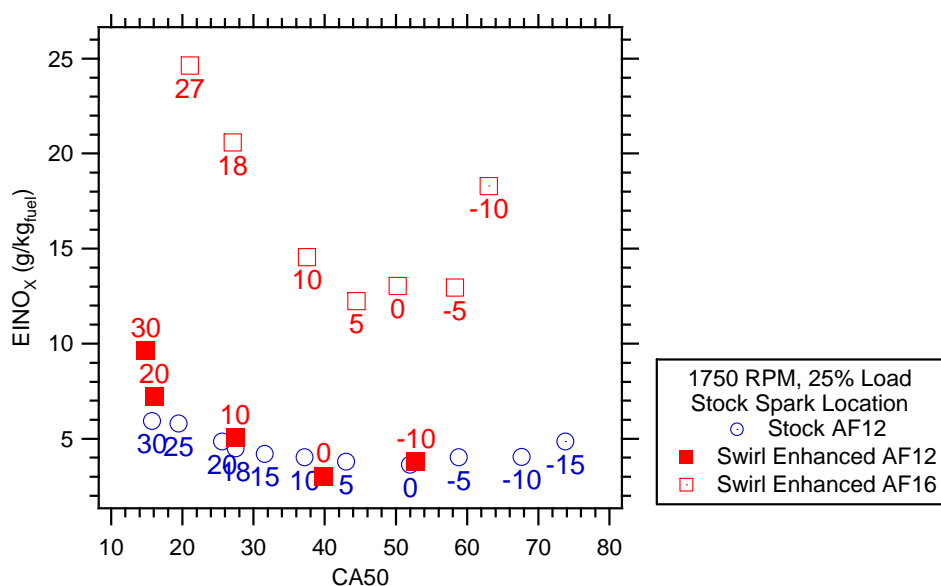


Figure 5.6.17: EINO_x Response with Lean, Retarded Combustion Phasing with Swirl Enhancement

The increased NO_x emission significantly impacts the overall HC+NO_x emissions; all other conditions have been dominated by the HC term, but now NO_x dominates. Thankfully, the reduction in HC is enough to balance the increase in NO_x resulting in little change in emission from the stock condition (see Fig. 5.6.18).

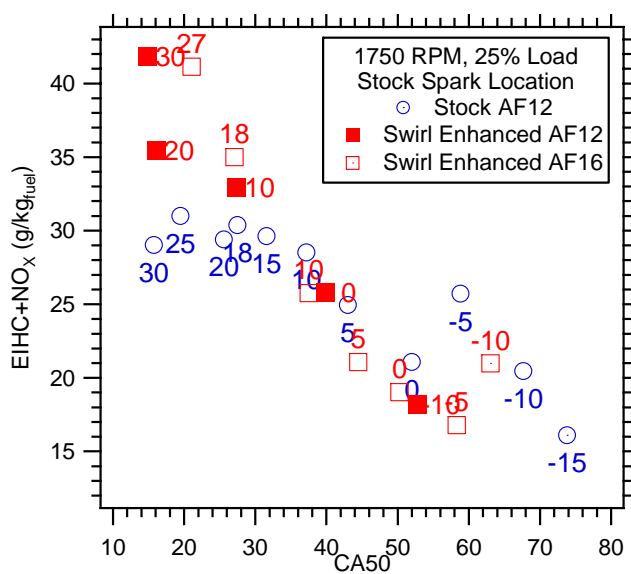


Figure 5.6.18: EIHC+NO_x Response with Lean, Retarded Combustion Phasing and Swirl Enhancement

5.6.6.3 O₂ Response with Lean, Retarded Combustion Phasing and Swirl Enhancement

The lean AF ratio results in a significantly higher exhaust O₂ emission. This increased oxygen content could provide a pathway for further HC post-oxidation with retarded combustion phasing. As with earlier tests, O₂ linearly decreases with combustion phasing retard (see Fig. 5.6.19).

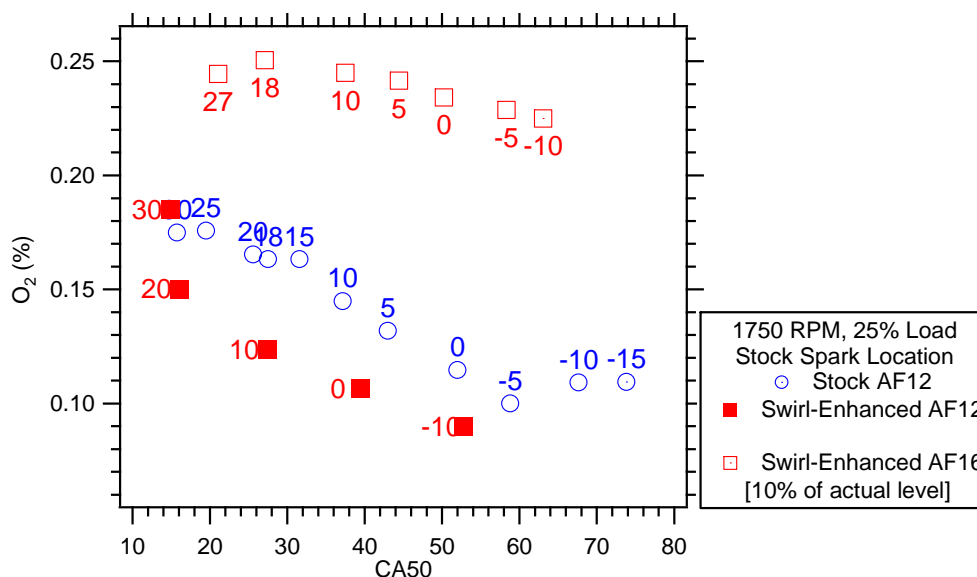


Figure 5.6.19: O₂ Response Due to Lean, Retarded Combustion Phasing and Swirl Enhancement

5.7 Combustion Similarity

In order to assess if one design or characteristic alleviates the slow combustion at light-load conditions, a similar condition between various engines was defined to allow for direct comparison. As outlined in section 2.8, mean piston speed, engine load as described by IMEP and combustion phasing define a similar combustion regime to a first order approximation.

5.7.1 Condition Definition

Table 5.7.1 defines the desired operating characteristics used for this study.

Table 5.7.1: Similar Operating Condition Definitions

| | |
|--------------------------|----------|
| Mean Piston Speed | 3.71 m/s |
| IMEP | 314 kPa |
| CA50 | 27°aTDC |

These parameters were selected from a common condition of the Kohler engine. Mean piston speed relates engine speed to engine geometry (refer to eqn. 2.8.3). By selecting a common piston speed among the engines, crankshaft speeds will vary inversely with stroke length. The IMEP, as defined by eqn. 2.8.2 over the full cycle, describes an engine load independent of engine geometry. An equivalent load between engines also provides a relationship to air and fuel rates that scales with engine size. Selection of a constant combustion phasing between engines presents the cylinder with a similar pressure field at a similar CA independent of engine geometry. Differences in heat release then reflect the geometry differences due to various port, valve and combustion chamber designs.

5.7.2 Engine Description

Various engines at the ERC and from the Wisconsin Small Engine Consortium member companies were tested at the similarity condition as defined by Table 5.7.1. It must be noted these engines are not scaled and do not follow a strict geometrically similar constraint; this study utilized stock production engines at a similar operating condition. Table 5.7.2 presents various geometry and operating variables of the engines tested.

Table 5.7.2: Engine Geometry and Speed

| Engine: | RPM | B/S | Disp. [cc] | Compression Ratio | Numb. Of Intake Valves | Chamber Geometry |
|-----------------|------|------|------------|-------------------|------------------------|--------------------------------------|
| Briggs | 2270 | 1.32 | 190 | 8 | 1 | Bathtub, side spark location |
| Kohler | 1750 | 1.2 | 337 | 8.15 | 1 | Shallow Bathtub, side spark location |
| Mercury Marine | 1355 | 1 | 433 | 8.37 | 2 | Pent-roof, side spark location |
| GM | 1240 | 0.91 | 550 | 10.95 | 2 | Pent-roof, center spark location |
| Harley Davidson | 1000 | 0.86 | 792 | 9.2 | 1 | Deep-Bathtub, center spark location |

5.7.3 Similar Condition Heat Release Results

The pressure traces of the various engines follow a remarkably similar path providing confidence in the condition definition (see Fig. 5.7.1).

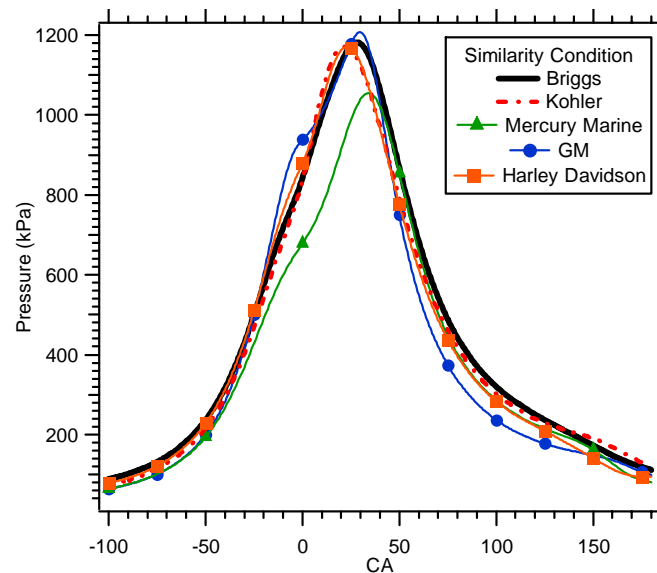


Figure 5.7.1: In-Cylinder Pressure Response of the Engines at the Similarity Condition

The heat release rate, as indicated in Fig. 5.7.2, follows similar paths but vary in magnitude due to differences in fuel mass.

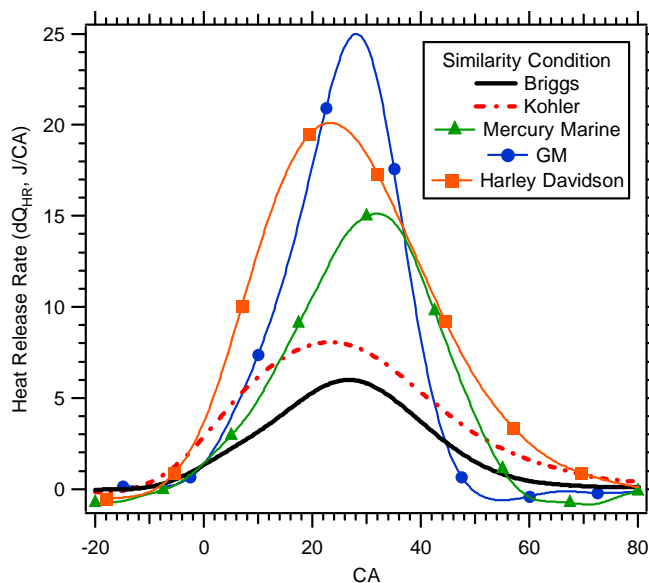


Figure 5.7.2: Heat Release Rate of the Engines at the Similarity Condition

The mass fraction burned allows a better comparison of this condition as the curve is normalized by the energy released from the fuel (see Figure 5.7.3).

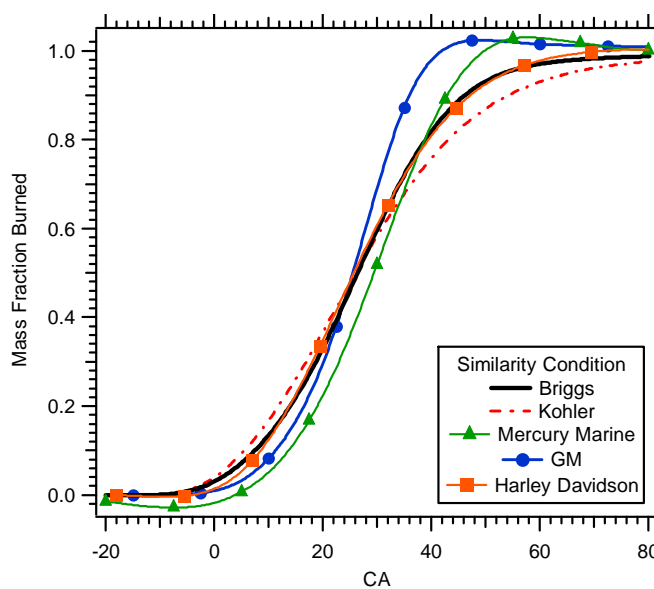


Figure 5.7.3: Mass Fraction Burned Curve of the Engines at the Similarity Condition

Differentiating the MFB curve presents a curve similar to the HRR, but without the fuel effects (see Fig. 5.7.4).

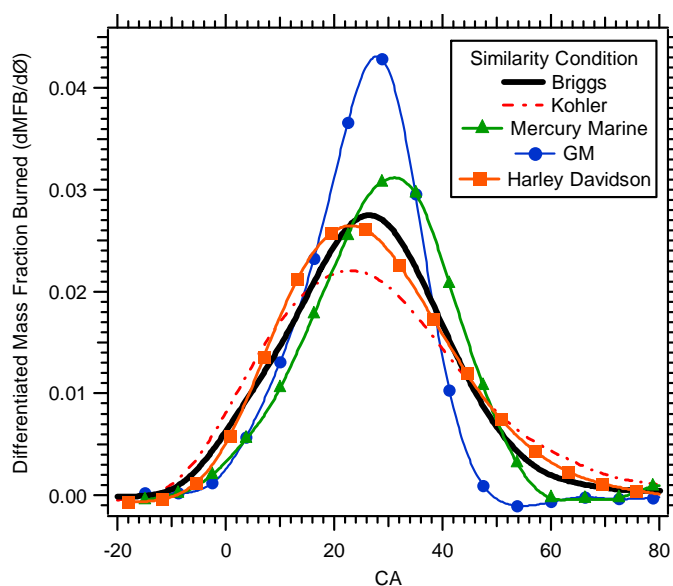


Figure 5.7.4: Differentiated Mass Fraction Burned Curve of the Engines at the Similarity Condition

This differentiated MFB curve describes the rate of change of the curve and is independent of all fueling differences; the effect of various engine designs on burn duration is now clearly indicated. Note the magnitude change later in the cycle for the GM and Mercury Marine engine. The initial periods of heat release are surprisingly similar, yet the GM and Mercury Marine engines maintain a larger rate of change (i.e. burning faster) later in the cycle. Interestingly, the lower B/S ratio engines do not necessarily yield the best burn duration (see Table 5.7.3).

Table 5.7.3: MFB Parameter Comparison of Various Engines at the Similarity Condition

| Engine | B/S Ratio | Ign. Timing (°bTDC) | CA50 | CAIgn-10 | CA10-50 | CA50-90 | CA10-90 |
|-----------------|-----------|---------------------|------|----------|---------|---------|---------|
| Briggs | 1.32 | 18 | 26 | 25.5 | 18.75 | 19.75 | 38.5 |
| Kohler | 1.19 | 22 | 24 | 27 | 18.25 | 19 | 37.25 |
| Mercury Marine | 1 | 13 | 29 | 25 | 17.25 | 15.75 | 33 |
| GM | 0.91 | 10 | 26 | 21.25 | 14.25 | 10.25 | 24.5 |
| Harley Davidson | 0.86 | 17 | 26 | 25.5 | 17 | 21.5 | 38.5 |

The GM engine presents the lowest burn duration, while the Harley, Kohler and Briggs have longer burn durations, by almost 15°CA. It is interesting to note that the GM engine has a CAIgn-10 duration four degrees shorter than the other engines. Since this early regime is sensitive to changes in the flow field, a general conclusion is that the GM head design provides a favorable flow pattern at the time of ignition. Prior studies [50,57] have found that the early flame propagation period (CAIgn-10 and CA10-50) and flame speed can be influenced by the compression ratio (refer to eqn. 2.8.5). All of the engines except the GM engine have compression ratios in the 8-9 range while the GM compression ratio is 11 therefore the early flame propagation data may be biased.

The shorter CA50-90 durations of the Mercury Marine and GM engine could possibly be attributed to improved heat transfer through the water cooling rather than the air cooling packages of the other engines. Also these engines may present greater intake momentum providing for favorable late cycle flow fields and improved CA50-90 durations.

5.7.4 Similar Condition Conclusions

Operating engines of various sizes at the same condition (e.g. same RPM, load, spark timing, etc.) will obscure the dominant contributions to the heat release rate. A similarity condition can be easily created across various engines if mean piston speed, IMEP and combustion phasing are held constant. Following these basic parameters, the pressure response of various engines was found to be similar resulting in similar heat release rates. Differentiating the MFB curve can provide further insight into similar operating conditions without the influence of fueling effects.

By changing engines, it was expected that a significant change in burn duration would occur as the turbulence intensity would vary based on intake and combustion chamber geometry. Since the mean piston speed was held constant across the engines, changing designs would represent a change in slope of the turbulence intensity plot (refer to Fig. 2.7.3).

The engines provided by the member companies and those located at the ERC represent a wide range of combustion chamber and port designs, yet nearly all of them have similar initial flame propagation periods (CAIgn-10, CA10-50), but differ significantly in the flame termination periods (CA50-90). It was shown in section 5.6.6 that flow field effects can be still prevalent late in the cycle effecting burn duration (highly retarded combustion phasing is still significantly improved over the stock condition). Although both the GM and Mercury Marine engines are water cooled, the pent-roof combustion chamber may allow for a greater intake momentum lasting later in the cycle improving CA50-90 and ultimately burn duration.

6.0 Discussion

6.1 Heat Release Rate Improvement

Various methods to improve heat release rate in small engines have been investigated in this study, and in previous investigations. This study focused on dual spark configurations, alternate spark locations and bulk flow improvement, where previous work focused on valve overlap. There are minor differences in stroke length between the engines used in the valve overlap study and the present engine that must be taken into consideration, but this data set can provide a tool to determine which burn rate strategy can be utilized to provide the largest improvement.

The effect of valve overlap on light-load engine performance was investigated by Albert and Haugle on a similar Briggs Intek engine through a special, split-lobe cam system capable of varying valve open durations [1, 2]. Three conditions were investigated in this study: 0°, 95° and 128° (maximum) CA overlap. Comparing that dataset to the stock condition of 50°CA valve overlap, a relative percent difference can be determined. A similar procedure to determine the relative percent difference was conducted with the alternate spark position conditions, dual spark conditions and the swirl enhanced head configuration to allow a comparison between all of the datasets. All changes are relative to their respective stock configurations and timings. Note that positive relative percent changes are a favorable change (i.e. decreased CA1090, advancing CA50, and decreased COV) and a negative relative percent change represents an unfavorable change (i.e. increased CA1090, retarding CA50, and increased COV).

6.1.1 Burn Duration Comparison

A comparison of the various configurations effect on CA10-90 is shown in Fig. 6.1.1.

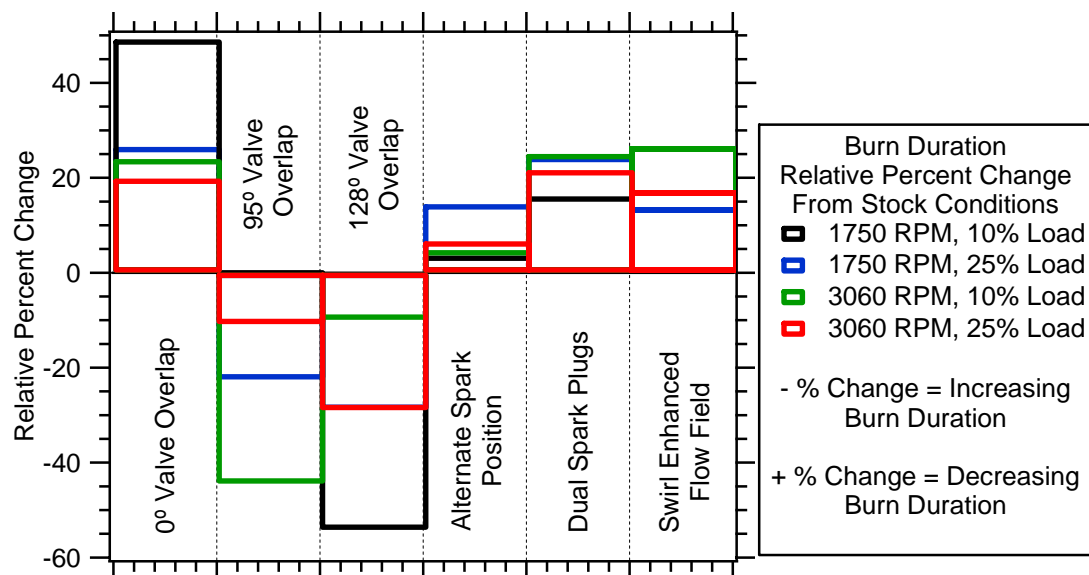


Figure 6.1.1: Burn Duration Comparison of Various Techniques to Modify Light-Load Heat Release Rate

Whereas the zero degree valve overlap significantly improves 1750 RPM, 10% load condition, the effect diminishes with increasing speed and load. Dual spark and swirl-enhanced conditions provide consistent improvements to the burn duration relatively independent of speed and load, and are comparable in their level of improvement

6.1.2 Combustion Phasing Comparison

Early combustion phasing positions combustion in a favorable pressure field to allow for maximum work extraction. Figure 6.1.2 represents the change in CA50 across the various configurations.

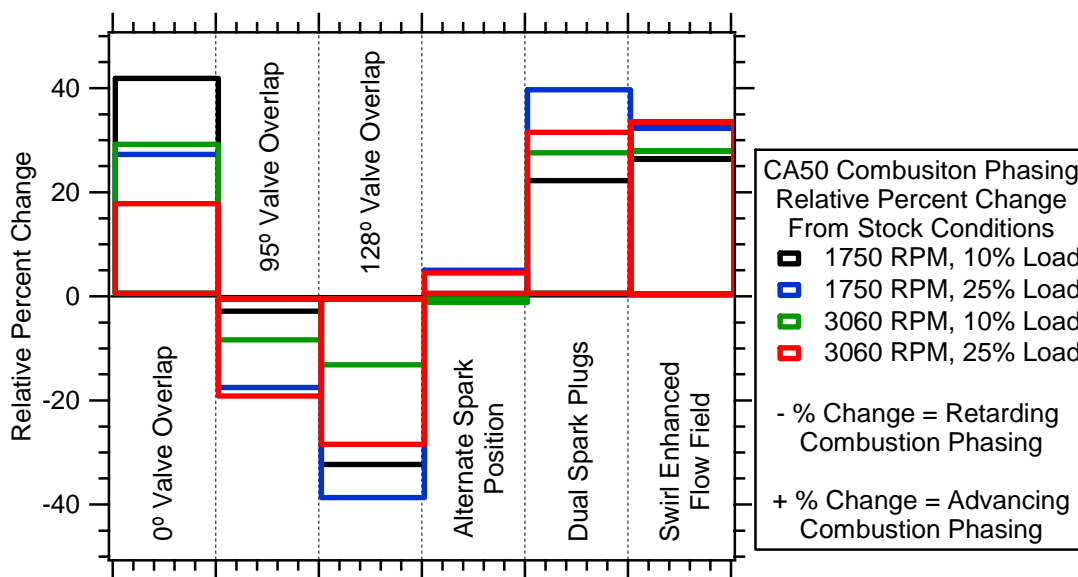


Figure 6.1.2: Combustion Phasing Comparison of Various Techniques to Modify Light-Load Heat Release Rate

The zero valve overlap, dual spark and swirl-enhanced flow field all resulted in nearly comparable advancement of combustion phasing.

6.1.3 COV Comparison

Figure 6.1.3 presents the percent change of COV between the various configurations.

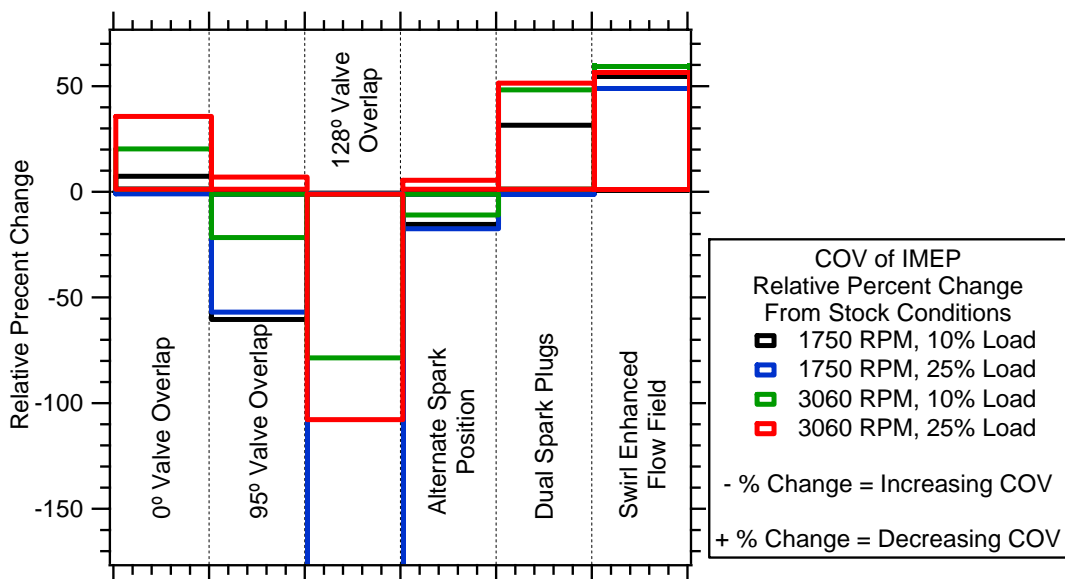


Figure 6.1.3: COV Comparison of Various Techniques to Modify Light-Load Heat Release Rate

The increased valve overlap changes the internal residual retention therefore adversely affect COV; reduction of the trapped residual through zero valve overlap improves COV. The swirl-enhanced condition provides a consistent improvement independent of speed and load.

6.1.4 Relative Heat Release Rate Improvements Conclusions

Through investigation of the relative percent change from the stock condition, the efficacy of various techniques to increase heat release rate is possible from two different studies. The swirl-enhanced flow field through a tangential port blockage consistently provided a favorable change in burn duration, combustion phasing and COV, nearly independent of speed and load. The reduction of residual fraction through low valve overlap also had beneficial effects, but they diminished at higher speeds and loads.

6.2 Bulk Flow Description

During the steady flow experimentation portion of this study, significant questions as to the definition of various steady flow parameters arose; specifically the flow and global swirl ratio. Various references were found to describe the flow coefficient as the measured flow rate over the ideal flow rate defined by an isentropic nozzle of a given area, but the area would vary. The inner valve seat area was the most common [37,38], but the inner valve seat area minus the stem area, and a varying minimum flow area based on valve lift were also referenced [34]. Compressible flow through a pipe dictates the reference area to determine mass flow rates should be the minimum area of the geometry. The selection of area greatly affects the overall solution of the flow coefficient and global swirl ratio (refer to eqn. 2.7.8).

To determine the effect of the selected area, a data set of the stock head configuration at WOT was analyzed with various reference areas (see Table 6.2.1); note the inside valve seat area was the reference area used for this study.

Table 6.2.1: Various Reference Areas for Flow Coefficient Calculation

| Reference Area | Equation |
|----------------------------------|--|
| Inside Valve Seat Area | $A_C = \frac{\pi}{4} D_{valve}^2$ |
| Corrected Inside Valve Seat Area | $A_C = \frac{\pi}{4} (D_{valve}^2 - D_{stem}^2)$ |
| Port Area | $A_C = \frac{\pi}{4} D_{port}^2$ |
| Corrected Port Area | $A_C = \frac{\pi}{4} (D_{port}^2 - D_{stem}^2)$ |
| Curtain Area | $A_C = \pi D_{valve} Lift$ |

Where D_{valve} is the inner valve seat diameter, D_{stem} is the diameter of the valve stem and D_{port} is the intake port diameter above the valve seat. The “corrected” area represents the subtraction of the area taken up by the valve stem in the port. Note that the curtain area varies based on valve lift. Figure 6.2.1 shows the various responses of the flow coefficient based on the reference area definition.

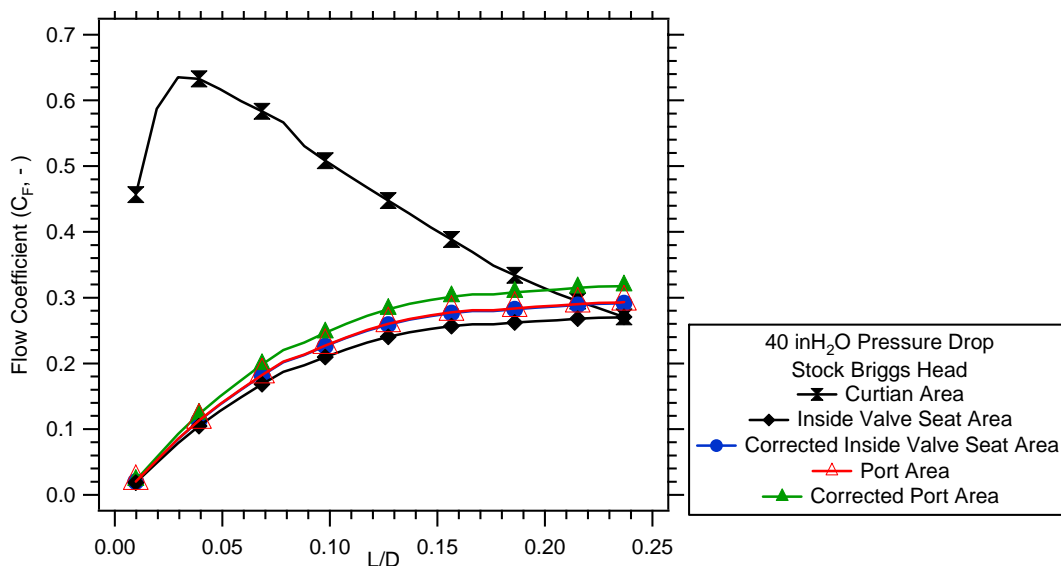


Figure 6.2.1: Flow Coefficient Response to Various Reference Areas from Table 5.6.1
 Minor changes in the flow coefficient, however, result in relatively large changes in the global swirl ratio (see Table 6.2.2).

Table 6.2.2: Various Area Values and Corresponding Global Swirl Ratio Values

| Reference Area | Area (mm ²) | Area % Diff. | Global Swirl Ratio | Global Swirl Ratio % Diff. |
|----------------------------------|-------------------------|--------------|--------------------|----------------------------|
| Inside Valve Seat Area | 476 | - | -0.40 | - |
| Corrected Inside Valve Seat Area | 441 | 7.4 | -0.37 | 7.2 |
| Port Area | 439 | 7.8 | -0.37 | 7.7 |
| Corrected Port Area | 405 | 14.9 | -0.34 | 15.8 |
| Curtain Area | Varies | Varies | -0.09 | 77.3 |

This example is provided to show the importance of clear definition of the intake geometry and its effect on other parameters. Since the tangential port blockage minimizes the area in the port downstream of the intake runner, the minimum area may have shifted. Care must be taken when measuring and reporting steady flow data.

7.0 Conclusions and Recommendations

7.1 Overview

This project investigated methods to improve light-load, low-speed burn rate in a air-cooled utility engine. Combustion and steady flow experimentation allowed for heat release analysis and a basic, global view of the flow field for various swirl-enhancing techniques. Emissions reduction through retarded spark timing was investigated for various spark positions and intake geometries. A similarity condition was developed to benchmark engines of various geometries at a light-load operating point to determine if a simple geometric feature could be utilized from established engine designs to improve burn rate. Pressure data collected from WSEC member companies and engines at the ERC provided a catalogue of various engine geometries and sizes at a similar operating point for performance and heat release comparison.

7.2 Summary of Results

Simple methods have been found to improve the burn duration of a small utility engine through various techniques. The main objective of any technique is to reduce CA10-90, but also place CA50 at a favorable position. Dual spark conditions effectively improved CA10-90 by advancing combustion around 7°CA depending on speed and load. The advantage of multiple flame fronts decreased as the kernels coalesced into one propagating flame front. Spark location was found to significantly impact heat release rate and emissions. At a comparable CA50 phasing, dual spark emissions levels were comparable to single spark conditions, and had a lower burn duration.

The HC emissions were found to dominate in the light-load, low-speed operating regime, therefore a retarded spark timing strategy was employed to reduce ring pack loading and to improve post-oxidation. Retarding combustion phasing reduces peak pressure, reducing ring-pack loading, and increases exhaust gas temperature allowing for an improved environment for HC post-oxidation. The trends that were found on a mass-basis, which were hidden by the normalization with the fueling rate on an EI basis, indicated a maximum possible level of HC post-oxidation for a given condition. The influence of O₂ concentration suggests a minimum level for post-oxidation kinetics. Spark position was found to be a significant factor in mass-based HC emissions.

Steady flow experiments provided a global view of the intake flow through non-dimensional parameters. The flow coefficient and swirl coefficient described the mass flow and angular momentum of the flow for various port configurations. Partial throttle and WOT tests were conducted yielding significantly different results of mass flow and angular momentum. Since this study focused on light-load conditions, the partial throttle tests were highlighted as a more probable in-cylinder flow pattern during the combustion tests. A tradeoff exists between flow rate and the pressure drop experienced by any blockage created to improve the momentum of the flow field, therefore high swirl configurations provided lower mass flow rates in comparison to the baseline geometry. It was found that flow modification had to be implemented as close to the valve face as possible to provide the greatest effect (swirl). Upstream modifications had less of an effect, probably due to the relatively undirected flow in the port. Blockages, rather than directed vanes in the port were found to yield the highest global swirl. A tangential port blockage was found to yield the

highest global swirl ratio of 2.6 under partial throttle conditions, and was selected for combustion tests.

The head with the tangential port blockage was compared across all conditions at stock spark timing and was found to significantly improve light-load, low-speed heat release. Combustion phasing advanced 10°CA and burn duration decreased by $7\text{-}10^{\circ}\text{CA}$ depending on the condition in comparison to the stock spark configuration. Further investigation into the 1750 RPM, 25% load condition with retarded spark timing revealed a significant reduction in HC is possible. The swirl-enhanced configuration allowed lean conditions to be investigated without significant heat release past EVO. Conditions at an AF ratio of 16 with retarded spark timing provided the lowest HC emissions, but increased NO_x emissions. Although there was an HC and NO_x tradeoff, the $\text{HC}+\text{NO}_x$ parameter upon which small engines are regulated followed the same path as the stock AF12 retarded spark conditions.

A similar operating condition across various engine geometries was developed based on a constant mean piston speed, IMEP and CA50. Various engines from the WSEC member companies and at the ERC were tested at this condition and compared to determine a heat release comparison was made. The engines provided a significant range in size and intake geometry from simplistic port design to multivalve automotive port configurations. The GM engine, with two intake valves and a pent-roof chamber presented the lowest burn duration, while the Harley, Kohler and Briggs engines were the slowest to complete combustion. The greatest difference between the engines occurred during the initial and flame propagation phase (CAIgn-10 and CA10-50) in which the expanding kernel is sensitive to the flow field effects. Surprisingly, all of the member company engines were within $1\text{-}2^{\circ}\text{CA}$ for these phases. Although the main goal of this similarity condition was to isolate

flow field differences, which would result in early heat release differences, the later heat release phase, which is highly influential by heat transfer proved to be the greatest difference in the engines.

Overall, small engine light-load, low-speed burn rate can be significantly increased through swirl enhancement. The improved flow field decreases burn duration and can allow lean conditions to be run. By retarding ignition, a favorable HC post-oxidation environment can yield lower emissions across all conditions. A “burning fast, late and lean” combustion strategy can provide the small engine community a technique to meet emissions standards for the future.

7.3 Recommendations

During the experimentation for this project several questions arose as to the nature of HC post-oxidation, in-cylinder flow field improvement, and production engine comparison based on a similar operating condition.

Over the course of this project, the engine had to be replaced due to excessive wear leading to an ever-increasing HC response for a given condition. Before its replacement, all of the data leading up to section 5.5 was conducted on one engine. Due to its prolonged life, a significant layer of carbon build up along the top of the combustion chamber and piston face developed. To counteract this buildup effect, a high-speed, high-load condition was run at the end of each test day to try to “burn-out” any deposits. Disassembly of the old engine proved this technique still left a considerable layer of carbon buildup along the chamber surfaces. After the engine was rebuilt and the head cleaned, a retarded spark sweep at 1750 RPM, 25% load was conducted to assess differences between engines (see section 5.5). The

cleaned engine presented a significantly lower HC response as expected, but also a lower O₂ output. The trends, seen in Fig. 5.4.7, shows a minimum in mass-based HC levels at a given O₂ concentration. The new engine spark sweep provided O₂ levels below this previously defined concentration, yet still allowed for HC oxidation. The connection between combustion chamber deposits and O₂ levels is not explored in this study, but may yield an interesting kinetic pathway for HC oxidation if lean combustion is not attainable for air-cooled engines. This also brings into question what the smallest level of oxygen necessary for post-oxidation is, and if this level can be obtained in a rich-combustion regime.

The flow field modifications through port blockages and directional vanes were static, limiting WOT breathing capacity and performance. As the engine is designed for a WOT operating regime, the loss of volumetric efficiency significantly decreases the performance. A method to effectively move the blockages out of the way during WOT conditions would provide a complete solution for the small engine community. As shown in section 5.6, a tangential blockage, yielding a high swirl flow field, significantly improves the light load burn rate without the need of a relatively expensive secondary spark system, but due to the static nature of the blockage, the WOT torque was decreased by 20% due to decreased breathing capacity. A simple, cast-in port geometry enhancing a tangential flow into the engine would provide the ultimate solution to light-load burn rate problems, but may prove to be expensive.

Further exploration of a similar operating condition is suggested due to its ability to benchmark several engines of various designs at the same condition. The results were surprisingly close in the engine comparison, but this may be due to a variety of size effects. It was suggested that engines of large bore-to-stroke ratio provide a larger volume for a

constant crank angle flame kernel (refer to Fig. 2.8.6). These volume effects may be clouding the similarity condition due to the large variation in bore-to-stroke ratio across the tested engines. Strict scaling studies conducted by Staples [67] and Shi [68] suggest a stronger comparison between engines when the TDC environment in terms of temperature and pressure are scaled in diesel engines. Although dominated by flow field effects, this TDC environment scaling may provide a method to reduce compression ratio biases in the dataset.

The retarded spark timing provides a reliable method to decrease HC emissions, but the dependency on combustion chamber deposits represents an interesting question as to the oxidation chemistry occurring in this combustion regime. In-cylinder flow field modifications were found to be based off of relatively simple port geometries yet the issue of improving the motion without the loss of WOT performance is still elusive. Similarity conditions between engines presents a very useful tool if properly defined; the work from this thesis only presented a simplistic, first order approach to the technique.

References

1. Haugle, N.J., Master's Thesis, University of Wisconsin – Madison, 2006.
2. Albert, B.P., Master's Thesis, University of Wisconsin – Madison, 2004.
3. Salazar, V.S., PhD Thesis, University of Wisconsin – Madison, 2008.
4. Bottom, K.E., PhD Thesis, University of Wisconsin – Madison, 2003.
5. Rassweiler, G.M. and Withrow, L., "Motion Pictures of Engine Flames Correlated with Pressure Cards", SAE Journal, Vol. 42, No. 5, 1938.
6. Krieger, R.B., and Borman G.L. "The Computation of Apparent Heat release for Internal Combustion Engines", ASME paper 66 WA/DGP-4, 1966.
7. Gatowski, J.A., et. al., "Heat Release Analysis of Engine Pressure Data", SAE paper 841359, 1984.
8. Cheung, H. and Heywood, J.B., "Evaluation of a One-Zone Burn-Rate Analysis Procedure Using Production SI Engine Pressure Data", SAE paper 932749, 1993.
9. Lanzafame, R. and Messina, M., "ICE Gross Heat Release Strongly Influenced by Specific Heat Ratio Values", *International Journal of Automotive Technology*, Vol. 4, No. 3, pg124 – 133, 2003.
10. Poulos, S.G., and Heywood, J.B., "The Effect of Chamber Geometry on Spark-Ignition Engine Combustion", SAE paper 830334, 1983.
11. Yeliana, Y. et. al., "The Calculation of Mass Fraction Burned of Ethanol-Gasoline Blended Fuels Using Single and Two-Zone Model", SAE paper 2008-01-0320, 2008.
12. Brunt, M.F and Emtage, A.L., "Evaluation of Burn Rate Routines and Analysis Errors", SAE paper 970037, 1997.
13. Liou T.M et.al., "Laser Doppler Velocimetry Measurements in Valved and Ported Engines", SAE paper 840375, 1984.
14. Peters, B.D. and Borman, G.L., "Cyclic Variations and Average Burning Rates in a S.I. Engine", SAE paper 700064, 1970.
15. "Test Procedure for the Measurement of Gaseous Exhaust Emissions For Small Utility Engines", SAE Recommended Practice, SAE Paper J1088, Feb. 1993.
16. Douglas, R. and Glover, S., "The Feasibility of Meeting CARB/EPA 3 Emissions Regulations for Small Engines", SAE paper 2007-32-0059, 2007.
17. Mattavi, J.N., "The Attributes of Fast Burning Rates in Engines", SAE paper 800920, 1980.
18. Witze, P., "The Effect of Spark Location on Combustion in a Variable-Swirl Engine", SAE paper 820044, 1982.

19. Groff, E.G., and Sinnamon, J.F., "The Effects of Ignition Location in a Swirl Field on Homogeneous-Charge Combustion" SAE paper 821221, 1982.
20. Wentworth, J.T., "Effects of Combustion Chamber Shape and Spark Location on Exhaust Nitric Oxide and Hydrocarbon Emissions", SAE paper 740529, 1974.
21. Quader, A.A., "Effects of Spark Location and Combustion Duration on Nitric Oxide and Hydrocarbon Emissions", SAE paper 730153, 1973.
22. Salazar, V.M. and Ghandhi, J.B., "Ring Pack Crevices and Crankcase Pressure Effects on the Hydrocarbon Emissions from an Air-Cooled Utility Engine", SAE paper 2008-32-0004, 2008.
23. Ogawa, H., et.al., "Development of a Power Train for the Hybrid Automobile – the Civic Hybrid", SAE paper 2003-01-0083, 2003.
24. Ramtilak, A., et. al., "Digital Twin Spark Ignition for Improved Fuel Economy and Emissions on Four Stroke Engines", SAE paper 2005-26-008, 2005.
25. Chandra, H., "A Critical Study of the Dual Versus Single Plug Systems in S.I. Engines", SAE paper 940452, 1994.
26. Lauvergne, R., and Hallot, J., "Investigation of the Effect of Double Ignition on the Combustion Processes in a 2-valves Gasoline Engine Through 3D Simulation", SAE 2003-01-0010, 2003.
27. Hallgren, B.E., and Heywood, J.B., "Effects of Substantial Spark Retard on SI Engine Combustion and Hydrocarbon Emissions", SAE paper 2003-01-3237, 2003.
28. Eng, J.A., et. al., "Experimental Hydrocarbon Consumption Rate Correlations from a Spark Ignition Engine", SAE paper 972888, 1997.
29. Eng, J.A., "The Effect of Spark Retard on Engine-out Hydrocarbon Emissions", SAE paper 2005-01-3867, 2005.
30. S.R. Turns, *An Introduction to Combustion: Concepts and Applications*, McGraw-Hill, Inc., ISBN 0-07-230096-5, 2000.
31. Lee, D., and Heywood, J.B., "Effects of Charge Motion Control during Cold Start of SI Engines", SAE paper 2006-01-3399, 2006.
32. Lee, D.W., "A Study of Air Flow in an Engine Cylinder", NACA TM Report No. 653, 1938.
33. Davis, G.C., and Kent, J.C., "Comparison of Model Calculations and Experimental Measurements of the Bulk Cylinder Flow Processes in a Motored PROCOC Engine", SAE paper 790290, 1979.
34. Heywood, J.B., *Internal Combustion Engine Fundamentals*, McGraw-Hill, Inc., New York; 1988.
35. Taylor, C.F., *The Internal Combustion Engine in Theory and Practice*, Vol. 1., MIT Press, Cambridge, Mass; 1985 2nd ed.

36. Bracco, F.V., "Structure of Flames in Premixed-Charge IC Engines", *Combustion Science and Technology*, Vol. 58, pgs. 209-230, 1988.
37. Xu, H., "Some Critical Technical Issues on the Steady Flow Testing of Cylinder Heads", SAE paper 2001-01-1308, 2001.
38. Kang, K.Y. and Reitz, R.D., "The effect of intake valve alignment on swirl generation in a DI diesel engine", *Journal of Experimental Thermal and Fluid Science* Vol. 20, pgs 94-103, 1999.
39. Pope, Stephen B., *Turbulent Flows*, Cambridge University Press, Cambridge, UK; 2000.
40. Semenov, E.S., "Studies of Turbulent Gas Flow in Piston Engines", NASA Tech. Trans. F97, 1958.
41. Damkohler, G., "The Effect of Turbulence on the Flame Velocity in Gas Mixtures", NACA TM Report No. 1112, 1940.
42. Kent, J.C., et. al., "Effects of Intake Port Design and Valve Lift on In-Cylinder Flow and Burnrate", SAE paper 872153, 1987.
43. Mikulec, A., et. al., "The Effect of Swirl on Combustion in a Pancake Chamber Spark Ignition Engine: The Case of Constant Inducted Kinetic Energy", SAE paper 880200, 1988.
44. Kent, J.C., et. al., "Observation on the Effects of Intake-Generated Swirl and Tumble on Combustion Duration", SAE paper 892096, 1989.
45. Lancaster, D.R., et. al., "Effects of Turbulence on Spark-Ignition Engine Combustion", SAE paper 760160, 1976.
46. Massey, B.S., *Units, Dimensional Analysis and Physical Similarity*. Von Nostrad Reinhold Company, New York, New York; 1971.
47. Purday, H.F.P., *Diesel Engine Design*. Von Nostrad Reinhold Company, New York, New York; 1919.
48. Lichty, L., *Internal Combustion Engines*. McGraw-Hill Book Company, New York, New York; 1939.
49. Brandstetter, W.P., "Similarity Laws for Four-Stroke Engines and Numerical Results for the Intake Process Calculated with the Method of Characteristics", SAE paper 690466, 1969.
50. Chon, D.M., and Heywood, J.B., "Performance Scaling of Spark-Ignition Engines: Correlation and Historical Analysis of Production Engine Data", SAE paper 2000-01-0565, 2000.
51. Regueiro, J.F., and Korn, S.J., "Geometric Parameters of Four-Valve Cylinder Heads and Their Relationship to Combustion and Engine Full Load Performance", SAE paper 940205, 1994.
52. Eilts, P and Groth, I.K., "Similarity considerations on wall heat losses in internal combustion engines", *Proc. Instn. Mech. Engrs.*, Vol. 205, pg 139-142, 1991.

53. Boretti, A.A., and Cantore, G., “Similarity Rules and Parametric Design of Race Engines”, SAE paper 2000-01-0669, 2000.
54. Cantore, G., and Mattarelli, E., “Similarity Rules and Parametric Design of Four Stroke MotoGP Engines”, SAE paper 2004-01-3560, 2004.
55. Miyauchi, A., *et.al.*, “Development of High Performance Combustion Chamber for Four-Stroke Cycle Small Utility Engines”, SAE paper 1999-01-3336, 1999.
56. Lucas, G.G., and Brunt, M.F., “The Effect of Combustion Chamber Shape on the Rate of Combustion in a Spark Ignition Engine”, SAE paper 820165, 1982.
57. Mayo, J., “The Effect of Engine Design Parameters on Combustion Rate in Spark-ignited Engines”, SAE paper 750355, 1975.
58. Newlyn, H.A., and Few, P.C., “Effects of Changes in Engine Geometry on the Combustion in an S.I. Engine”, SAE paper 831035, 1983.
59. Davis, G.C, Tabaczynski, R.J., and Belaire, R.C., “The Effect of Intake Valve Lift on Turbulence Intensity and Burnrate in S.I. Engines-Model Versus Experiment”, SAE paper 840030, 1984.
60. Son, Jin-Wook, *et.al.*, “A Correlation Between Re-Defined Design Parameters and Flow Coefficients of SI Engine Intake Ports”, SAE paper 2004-01-0998, 2004.
61. Albert, B.P. and Ghandhi, J.B., “Residual Gas Measurements in a Utility Engine”, SAE paper 2004-32-0029, 2004.
62. Haugle, N.J. and Ghandhi, J.B., “The Effects of Exhaust Gas Recirculation in Utility Engines”, SAE paper 2006-32-0116, 2006.
63. Briggs Communication
64. SuperFlow Flowbench 600 Instructions, Superflow Corporation, 1976.
65. Johnson, R.A., *Probability and Statistics for Engineers*, 6th ed. Prentice Hall, Upper Saddle River, NJ., 2000.
66. Cengel, Y.A, and Cimbala, J.M., *Fluid Mechanics: Fundamentals and Applications*. McGraw Hill, Boston, MA; 2006.
67. Staples, L., Master’s Thesis, University of Wisconsin – Madison, 2008.
68. Shi, Yu, and Reitz, R., “Study of Diesel Engine Size-Scaling Relationships Based on Turbulence and Chemistry Scales”, SAE paper 2008-01-0955, 2008.

Appendix A.1

Pressure Transducer Calibration

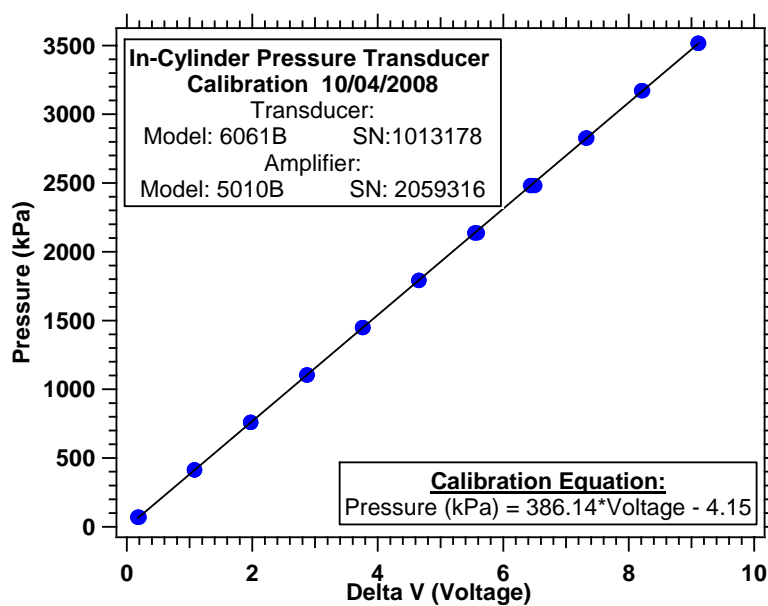


Figure A.1.1: Kistler In-cylinder Pressure Transducer Calibration

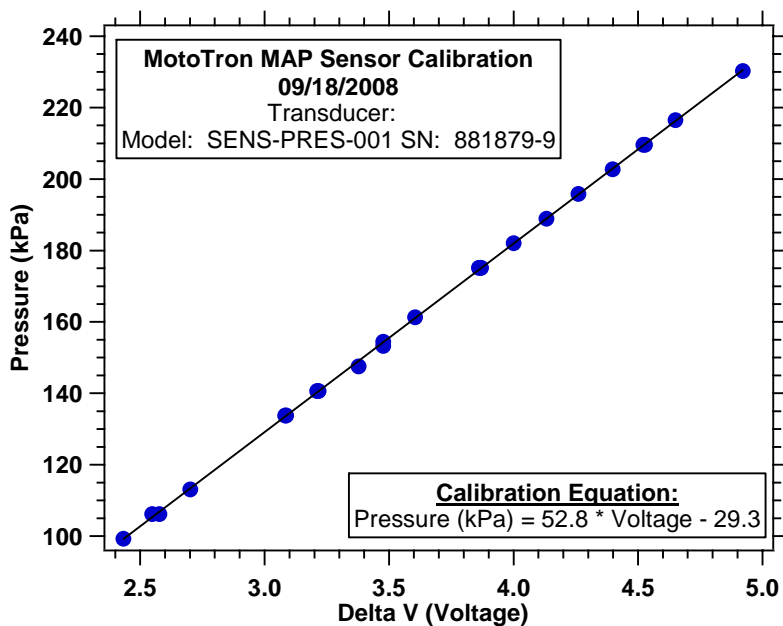


Figure A.1.2: MotoTron MAP Sensor Calibration

Appendix A.2

WOT Steady Flow Results

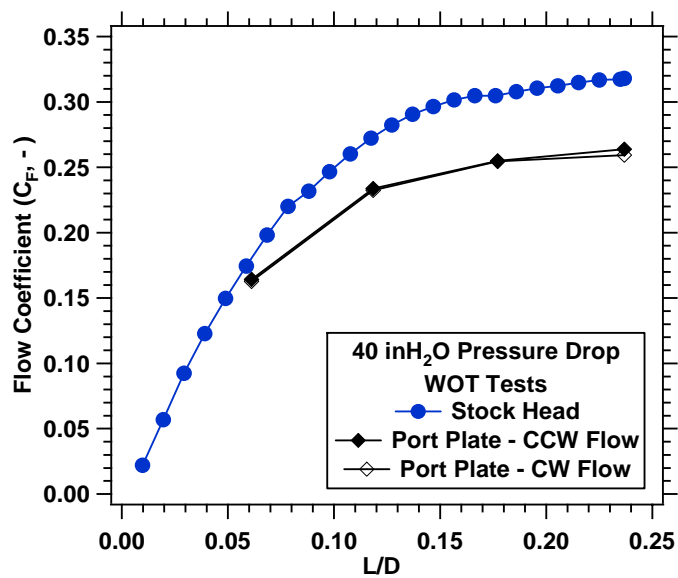


Figure A.2.1: WOT Flow Coefficient Response due to the Port Plates Favoring CCW and CW Flow Direction

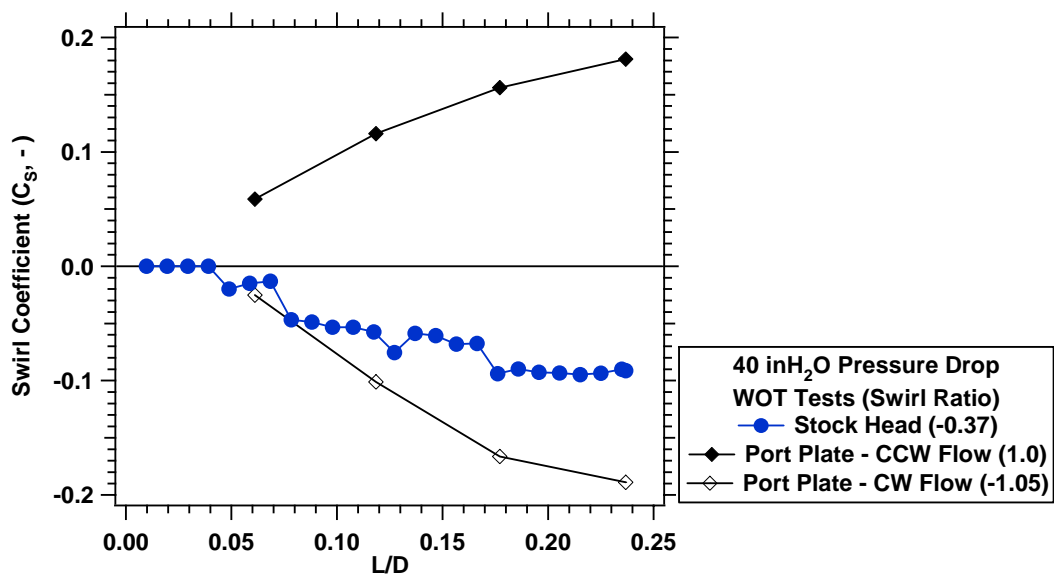


Figure A.2.2: WOT Swirl Coefficient Response Due to Port Plates Favoring CCW and CW Flow Direction

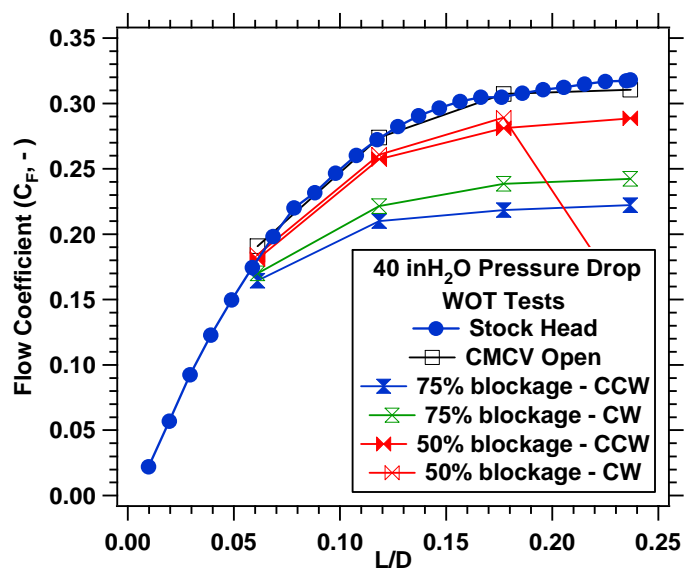


Figure A.2.3: WOT Flow Coefficient Response Due to Various CMCV Plate Blockages

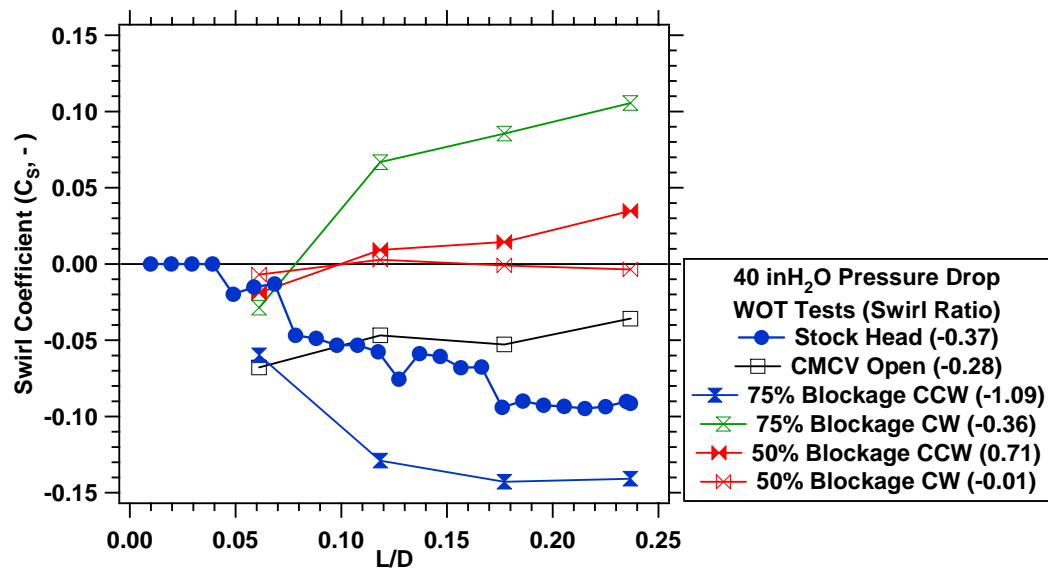


Figure A.2.4: WOT Swirl Coefficient Response Due to Various CMCV Plate Blockages

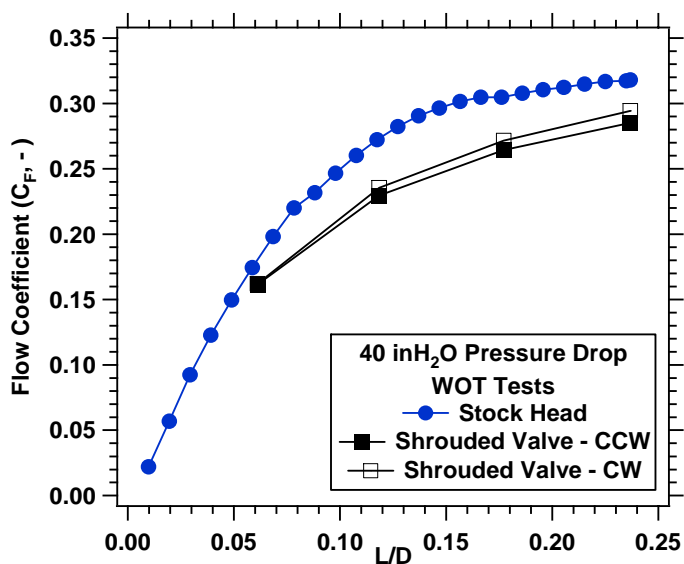


Figure A.2.5: WOT Flow Coefficient Response Due to the Shrouded Valve

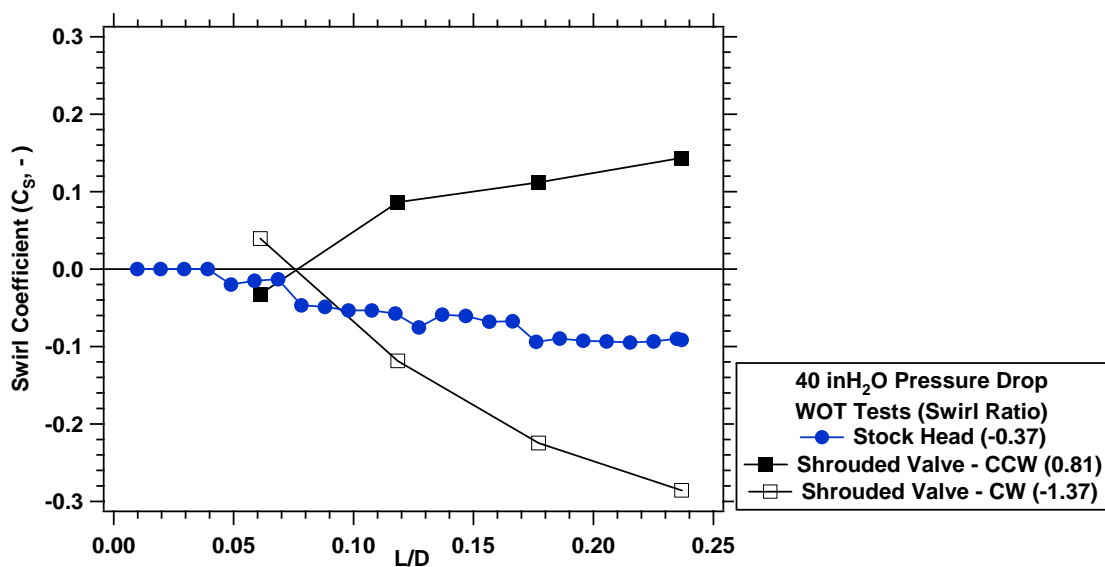


Figure A.2.6: WOT Swirl Coefficient Response Due to the Shrouded Valve

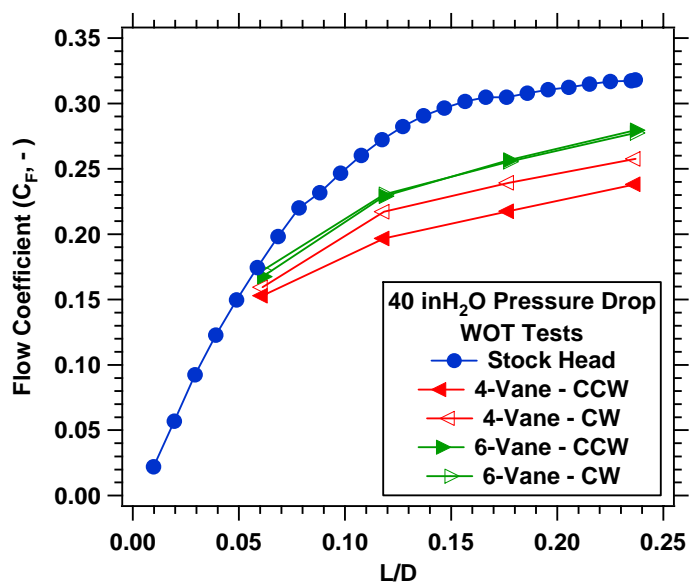


Figure A.2.7: WOT Flow Coefficient Response Due to the Pin-Wheel Blockages at the Valve Face

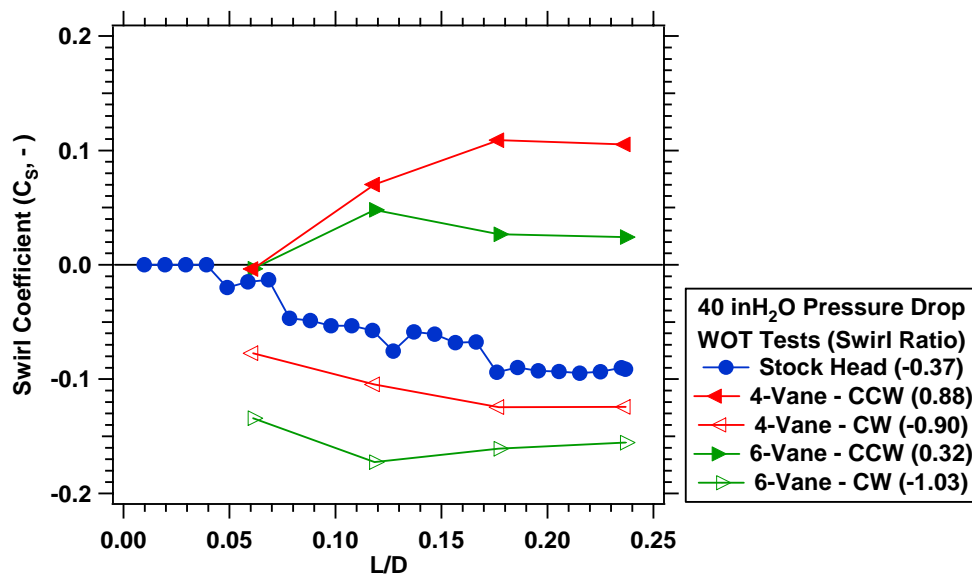


Figure A.2.8: WOT Swirl Coefficient Response Due to the Pin-Wheel Blockage at the Valve Face

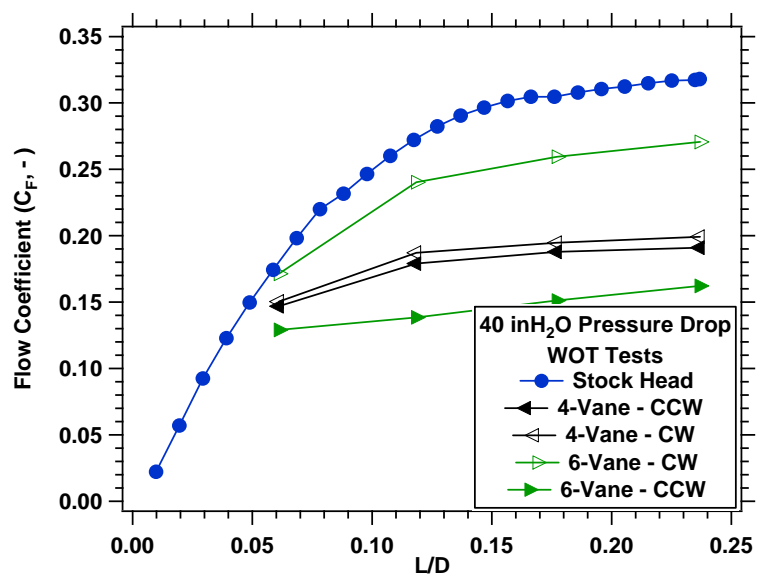


Figure A.2.9: WOT Flow Coefficient Response Due to the Pin-Wheel Blockages Attached to the Valve Stem

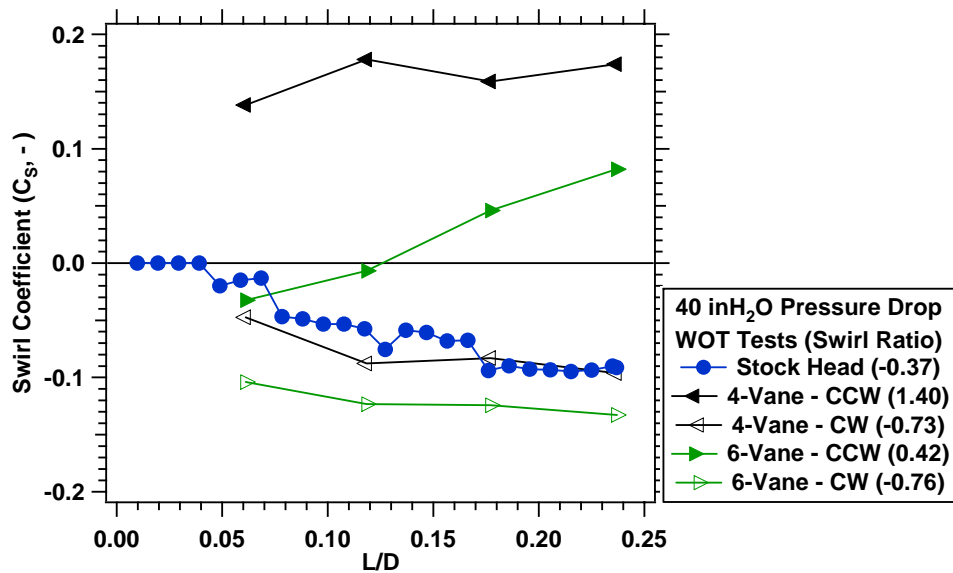


Figure A.2.10: WOT Swirl Coefficient Response Due to the Pin-Wheel Blockages Attached to the Valve Stem

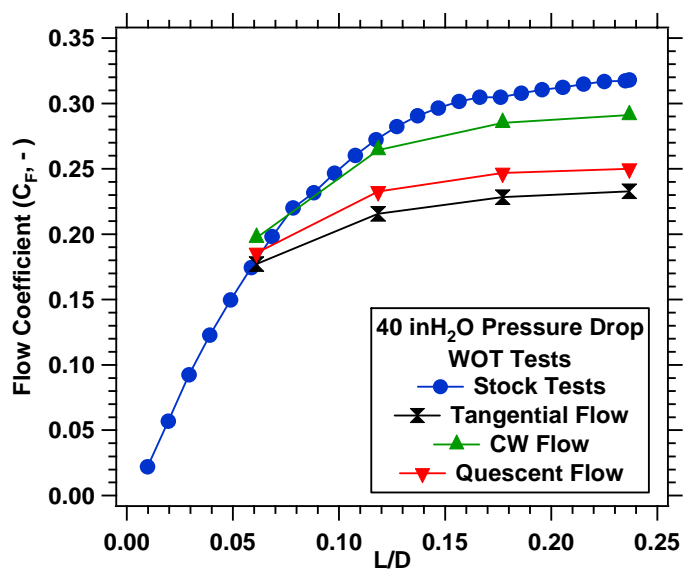


Figure A.2.11: WOT Flow Coefficient Response Due to the Port Blockages

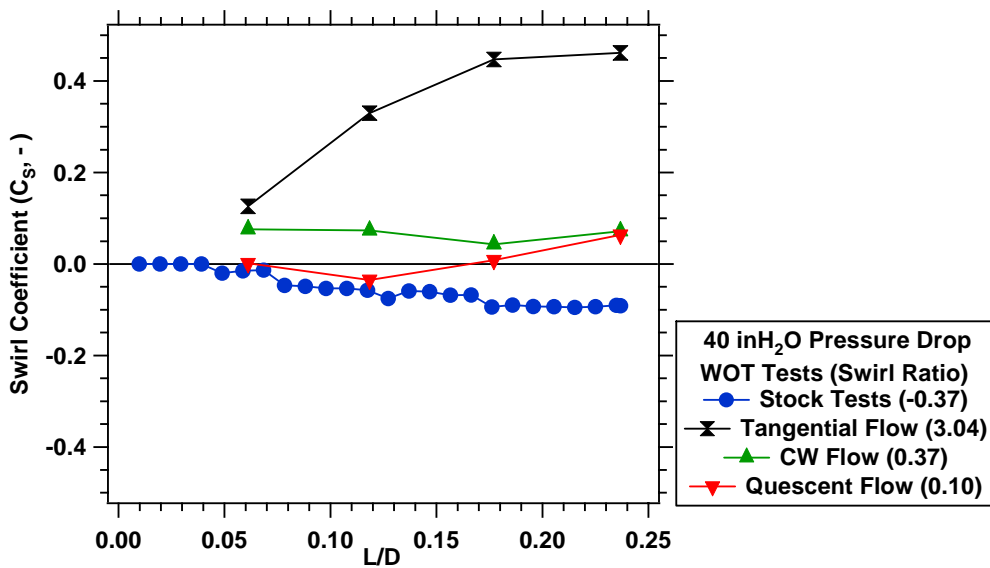


Figure A.2.12: WOT Swirl Coefficient Response Due to the Port Blockages

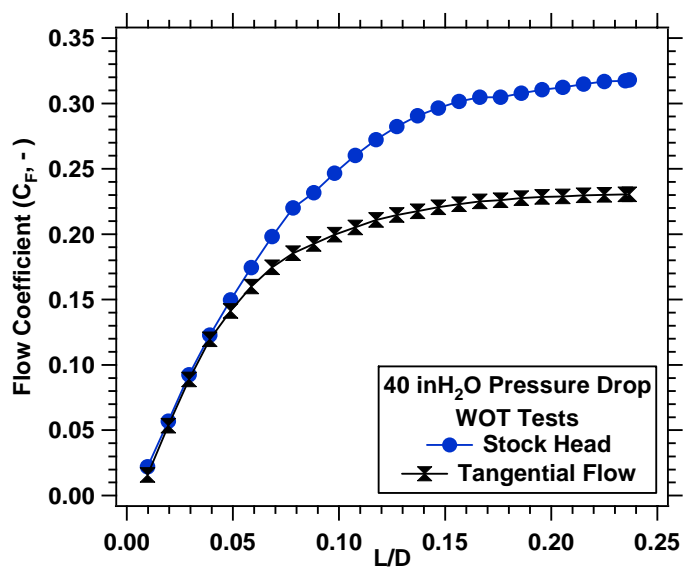


Figure A.2.13: WOT Flow Coefficient Response Due to the Port Blockage on the Modified Head Used for Combustion Tests

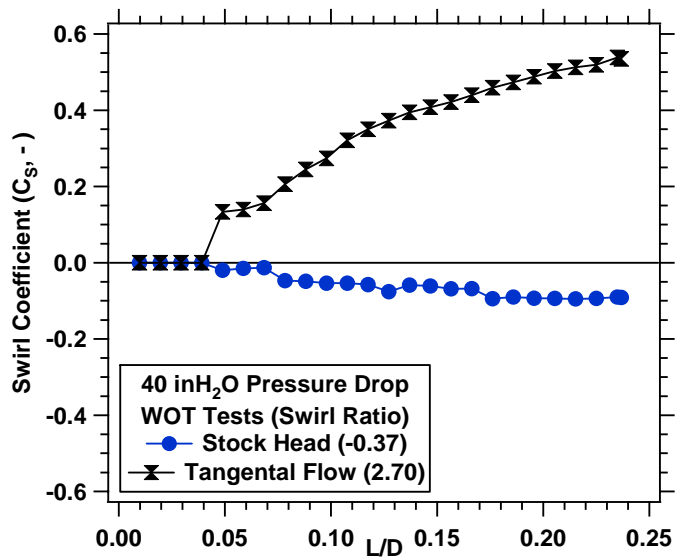


Figure A.2.14: WOT Swirl Coefficient Response Due to the Port Blockage on the Modified Head Used for Combustion Tests